UNIVERSITÀ DEGLI STUDI DI GENOVA

Facoltà di Scienze Matematiche, Fisiche e Naturali
Dipartimento di Fisica

Search for the Standard Model Higgs boson produced by vector boson fusion in the bottom quark pair decay channel and real-time flavour tagging selection with the ATLAS detector.

Carlo Varni

Thesis Advisors:

Fabrizio Parodi

External Referees:

Stephen Jacob Sekula

Paolo Francavilla

A Thesis presented
for the degree of Doctor of Philosophy
in the subject of
Physics.

Contents

Introduction

The engines used for High Energy Physics investigations are colliders: particle accelerators that rely on collisions between beams of particles for their searches. The Large Hadron Collider (*LHC*) [1, 2] reaches the world's highest center-of-mass energy and luminosity and collides bunches of protons and/or lead ions. The products of these collisions are analysed by the four main experiments located along the 27 km-long *LHC* accelerator ring. The *ATLAS* (acronym for **A** **T**oroidal **L**HC **A**pparatu**S**) experiment [3, 4] is the biggest of these. Toghether with the *CMS* (acronym for **C**ompact **M**uon **S**olenoids) experiment, *ATLAS* is one of the two general-purpose experiments at LHC – that nowadays involves over 3000 physicists from all around the world – built in order to probe proton-proton collisions. The physics programme it covers is broad, the main focus being on rare and low cross section processes. As such, the *ATLAS* experiment relies on a complex trigger system in order to reject events that cannot possibly contain interesting phenomena, thus enhancing the signal-to-background ratio of the selected data pool. Such a tool must be extremely efficient since it can select only few events to be recorded, in order to remain within the storage capability of the collaboration.

Amidst these phyics phenomena, the Higgs boson represents interesting a topic of investigation. In this field, the results obtained by the *ATLAS* collaboration are outstanding: the analysis of 2012-collected data led to the discovery of the Higgs boson and subsequent studies provided valuable information on the Higgs Boson's coupling to bosons and fermions. However, the observation of the Yukawa coupling with fermions is so far limited only to top and bottom quarks and to tau leptons. Concerning the other fermions, the required significance for claiming the evidence has not been reached yet, due to the rare nature of the phenomena and the overwelming background that can be found in a hadron collider.

This thesis work focuses on the study of the Higgs boson decay to bottom quarks, in particular in the *Vector Boson Fusion* (*VBF*) production mechanism, VBF $H \to b\bar{b}$: an extremely challenging search due to the overwelming multi-jet backgrounds and complex jet reconstruction, calibration and identification of b-jets typical of fully hadronic final states. The ability to correctly identify and discriminate particles and/or jets stemming from

differently flavoured quarks at online level provides an extremily power tool to reduce the QCD background. The b-jet triggers provide this capability. Without these triggers, such an analysis would not be feasible in a hadron collider.

During my *Ph.D.* I have worked at two iterations of the VBF $H \to b\bar{b}$ analysis [5, 6]. At first, the analysis of the data collected during the 2012 LHC operations showed that such a channel could indeed be studied, despite the huge amount of combinatorial background plaguing the event selection. Acting as the main analyser, I took care of: the data-selection, based on a multivariate analysis; the background modelling; the signal extraction; and the assessment of sources of systematic error. The analysis of the data collected during the 2016 LHC operations confirmed the previous results. Since the b-jet trigger is a crucial ingredient for this analysis I decided to focus my interest on more technical aspects, such as trigger studies and software developments for the handling of the data. This allowed me to focus on b-jet triggers, and starting from January 2018 I acted as coordinator of the b-jet triggers for the whole *ATLAS* collaboration.

This work is organized as follows :

- **Chapter 1** : A theoretical introduction in which I briefly introduce the Standard Model and the Higgs Boson framework.
- **Chapter 2** : A summary of the current status of our knowledge of the Yukawa coupling with fermions.
- **Chapter 3** : A quick overview of the ATLAS trigger system and a special focus on the b-jet triggers.
- **Chapter 4** : The introduction to the VBF $H \to b\bar{b}$ analsys, explaining the motivation of such an analysis.
- **Chapter 5** : A description of the analysis on data collected during 2012 operations.
- **Chapter 6** : A description of the analysis on data collected during 2016 operations.
- **Chapter 7** : A quick overview of the possible future enhancements, both for the b-jet triggers and the VBF $H \to b\bar{b}$ analysis.

CHAPTER 1

Theoretical background

This chapter illustrates the theoretical model that introduces the mechanism of spontaneous symmetry breaking that leads to the existence of the Higgs boson. This particle is part of the Standard Model: the most complete and satisfying field theory that describes particle interactions.

I will provide a quick description of this theoretical framework before focusing on the Brout–Englert–Higgs mechanism. I will explain how spontaneus symmetry breaking occurs and how it leads to massive particles; I will show both Higgs boson production and decay channels; and eventually, the reasons behind the choice of the search this thesis is focused on.

1.1 The Standard Model

In the last century, the main focus of physics research was to understand what the very fundamental constituents of matter are and what forces rule the interactions between these constituents. In the attempt of testing theoretical predictions, experiments resulted in revolutionary discoveries that led to the formulation of a comprehensive quantum field theory: the so-called Standard Model (SM) [7–9][1].

The SM describes and treats physical systems by means of fields – i.e. functions defined in each point of ordinary spacetime – in a renormalizable, local, gauge invariant (under the internal symmetries of the unitary product group $\mathbf{U}(1) \otimes \mathbf{SU}(2) \otimes \mathbf{SU}(3)$) and covariant way. Moreover, it associates particles to the irreducible rappresentations of the symmetry groups. According to this theory, only two kinds of particles exist in nature: fermions and bosons. The spin-statistic theorem guarantees the former obey Fermi-Dirac statistics and are half-integer spin particles, the

[1] Salam, Weinberg and Glashow's works were the first and main contributions that led to the Standard Model formulation. In 1979 these physicists were awarded jointly with the Nobel Prize in Physics *"for their contributions to the theory of the unified weak and electromagnetic interaction between elementary particles, including, inter alia, the prediction of the weak neutral current"* [10]. The first corroborations came from the discoveries of the Gargamelle, UA1 and UA2 collaborations [11–13].

latter obey Bose-Einstein statistics and have integer-spin values. Moreover, the CPT theorem [14] states every particle has an anti-particle with the same properties but opposite charges.

Particles interact by means of three forces – the electromagnetic, the weak and the strong interaction – due to the exchange of spin-1 particles: photon; $W^{\pm}$ and Z^0; and eight gluons. The SM unifies the electromagnetic and the weak forces into a single framework – the standard electro-weak theory – but treats the strong inteaction as a separate phenomenon.

Table 1.1 summarizes the main properties – electric charge and mass – of the spin-1/2 particles that constitute matter; table 1.2 illustrates how the six leptons and the six quarks are assembled into three families; table 1.3 gives an overview of the forces and their carriers.

Leptons		
Flavour	Charge $[e > 0]$	Mass [GeV]
e^-	-1	$(0.510998928 \pm 0.000000011) \times 10^{-3}$
ν_e	0	$< 2 \times 10^{-9}$
μ^-	-1	$(105.6583715 \pm 0.0000035) \times 10^{-3}$
ν_μ	0	$< 0.19 \times 10^{-3}$
τ^-	-1	1.77682 ± 0.00016
ν_τ	0	< 0.018

Quarks		
Flavour	Charge $[e > 0]$	Mass [GeV]
u	2/3	$2.3^{+0.7}_{-0.5} \times 10^{-3}$
d	-1/3	$4.8^{+0.5}_{-0.3} \times 10^{-3}$
c	2/3	1.275 ± 0.025
s	-1/3	$(95 \pm 5) \times 10^{-3}$
t	2/3	$173.21 \pm 0.51 \pm 0.71$
b	-1/3	4.18 ± 0.03

Table 1.1: *Scheme of spin-1/2 particles that constitute matter: the six leptons – electron, muon, tau and the corresponding neutrinos –; and the six quarks – up, down, charm, strange, top (or truth) and bottom (or beauty). Data taken from references [15–17].*

1.1.1 Electromagnetic interactions

Quantum Electro-Dynamics (QED) is the theoretical framework which fully describes how charged leptons (i.e. electrons, muons, taus and their anti-particles) interact with the electromagnetic field. It schematizes the interaction through the exchange of a virtual photon γ, giving a complete account of matter and light coupling.

	First family	Second family	Third family	
Leptons	$\begin{pmatrix}\nu_e\\e^-\end{pmatrix}$	$\begin{pmatrix}\nu_\mu\\\mu^-\end{pmatrix}$	$\begin{pmatrix}\nu_\tau\\\tau^-\end{pmatrix}$	Matter
Quarks	$\begin{pmatrix}u\\d\end{pmatrix}$	$\begin{pmatrix}c\\s\end{pmatrix}$	$\begin{pmatrix}t\\b\end{pmatrix}$	
Anti-Leptons	$\begin{pmatrix}\bar{\nu}_e\\e^+\end{pmatrix}$	$\begin{pmatrix}\bar{\nu}_\mu\\\mu^+\end{pmatrix}$	$\begin{pmatrix}\bar{\nu}_\tau\\\tau^+\end{pmatrix}$	Anti-matter
Anti-Quarks	$\begin{pmatrix}\bar{u}\\\bar{d}\end{pmatrix}$	$\begin{pmatrix}\bar{c}\\\bar{s}\end{pmatrix}$	$\begin{pmatrix}\bar{t}\\\bar{b}\end{pmatrix}$	

Table 1.2: *Overview of the very fundamental constituents of matter and anti-matter, divided into the three families. Anti-matter particles have the same properties as their matter counterparts, but opposite charges (electric, hypercharge).*

Interaction	Boson	Charge $[e > 0]$	Mass [GeV]
Electromagnetic	γ	0	0
Weak	Z^0	0	91.1876 ± 0.0021
	$W^\pm$	± 1	80.385 ± 0.015
Strong	8 gluons	0	0

Table 1.3: *Scheme of the three forces described by the Standard Model with the corresponding spin-1 gauge particles (the force carriers). Data taken from references [16, 17].*

If the $e - \mu - \tau$ universality is satisfied (i.e. the coupling of leptons to gauge bosons is flavour-independent), this theory is gauge invariant under the local set of transformation of the $\mathbf{U}(1)$ group

$$\begin{aligned} e^f &\rightarrow e^{-iq\Lambda(x)} e^f \\ A^\mu &\rightarrow A^\mu + \partial^\mu \Lambda \end{aligned} \tag{1.1}$$

where: Λ is a real function of the spacetime coordinates; q is the coupling constant of the theory, which corresponds to the charge of the lepton $e^f (= e, \mu, \tau$ for $f = 1, 2, 3$ respectively). The Lagrangian density that defines this system must be invariant with respect to the gauge transformation of equation 1.1. In order for this to be realized, the covariant derivative $D_\mu \equiv \partial_\mu + iqA_\mu$ must be introduced. This gives rise to the interaction term. Therefore, the Lagrangian is:

$$\mathcal{L}_{QED} = \sum_{f=1}^{3} \bar{e}^f (i\gamma^\mu D_\mu - m) e^f - \frac{1}{2}(\partial_\mu A_\nu)(\partial^\mu A^\nu) \tag{1.2}$$

QED forbids a photon mass term ($\propto A_\mu^2$) in the Lagrangian density due to the gauge conditions of equation 1.1. Thus, it predicts a massless photon, consistently with non-covariant formulation and experimental results. The Lagrangian density of equation 1.2 consists of a sum of terms each of which involves one kind of lepton only. As a consequence, the Feynman diagrams that describe QED interactions have vertices with fermion lines referring to the same family. Hence, QED precludes reactions involving different kinds of leptons, such as

$$e^- + \mu^+ \rightarrow e^+ + \mu^- \tag{1.3}$$

Ultimately, QED is a local theory: it describes only elementary (thus point-like) particles, such as leptons. In contrast, non-elementary particles, such as hadrons (protons and neutrons for instance), have a finite size. Being composed by color-charged elementary particles, Quantum ChromoDynamics (QCD) is needed to describe their kinematics properly.

1.1.2 Weak interactions

In 1954 the physicists Chen-Ning Franklin Yang and Robert Laurence Mills developed a gauge theory based on the invariance with respect to a non-Abelian group. The SM describes Weak interactions as invariant with respect to a set of transformations of the non-Abelian $\mathbf{SU}(2)$ group but treats them in analogy to QED.

Pioneering experiments [18] showed that weak interactions, unlike QED, violate parity symmetry. Thus, the SM treats differently the left and right components of Dirac spinors assigning the former to the doublet representation of $\mathbf{SU}(2)$ and the latter to the singlet (or scalar) one. It implies the presence of three independent currents (one neutral and two charged) and, as experiments conducted in 1983 evidenced [11, 12, 19, 20],, the existence

of three intermediate massive vector bosons – $W^{\pm}$ and Z^0 –, whose interactions are described by three vector fields W_i^μ (with $i = 1, 2, 3$). Acting only on the left components of leptons, the neutral current W_3^μ has a chiral nature and envisages the production of neutrinos, therefore it is dissimilar from the electromagnetic current.

In the so-called electro-weak unification, the SM includes the QED current into its framework by adding an Abelian factor and requiring the invariance with respect to a wider symmetry group. We should then introduce a new vector boson field, known as B_μ, that affects only the neutral current component, and impose invariance of the theory with respect to a set of transformations of the product group $\mathbf{U}(1) \otimes \mathbf{SU}(2)$:

$$\begin{gathered} l_L^f \equiv \begin{pmatrix} \nu^f \\ e^f \end{pmatrix}_L \rightarrow e^{ig\Lambda_i \frac{\tau_i}{2}} \begin{pmatrix} \nu^f \\ e^f \end{pmatrix}_L \\ e_R^f \rightarrow e_R^f \\ l_L^f, e_R^f \rightarrow e^{ig'\Lambda \frac{Y}{2}}\ l_L^f, e_R^f \\ W_i^\mu \rightarrow W_i^\mu - g\epsilon_{ijk}\Lambda_j W_k^\mu + \partial^\mu \Lambda_i \\ B^\mu \rightarrow B^\mu + \partial^\mu \Lambda \end{gathered} \tag{1.4}$$

where g' and g are the coupling constants for $\mathbf{U}(1)$ and $\mathbf{SU}(2)$ respectively, τ_i the generators of weak interactions, i.e. the Pauli matrices, and Y the weak hypercharge.

The electro-weak symmetry breaking mechanism gives mass to the current mediators, leaving the photon as a massless boson. However, this mechanism implies that the fields with a physical meaning and that acquire mass are a combination of W_i^μ and B^μ. Thus, we introduce the $W_\mu^\pm$, Z_μ and A_μ fields for the weak and the QED currents:

$$\begin{gathered} W_\mu^\pm = \tfrac{1}{\sqrt{2}} \left(W_\mu^1 \mp i\ W_\mu^2 \right) \\ Z_\mu = -\sin\theta_W B_\mu + \cos\theta_W W_\mu^3 \\ A_\mu = \cos\theta_W B_\mu + \sin\theta_W W_\mu^3 \end{gathered} \tag{1.5}$$

where θ_W is the weak angle, determined through experiments. We derive the weak gauge-invariant Lagrangian density, for fermion fields, that defines this theory as composed of three terms: a free propagation and two interaction

components.

$$\begin{aligned}
\mathcal{L}_0 &= \sum_{f=1}^{3} \left[i\ \bar{l}_L^f \gamma^\mu \partial_\mu l_L^f + i \bar{e}_R^f \gamma^\mu \partial_\mu e_R^f \right] \\
\mathcal{L}_c &= \tfrac{g}{\sqrt{2}} \sum_{f=1}^{3} \left[\bar{\nu}_L^f \gamma^\mu e_L^f W_\mu^+ + \bar{e}_L^f \gamma^\mu \nu_L^f W_\mu^- \right] \\
\mathcal{L}_n &= \bar{\Psi} \gamma^\mu \left[g\ \sin\theta_W\ T^3 + g' \tfrac{Y}{2} \cos\theta_W \right] \Psi A_\mu + \\
&+ \bar{\Psi} \gamma^\mu \left[g\ \cos\theta_W\ T^3 - g' \tfrac{Y}{2} \sin\theta_W \right] \Psi Z_\mu
\end{aligned} \tag{1.6}$$

where Ψ, introduced in the neutral term, is a column vector formed with all left-handed and right-handed fermions in the theory:

$$\Psi \equiv \begin{pmatrix} \nu_L^f \\ e_L^f \\ \nu_R^f \\ e_R^f \end{pmatrix} \tag{1.7}$$

However, the experiments themselves raised an issue: weak interactions have short range and thus intermediate vector bosons are massive while gauge theories require massless mediators. Moreover, charged leptons have non-negligible masses but the electro-weak Lagrangian density does not show a mass term for them, due to the gauge invariance. The Brout-Englert-Higgs mechanism solves this issue.

Electro-weak interactions for quarks

Quarks have an electric charge and are associated to non-trivial representations of the **SU**(2) group; thus, being coupled to both the photon and the weak bosons, they interact through the electro-weak force. Their confinement nature made them hard to be accepted when in 1964 the American physicists Murray Gell-Mann [21] and George Zweig [22] proposed, independently, a quark model able to describe the hadrons zoology of that time. This model proposed only three quarks: up, down and strange. But experimental discoveries evidenced the presence of new hadrons not explainable with this quark model: in 1970 the physicists S. Glashow, J. Iliopuoulos and L. Maiani suggested (GIM mechanism [23]) to include a new quark, i.e. the charm quark – whose existence was confirmed in 1974 thanks to the J/ψ discovery [24, 25]. In order to include the new findings, physicists formulated modified quark models such as the *Constituent Quark Model* (CQM) and the *Isgur and Karl model* [26–28]. The SM now implies the existence of at least six quark flavours, which have all been discovered.

Weak interactions allow a mixing phenomenon between quarks of different flavours: in 1973 Makoto Kobayashi and Toshihide Maskawa [30] introduced the CKM matrix V_{fg} – an extention of the GIM mechanism, which only included two families – adding one quark generation to the matrix previously defined by Nicola Cabibbo [31] . The absolute values of V_{fg}

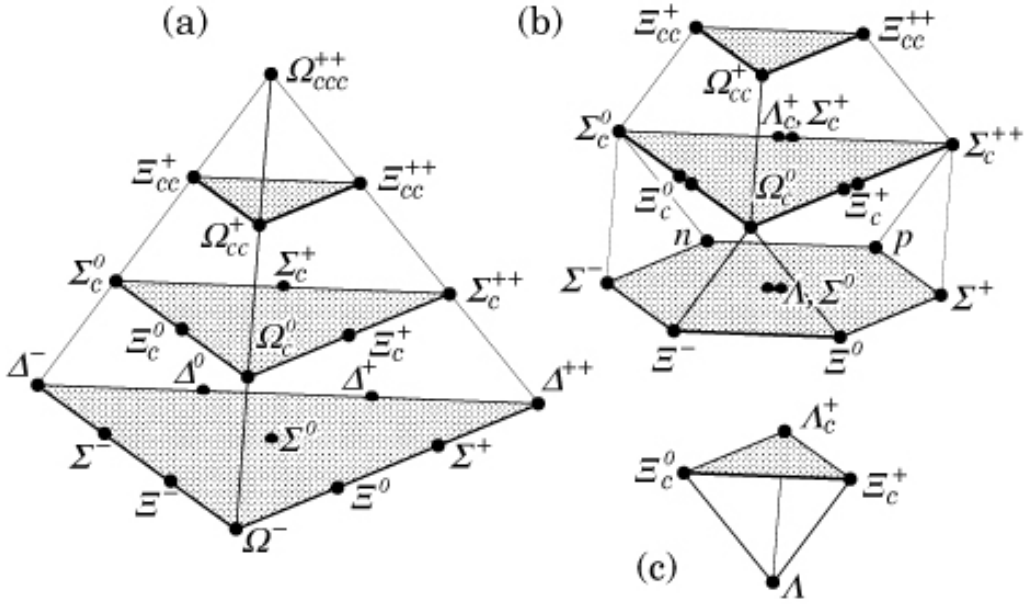

Figure 1.1: *Scheme of flavour symmetries of the* $\mathbf{SU}(4)$ *group:* $\mathbf{4} \otimes \mathbf{4} \otimes \mathbf{4} = \mathbf{20_S} \oplus \mathbf{20_{SM}} \oplus \mathbf{20_{AM}} \oplus \mathbf{4_A}$*: (a) the symmetric* $\mathbf{20_S}$ *of the* $\mathbf{SU}(4)$ *group, with the* $\mathbf{SU}(3)$ *decuplet on the lowest layer; (b) the mixed-symmetric* $\mathbf{20}$*s, with the* $\mathbf{SU}(3)$ *octet on the lowest layer; (c) the antisymmetric* $\mathbf{4_A}$*, with the* $\mathbf{SU}(3)$ *singlet at the bottom. Image taken from reference [29].*

are

$$V_{fg} \equiv \begin{pmatrix} |V_{ud}| & |V_{us}| & |V_{ub}| \\ |V_{cd}| & |V_{cs}| & |V_{cb}| \\ |V_{td}| & |V_{ts}| & |V_{tb}| \end{pmatrix} = \tag{1.8}$$

$$= \begin{pmatrix} 0.97425 \pm 0.00022 & 0.2252 \pm 0.0009 & (4.13 \pm 0.49) \times 10^{-3} \\ 0.225 \pm 0.008 & 0.986 \pm 0.016 & (41.1 \pm 1.3) \times 10^{-3} \\ (8.4 \pm 0.6) \times 10^{-3} & (40.0 \pm 2.7) \times 10^{-3} & 1.021 \pm 0.032 \end{pmatrix}$$

The SM includes the electro-weak interaction between quarks in analogy to how it treats leptons: it assign left and right components of quark Dirac spinors to the doublet and singlet representations of $\mathbf{SU}(2)$ and imposes invariance of the theory with respect to the set of transformation of both equation 1.4 and

$$q_L^f \equiv \begin{pmatrix} u^f \\ d^f \end{pmatrix}_L \rightarrow e^{ig\Lambda_i \frac{\tau_i}{2}} \begin{pmatrix} u^f \\ d^f \end{pmatrix}_L$$

$$u_R^f, d_R^f \rightarrow u_R^f, d_R^f \tag{1.9}$$

$$q_L^f, u_R^f, d_R^f \rightarrow e^{ig'\Lambda \frac{Y}{2}}\ q_L^f, u_R^f, d_R^f$$

where g, g', τ_i, Y, Λ and Λ_i are the same quantities as in equation 1.4 and f labels the quark family ($u^f = u, c, t$ and $d^f = d, s, b$ for $f = 1, 2, 3$). The Lagrangian density that defines this environment is an extension of the

Lagrangian density of equation 1.6

$$\begin{aligned}
\mathcal{L}_0 &= \textstyle\sum_{f=1}^{3} \Big[i\ \bar{l}_L^f \gamma^\mu \partial_\mu l_L^f + i \bar{e}_R^f \gamma^\mu \partial_\mu e_R^f + \\
&+ i\ \bar{q}_L^f \gamma^\mu \partial_\mu q_L^f + i \bar{u}_R^f \gamma^\mu \partial_\mu u_R^f + i \bar{d}_R^f \gamma^\mu \partial_\mu d_R^f \Big] \\
\mathcal{L}_c &= \tfrac{g}{\sqrt{2}} \left[\textstyle\sum_{f=1}^{3} \bar{\nu}_L^f \gamma^\mu e_L^f + \sum_{f,g=1}^{3} \bar{u}_L^f \gamma^\mu V_{fg} d_L^g \right] W_\mu^+ + \\
&+ \tfrac{g}{\sqrt{2}} \left[\textstyle\sum_{f=1}^{3} \bar{e}_L^f \gamma^\mu \nu_L^f + \sum_{f,g=1}^{3} \bar{d}_L^f \gamma^\mu V_{fg}^* u_L^g \right] W_\mu^- \\
\mathcal{L}_n &= \bar{\Psi} \gamma^\mu \left[g\ \sin\theta_W\ T^3 + g' \tfrac{Y}{2} \cos\theta_W \right] \Psi A_\mu + \\
&+ \bar{\Psi} \gamma^\mu \left[g\ \cos\theta_W\ T^3 - g' \tfrac{Y}{2} \sin\theta_W \right] \Psi Z_\mu
\end{aligned} \tag{1.10}$$

where Ψ now includes the left components of quarks too.

1.1.3 Strong interactions

The strong force affects particles with a color charge: the quarks and the eight color-charged gluons, the force carriers. The gauge theory that describes quark dynamics is Quantum ChromoDynamics (QCD). Based on the Yang-Mills theory, it treats strong forces as invariant with respect to a set of transformation of the **SU**(3) group.

We introduce eight gauge fields A_i^μ and define six Dirac fields Ψ^f (with $f = u, d, s, c, b, t$) as composed of three component fields, one for each color (r, g, b). Instead of the three Pauli matrices in the **SU**(2) case, it is the eight Gell-Mann matrices λ that act as generators of **SU**(3). Thus, the theory is invariant with respect to the local transformation

$$\begin{aligned}
\Psi^f &\to e^{i\ g_s \Lambda_i \frac{\lambda_i}{2}} \Psi^f \\
A_i^\mu &\to A_i^\mu - g_s f_{ijk} \Lambda_j A_k^\mu + \partial^\mu \Lambda_i
\end{aligned} \tag{1.11}$$

where: g_s is the strong coupling constant; f_{ijk} are the total antisymmetric structure constants; and Λ_i are real local functions of the spacetime coordinate, small enough to ensure the validity of perturbation theory. Table 1.4 reports the f_{ijk} values for different ijk configurations.

ijk	123	147	156	246	257	345	367	458	678
f_{ijk}	1	$\frac{1}{2}$	$-\frac{1}{2}$	$\frac{1}{2}$	$\frac{1}{2}$	$\frac{1}{2}$	$-\frac{1}{2}$	$\frac{\sqrt{3}}{2}$	$\frac{\sqrt{3}}{2}$

Table 1.4: *Values of the completely antisymmetric structure constant f_{ijk} for different ijk combinations. Data taken from reference [32].*

We include the interaction gluon-quark term in the covariant derivative D_μ[2], and introduce the gauge fields $G_i^{\mu\nu} \equiv \partial^\nu A_i^\mu - \partial^\mu A_i^\nu + g_s f_{ijk} A_j^\mu A_k^\nu$. The

[2]In strong interactions the covariant derivative is defined as $D_\mu \equiv \partial_\mu + i g_s \frac{\lambda^i}{2} A_\mu^i$

Lagrangian density that defines this theory is

$$\mathcal{L}_{QCD} = \sum_{f=1}^{3} \bar{\Psi}^f \left(i\gamma^\mu D_\mu - m_f \right) \Psi^f - \frac{1}{4} G_{i\mu\nu} G_i^{\mu\nu} \tag{1.12}$$

1.2 Spontaneous symmetry breaking

Experiments [11, 12, 19, 20] demonstrated the electro-weak bosons $W^\pm$ and Z^0, as well as charged leptons, are massive particles. However, gauge theories require massless mediators and fermions. Due to the chiral nature of the weak interactions, Dirac mass terms lack gauge invariance: these are proportional to

$$\bar{e}^f e^f = \bar{e}^f_L e^f_R + \bar{e}^f_R e^f_L \tag{1.13}$$

but left- and right-handed components transform in different ways under an $\mathbf{SU}(2)$ transformation. This implies the existence of another mechanism through which particles acquire mass.

This issue puzzled physicists for many years, until 1961-1962 when the theoretical physicist Jeffrey Goldstone proposed a new model in which particles acquire mass through a mechanism of spontaneous symmetry breaking [33, 34]. This concept, first suggested by Yoichiro Nambu during his studies about superconductivity and ferromagnetism [35], states spontaneous symmetry breaking occurs when a system – with a definite symmetry invariance – has a degenerate ground state; the arbitrary choice of the fundamental configuration produces the asymmetry.

1.2.1 The Brout-Englert-Higgs mechanism

Goldstone took Nambu's concept and developed a field theory – invariant under a $\mathbf{SU}(2)$ gauge transformation – that exhibits this behaviour. Robert Brout, François Englert and Peter Higgs generalized this theory to be invariant under a $\mathbf{U}(1)$ gauge transformation [36–38]. The modern standard electroweak theory is invariant under a $\mathbf{U}(1)\otimes\mathbf{SU}(2)$ gauge transformation.

The Brout-Englert-Higgs mechanism presents a scalar field whose potential has its minimum translated from the origin of the isotopic space (reported on figure 1.2). As a consequence, the ground state – characterized by the non-vanishing vacuum expectation value – doesn't show all the symmetries the Lagrangian has. Assigning the scalar field ϕ to the doublet representation of the non-Abelian $\mathbf{SU}(2)$ group, the minimum of the potential lies in $\phi_0 = v/\sqrt{2}$ – where v is a constant. This theory imposes the invariance with respect to the set of transformations of the gauge $\mathbf{U}(1)\otimes\mathbf{SU}(2)$ product group

$$\begin{aligned} \phi + \phi_0 &\to e^{ig\Lambda_i \frac{\tau^i}{2}} \left(\phi + \phi_0 \right) \\ \phi + \phi_0 &\to e^{ig'\Lambda \frac{Y}{2}} \left(\phi + \phi_0 \right) \end{aligned} \tag{1.14}$$

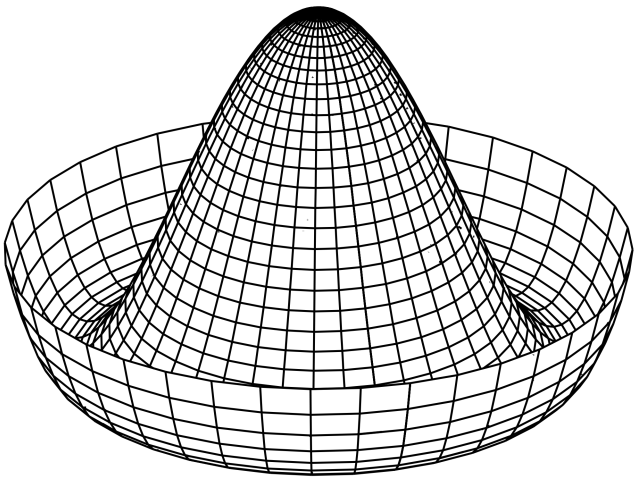

Figure 1.2: *The Higgs potential:* $\mathcal{V} = \mu^2|\phi|^2 + \lambda|\phi|^4$. *With* $\mu^2 < 0$ *and* $\lambda > 0$ *the spontaneus symmetry breaking occurs. The minimum of the potential* $\mathcal{V}$ *lies in a circle* $\phi_0 = e^{i\alpha\theta}v/\sqrt{2}$ *(where* v *is an* $\mathbf{SU}(2)$ *doublet constant with* $|v| = \sqrt{-\mu^2/\lambda}$*): the vacuum state is chosen so that* $\phi_0 = v/\sqrt{2}$*, thus breaking the symmetry.*

The SM expects the symmetry breaking to occur in three of the four dimensions on the $\mathbf{U}(1)\otimes\mathbf{SU}(2)$ gauge group without affecting the electrodynamics sub-group $\mathbf{U}_{em}(1)$. The absence of a massive photon is assured by the condition

$$\phi_0 \to e^{ie\alpha Q}\phi_0 \tag{1.15}$$

where the charge $Q = T_3 + Y/2$. This system has two non-trivial solutions: the first one requires $Y = +1$, the second one requires $Y = -1$. As custom, we choose the first solution.

Being assigned to the doublet representation of the $\mathbf{SU}(2)$ group, the ϕ field is composed by two complex fields: ϕ^0 and ϕ^+. Several parametrizations exist. These see each complex scalar field as composed by two real scalar fields – thus introducing the Higgs and the Goldstone bosons. The latter represents unphysical degrees of freedom and give mass to the $W^\pm$ and Z^0 fields.

$$\phi + \phi_0 = \frac{1}{\sqrt{2}} e^{i\tau^i \frac{\theta^i}{v}} \begin{pmatrix} 0 \\ v + H \end{pmatrix} \tag{1.16}$$

The phase factor in equation 1.16 contains these non-physical degrees of freedom and H is the Higgs boson. The former disappears using a suitable $\mathbf{SU}(2)$ gauge transformation, the so-called *unitary gauge*. The advantage of this choice is the Goldstone bosons disappear, while both the Higgs and the gauge bosons acquire mass. In this gauge, the Higgs Lagrangian density appears as

$$\mathcal{L}_H = \frac{1}{2}\partial^\mu H \partial_\mu H + \left[\frac{1}{4}g^2 W^{\mu+}W^-_\mu + \frac{1}{8}(g^2+g'^2)Z^\mu Z_\mu\right](H+v)^2 + \\ + \frac{1}{2}(2\lambda v^2)H^2 + \lambda v H^3 + \frac{1}{4}\lambda H^4 \quad (1.17)$$

The quadratic parts in the fields produce the mass terms for both the Higgs boson and the intermediate vector bosons. These are functions of the coupling constant, g and g', λ and v:

$$m_H^2 = 2\lambda v^2 \\ m_W^2 = \tfrac{1}{4}g^2 v^2 \qquad m_Z^2 = \tfrac{1}{4}\left(g^2+g'^2\right)v^2 \quad (1.18)$$

1.2.2 Quark and lepton masses

The gauge symmetries of the SM forbid mass terms for fermions: the chiral nature of spinors makes Dirac mass terms of equation 1.13 not invariant under an $\mathbf{SU}(2)$ transformation. However, both quarks and leptons acquire mass via the Brout-Englert-Higgs mechanism, through a Yukawa coupling: the interaction between two fermions and a boson – the leptons/quarks and the Higgs boson. The resulting Lagrangian densities add mass terms in the SM.

One should introduce three generic 3×3 complex matrices, y_u^f, y_d^f and y_e^f. They represent the Yukawa coupling strengths. However, the Yukawa mass terms – in the form of $\bar{l}_L^f(\phi+\phi_0)y_e^f e_R^f + h.c.$ – are not diagonal in the fields, but a bi-unitary trasformation can diagonalize them. Thus, introducing the six unitary matrices $V_{R,L}^{U,D,E}$, we obtain three diagonal matrices h_u^f, h_d^f and h_e^f – with real and non-negative entries – defined as

$$h_e^f \equiv V_L^{E\dagger} y_e^f V_R^E \\ h_u^f \equiv V_L^{U\dagger} y_u^f V_R^U \quad (1.19) \\ h_d^f \equiv V_L^{D\dagger} y_d^f V_R^D$$

This diagonalization process induces a new definition of the fields. Thus, we rotate them in such a way they bring the Yukawa interaction term in diagonal form:

$$\tilde{e}_{L,R}^f \equiv V_{L,R}^E \; e_{L,R}^f \\ \tilde{u}_{L,R}^f \equiv V_{L,R}^U \; u_{L,R}^f \quad (1.20) \\ \tilde{d}_{L,R}^f \equiv V_{L,R}^D \; d_{L,R}^f$$

This leads to Lagrangian terms in which we can identify the corresponding quark and lepton mass terms. In the *unitary gauge* these are

$$\begin{aligned} \mathcal{L}_Y^{lept} &= -\tfrac{1}{\sqrt{2}}(v+H)\sum_{f=1}^{3} h_e^f \bar{e}^f e^f \\ \mathcal{L}_Y^{quark} &= -\tfrac{1}{\sqrt{2}}(v+H)\sum_{f=1}^{3}\left(h_u^f \bar{u}^f u^f + h_d^f \bar{d}^f d^f\right) \end{aligned} \tag{1.21}$$

These rotations influence the other SM Lagrangian terms, leaving unchanged those diagonal in the fields. The neutral-current interaction Lagrangian remain unchanged, due to the universality of the fermion couplings to the photon and to the Z^0 boson. However, the quark Lagrangian in equation 1.21 affect the charged-current interaction Lagrangian while the leptonic Lagrangian leaves it unchanged.

This different behaviour is due to the absence of right-handed neutrinos. Being massless, they can undergo the same rotations as the charged leptons leaving the $\mathcal{L}_c$ Lagrangian untouched. As a consequence, in the SM with massless neutrinos, leptons have no mixing among different generations and the mass eigenstates coincide with the interaction eigenstates. On the other hand, the up and down components of the same left-handed doublet transforms in different ways – V_L^U and V_L^D are different matrices – and this causes a change in the $\mathcal{L}_c$ Lagrangian. Moreover, we can express the unitary matrix $V_L^{U\dagger} V_L^D$ as a single one: the Cabibbo-Kobayashi-Maskawa matrix V_{CKM} (equation 1.8).

The corresponding quark and lepton masses are functions of the Yukawa coupling matrices and v. Table 1.1 reports the experimental mass values.

$$\begin{aligned} m_e^f &= \tfrac{1}{\sqrt{2}} v h_e^f \\ m_u^f = \tfrac{1}{\sqrt{2}} v h_u^f \qquad & m_d^f = \tfrac{1}{\sqrt{2}} v h_d^f \end{aligned} \tag{1.22}$$

1.3 The standard electroweak Lagrangian

We can now summarize the standard electro-weak Lagrangian density and schematize it as composed by seven terms – each Lorentz invariant and possessing a $\mathbf{U}(1)\otimes\mathbf{SU}(2)$ group gauge symmetry. These Lagrangian terms are namely:

- Free Lagrangian for matter fermions

$$\begin{aligned} \mathcal{L}_0^F = \sum_{f=1}^{3} \big[& \bar{\nu}^f i\gamma^\mu \partial_\mu \nu^f + \bar{e}^f (i\gamma^\mu \partial_\mu - m_e^f) e^f + \\ & + \bar{u}^f (i\gamma^\mu \partial_\mu - m_u^f) u^f + \bar{d}^f (i\gamma^\mu \partial_\mu - m_d^f) d^f \big] \end{aligned} \tag{1.23}$$

- Free Lagrangian for gauge and Higgs bosons

$$\mathcal{L}_0^G = -\frac{1}{4}Z_{\mu\nu}Z^{\mu\nu} + \frac{1}{2}m_Z^2 Z^\mu Z_\mu - \frac{1}{2}W_{\mu\nu}^+ W_-^{\mu\nu} + m_W^2 W^{\mu+}W_\mu^- + \\ - \frac{1}{2}\partial_\mu A_\nu \partial^\mu A^\nu + \frac{1}{2}\partial^\mu H \partial_\mu H - \frac{1}{2}m_H^2 H^2 \quad (1.24)$$

- Electromagnetic coupling

$$\mathcal{L}_{em} = e\sum_{f=1}^{3}\left(-\bar{e}^f\gamma^\mu e^f + \frac{2}{3}\bar{u}^f\gamma^\mu u^f - \frac{1}{3}\bar{d}^f\gamma^\mu d^f\right)A_\mu \quad (1.25)$$

- Charged-current interaction

$$\mathcal{L}_c = \frac{g}{2\sqrt{2}}\left[\sum_{f=1}^{3}\bar{\nu}^f\gamma^\mu\left(1-\gamma_5\right)e^f + \sum_{f,g=1}^{3}\bar{u}^f\gamma^\mu\left(1-\gamma_5\right)V_{fg}d^g\right]W_\mu^+ + \\ + \frac{g}{2\sqrt{2}}\left[\sum_{f=1}^{3}\bar{e}^f\gamma^\mu\left(1-\gamma_5\right)\nu^f + \sum_{f,g=1}^{3}\bar{d}^g\gamma^\mu\left(1-\gamma_5\right)V_{fg}^* u^f\right]W_\mu^- \quad (1.26)$$

- Neutral-current interaction

$$\mathcal{L}_n = \frac{e}{4\cos\theta_W\sin\theta_W}\sum_{f=1}^{3}\Big[\bar{\nu}^f\gamma^\mu(1-\gamma_5)\nu^f \; + \\ + \bar{e}^f\gamma^\mu(-1+4\sin^2\theta_W+\gamma_5)e^f + \bar{u}^f\gamma^\mu(1-\frac{8}{3}\sin^2\theta_W-\gamma_5)u^f + \\ + \bar{d}^f\gamma^\mu(-1+\frac{4}{3}\sin^2\theta_W+\gamma_5)d^f\Big]Z_\mu \quad (1.27)$$

- Vector-boson self-interaction

$$\mathcal{L}_V = ig\sin\theta_W(W_{\mu\nu}^+W_-^\mu A^\nu - W_{\mu\nu}^-W_+^\mu A^\nu + F_{\mu\nu}W_+^\mu W_\nu^-) + \\ + ig\cos\theta_W(W_{\mu\nu}^+W_-^\mu Z^\nu - W_{\mu\nu}^-W_+^\mu Z^\nu + Z_{\mu\nu}W_+^\mu W_\nu^-) + \\ + \frac{g}{2}(2g^{\mu\nu}g^{\rho\sigma} - g^{\mu\rho}g^{\nu\sigma} - g^{\mu\sigma}g^{\nu\rho})\Big[\frac{1}{2}W_\mu^+W_\nu^+W_\rho^-W_\sigma^- + \\ - W_\mu^+W_\nu^+(A_\rho A_\sigma\sin^2\theta_W + Z_\rho Z_\sigma\cos^2\theta_W + 2A_\rho Z_\sigma\sin\theta_W\cos\theta_W)\Big] \quad (1.28)$$

- Higgs interaction

$$\mathcal{L}_H = \left(m_W^2W^{\mu+}W_\mu^- + \frac{1}{2}m_Z^2Z^\mu Z_\mu\right)\left(\frac{H^2}{v^2}+\frac{2H}{v}\right) + \\ - \frac{H}{v}\sum_{f=1}^{3}\left(m_d^f\bar{d}^f d^f + m_u^f\bar{u}^f u^f + m_e^f\bar{e}^f e^f\right) - \lambda v H^3 - \frac{1}{4}\lambda H^4 \quad (1.29)$$

1.4 The production and decay modes of the Higgs Boson

Despite the fact that some of the properties of the Higgs boson are still under investigation and/or in a phase of precise measurement, the theoretical framework allows a precise calculation of the expected Higgs production cross sections, decay rates, branching ratios and couplings. Figures 1.3 and 1.5 show the Higgs cross section and branching ratio, as functions of the Higgs mass at this energy. Figures 1.4 and 1.6 summarize the corresponding Feynman diagrams.

There are different mechanisms with which the Higgs boson can be produced at a hadron collider like LHC. In decreasing order of cross section magnitude these are : Gluon-gluon Fusion (ggF); Vector Boson Fusion (VBF); associated production with an intermediate vector boson (or "Higgs strahlung"); and associated production with a top pair ($t\bar{t}H$). The cross section of these processes at different center-of-mass energies is reported in table 1.5. There is as well a huge plethora of decay modes, whose Branching Ratios (BR) highly depend on the mass of the Higgs Boson. Since this mass value has been found to be 125.18 ± 0.16 GeV [39] , the main decay mode is into a pair of bottom quarks (BR of 5.84×10^{-1}). The other decay modes include: $H \to ZZ$ (BR of 2.62×10^{-2}); $H \to W^+W^-$ (BR of 2.14×10^{-1}); $H \to \tau^+\tau^-$ (BR of 6.27×10^{-2}); $H \to \gamma\gamma$ (BR of 2.27×10^{-3}); $H \to Z\gamma$ (BR of 1.53×10^{-3}); and $H \to \mu^+\mu^-$ (BR of 2.18×10^{-4}).

$\sqrt{s}[TeV]$	Production cross section for $m_H = 125$ GeV [pb]					
	ggF	VBF	WH	ZH	$t\bar{t}H$	total
7	$15.3^{+10\%}_{-10\%}$	$1.24^{+2\%}_{-2\%}$	$0.58^{+3\%}_{-3\%}$	$0.34^{+4\%}_{-4\%}$	$0.09^{+8\%}_{-14\%}$	17.5
8	$19.5^{+10\%}_{-11\%}$	$1.60^{+2\%}_{-2\%}$	$0.70^{+3\%}_{-3\%}$	$0.42^{+5\%}_{-5\%}$	$0.13^{+8\%}_{-13\%}$	22.3
13	$44.1^{+11\%}_{-11\%}$	$3.78^{+2\%}_{-2\%}$	$1.37^{+2\%}_{-2\%}$	$0.88^{+5\%}_{-5\%}$	$0.51^{+9\%}_{-13\%}$	50.6
14	$49.7^{+11\%}_{-11\%}$	$4.28^{+2\%}_{-2\%}$	$1.51^{+2\%}_{-2\%}$	$0.99^{+5\%}_{-5\%}$	$0.61^{+9\%}_{-13\%}$	57.1

Table 1.5: *Cross sections for different Higgs mass values and at a center of mass energy of $\sqrt{s}$ = 7, 8, 13 and 14 TeV. Data taken from references [40] assuming $m_H = 125$ GeV.*

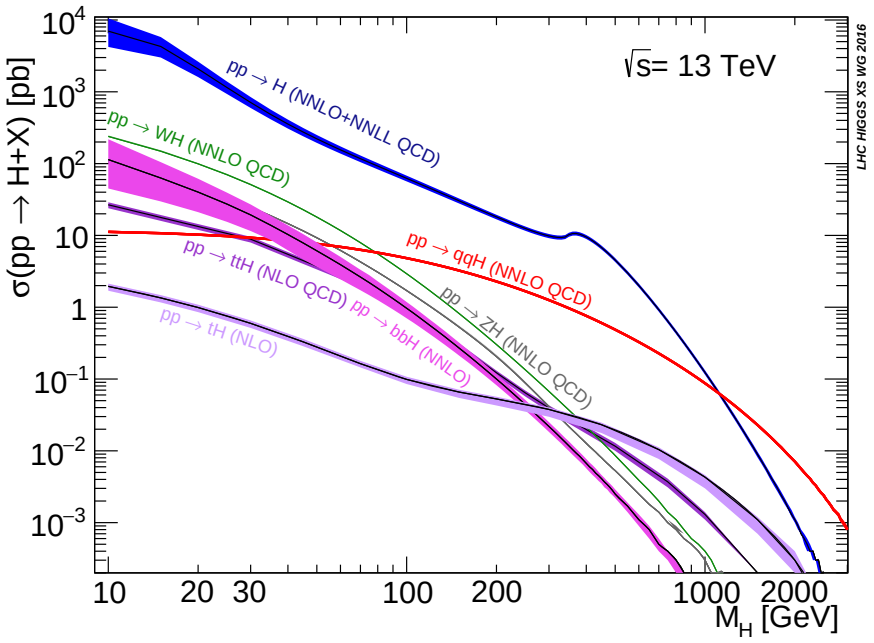

Figure 1.3: *The Standard Model Higgs boson production cross sections at $\sqrt{s} = 13$ TeV for differnet Higgs mass values. Figure supplied by the Higgs Cross Section Working Group* `https://twiki.cern.ch/twiki/bin/view/LHCPhysics/LHCHXSWG`.

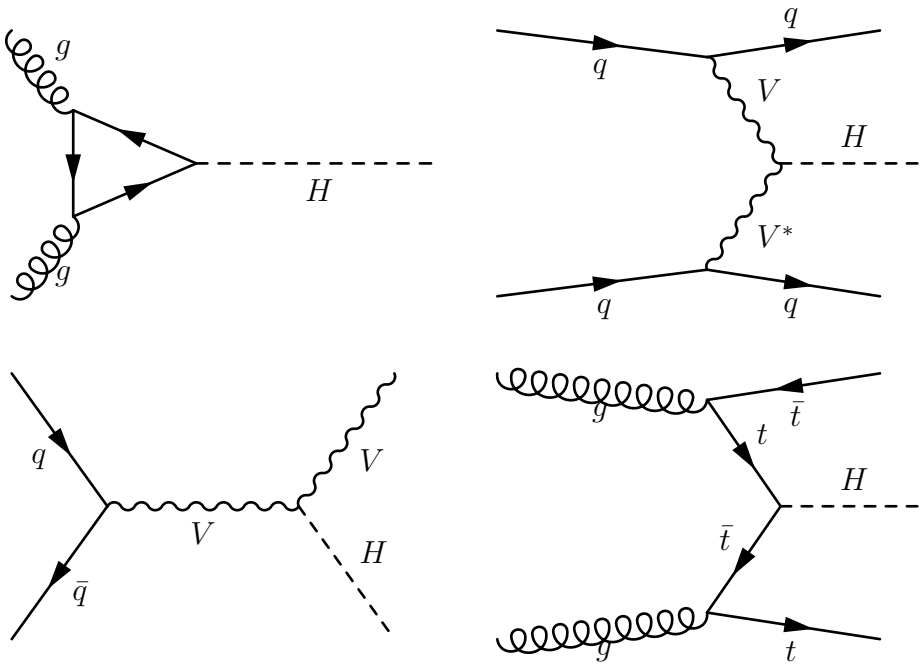

Figure 1.4: *The Feynman diagrams representing the different production channels for the Higgs boson in proton-proton collision: gluon fusion, vector boson fusion, associate production with an intermediate vector boson and the associate production with a top pair.*

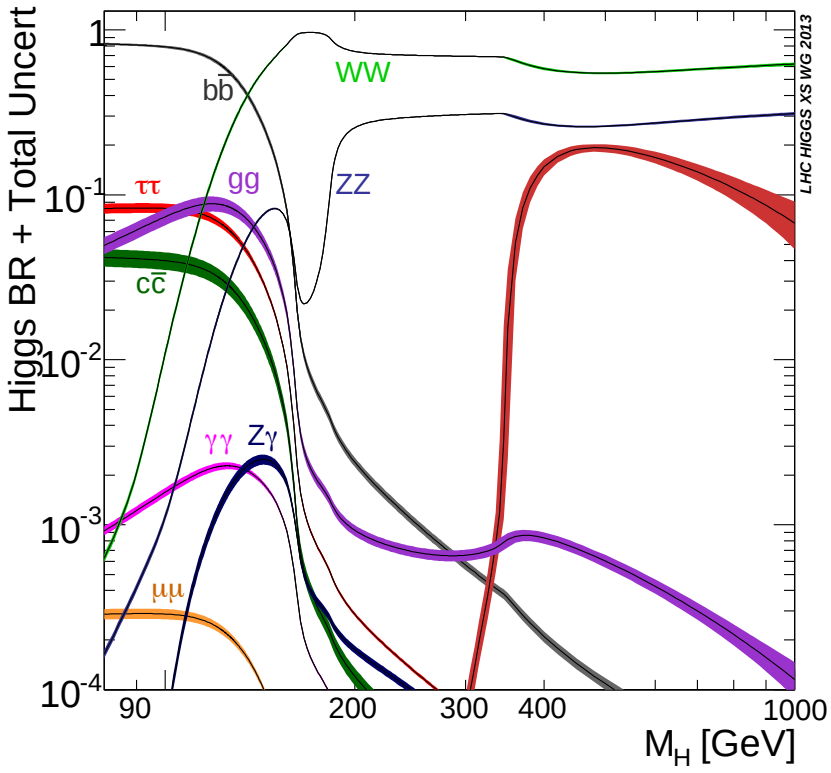

Figure 1.5: *The Standard Model Higgs boson decay branching ratios for different Higgs mass values. Figure supplied by the LHC Higgs Cross Section Working Group* `https://twiki.cern.ch/twiki/bin/view/LHCPhysics/CrossSections`.

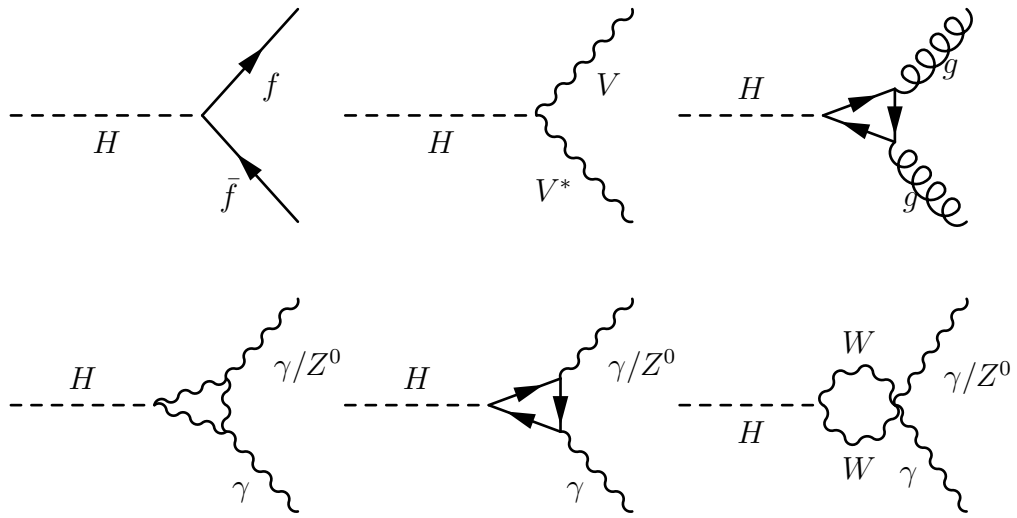

Figure 1.6: *The Feynman diagrams representing the Higgs boson decay channels at lowest orders: production of a $f\bar{f}$ pair ($f = b, \tau, c, \mu$), production of a weak vector boson pair, production of a gluon pair, and production of a $\gamma\gamma$ or a γZ^0 pair.*

CHAPTER 2

Higgs to Flavour, the latest results

This chapter provides a brief and concise overview of what are the latest results concerning the Higgs boson couplings, published by the two general-purpose experiments at LHC: ATLAS and CMS. The discussion will focus solely on the Yukawa coupling with fermions, this being the focus of this thesis. The specific details of the different works will not be addressed since this will go beyond the point of this thesis. Thus, I will list and point the reader to a series of papers on the subject, highlighting the main results these analyses quote.

2.1 The Data collected by the LHC

The scheduling of the operation at LHC is very straighforward and is illustrated in figure 2.11: there are several years-long data-taking campaigns, which are labelled as "Run-X" (with X an integer number), spaced out by few-years-long technical stops, denoted as "Long Shutdowns" (LS). During these periods of no operations, the accelerator system and the collider undergo a series of improvements for the next data-taking campaign.

As of now, we have concluded the so called "Run-1" and "Run-2" data-taking periods. The former covers 2011 and 2012, during which the ATLAS experiment collected about $25 fb^{-1}$ of data; while the latter spans from 2015 to 2018, during which the ATLAS collaboration collected about $150 fb^{-1}$ of data. During these years the center-of-mass energy was upgraded from 7 TeV (during 2011), to 8 TeV (during 2012) and to 13 TeV (during 2015-2018). The breakdown of the luminosity collected by the ATLAS experiment during the years is shown in figure 2.2. The total amount of luminosity of data, declared usefull for physics analysis, that the ATLAS collaboration collected can be found on table 2.1.

Starting from 2019 the preparation for Run-3 data-taking period will begin, with the aim of increasing the center-of-mass energy to 14 TeV and to double the current nominal luminosity. And starting from 2024 the High

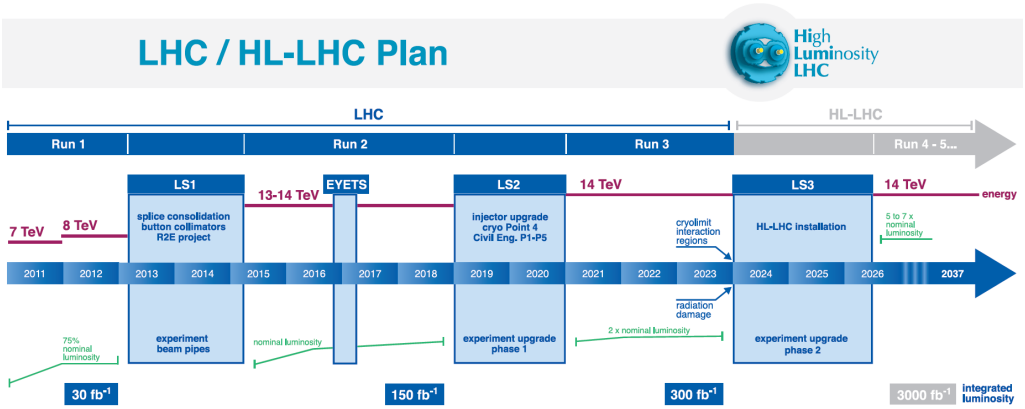

Figure 2.1: *Scheduling of the operations at LHC, from the Run-1 campaign to the High Luminosity LHC phase. The operating conditions (instantaneous luminosity and center of mass energy) are reported for the different phases of data-taking. Image taken from* `https://ep-news.web.cern.ch/content/weighing-lhc\OT1\textquoterights-future`.

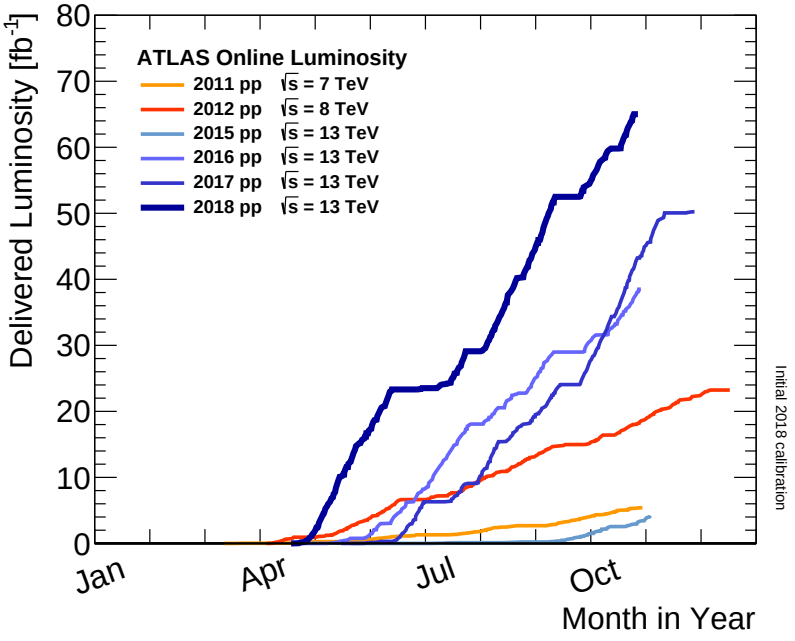

Figure 2.2: *Delivered Luminosity by the ATLAS experiment during Run-1 (2011-2012) and Run-2 (2015-2018) data taking periods. Image taken from* `https://twiki.cern.ch/twiki/bin/view/AtlasPublic/LuminosityPublicResultsRun2`

Year	Center of Mass Energy [TeV]	Luminosity $[fb^{-1}]$
2011	8	~ 5
2012		~ 20
2015	13	~ 3
2016		~ 36
2017		~ 43
2018		~ 61

Table 2.1: *The amount of luminosity of data, collected by the ATLAS experiment during the Run-1 and Run-2 campaigns, and declared useful for physics.*

.

Luminosity-LHC (HL-LHC) will begin. In this phase the nominal luminosity will be substantially increased up to 5 or 7 times the level during 2016.

The enormous amount of data collected so far was analysed by the experiments at LHC, leading to the publication of several papers on a huge variety of topics. The results so far have been outstanding. Just to mention one : the Higgs boson was discovered by the ATLAS and CMS collaborations in 2012 [41, 42].

2.2 Our knowledge of the Yukawa coupling with fermions

Despite the several studies targeting the Higgs Boson, not all its properties have been established mainly due to insufficient statistics. The status of our knowledge of the Yukawa Coupling is very different between the bosonic and the fermionic sectors. The former benefits from leptonic decays and clear trigger signatures, and as such we are now in the process of performing precision measurements of the coupling. Conversely, little we know about the latter: albeit we have recently achieved the observation of the Yukawa coupling with top [43, 44] and bottom quarks [45, 46] and with tau leptons [47, 48], we do not have yet the evidence for the other couplings. As of now, only the Yukawa couplings with the third and second generations – with the exception of strange quarks – can be investigated at the LHC.

In what follows, I summarize the latest results published by the ATLAS and the CMS collaborations concerning the Higgs boson coupling with fermions. The majority of these analyses, with a notable exception that will be mentioned, rely on the same base strategy: the use of multivariate techniques in order to improve the sensitivity; and a profile likelihood fit for the signal extraction. The interested reader will find all the necessary details, for each analysis, in the referenced papers.

2.2.1 Coupling with top quark

Indirect studies suggested that the Higgs boson coupling to top quarks is SM-like. This was deduced by the overall agreement with the SM prediction for the rate of Higgs boson production through gluon-gluon fusion and for the $H \to \gamma\gamma$ decay mode: in both processes the quantum loops include top quarks. However, non-SM particles may contribute in the loops, thus masking possible deviations from the SM.

The unique peculiarity of the top-quark Yukawa coupling is that it cannot be tested from the measurements of the Higgs boson's decay rate, since on-shell top-quarks are too heavy to be produced in Higgs boson decays. The constraints on the coupling can be obtained through the measurement of the $pp \to t\bar{t}H$ production process. The Higgs to di-top vertex is indeed present in the production channel in association with top quarks, which gives rise to a wide variety of final-state event topologies. A measurement of the production rate of the tree-level $t\bar{t}H$ process would be the best way of investigation. As such, direct searches for the Yukawa coupling with top quarks target the $t\bar{t}H$ production channel in all the possible decay modes.

Recently, the *ATLAS* and *CMS* collaborations both reported the observation of the Yukawa coupling with top quarks [43, 44]. This result was achieved by combining the data collected at $\sqrt{s}$ =7, 8 and 13 TeV, which correspond of the 2011, 2012, 2016 and 2017 (for the ATLAS experiment only) data-taking years. The presence of a $t\bar{t}H$ signal has been assessed by performing a simultaneous fit to the data from the different decay modes (e.g. $H \to b\bar{b}$, $H \to \gamma\gamma$, $H \to WW/ZZ$ and $H \to \tau^+\tau^-$). This resulted in a measured signal strength, $\mu \equiv \sigma_{measured}/\sigma_{SM}$, of $1.32^{+0.28}_{-0.26}$ for the ATLAS collaboration, and $1.26^{+0.31}_{-0.26}$ for the *CMS* collaboration, corresponding in an observed (expected) significance of 6.3σ (5.2σ) and 5.2σ (4.2σ) respectively. The results are summarized in figure 2.3, broken down in the different decay channels considered. Also, the year-by-year evolution of the significance of the *CMS* analysis is shown.

More specified investigation of the Yuakawa couping can be found in [49, 50], which target the $t\bar{t}H, H \to b\bar{b}$ process, and [51, 52], which focus on the H to multi-lepton channels. However, these specific cases are not enough to reach the 5σ threshold alone, which has been obtained when combining the different channels.

An additional piece of information concerning the top Yukawa coupling can be obtained by a search for the associated production of a Higgs boson and a single top quark (tHq), performed by the CMS collaboration [53]. The peculiarity of this paper is that it provides some information on the relative sign of the top-Higgs coupling modifier (k_t) and the coupling modifier of vectors bosons to the Higgs (k_V), while all the previously cited papers focus on the magnitude of the coupling. The SM predics a same-sign scenario, thus a negative relative sign of the couplings will indicate the presence of non-SM phenomena. At the present moment no deviation from the SM has been observed and studies from the decay rate of Higgs to photon pairs [54] and the cross section for associated production of Higgs and Z bosons via

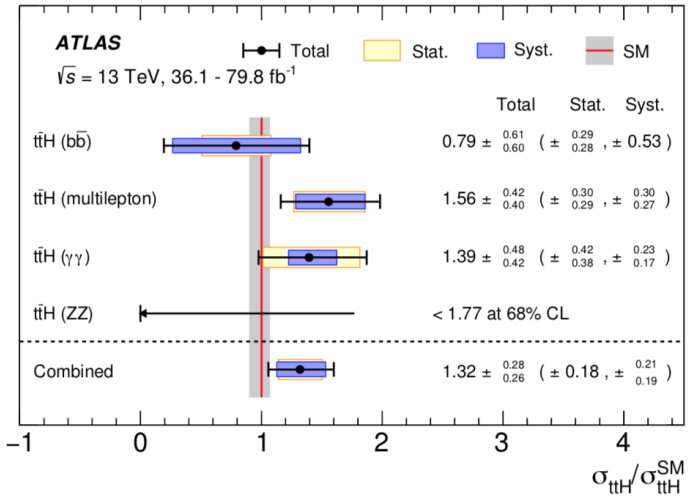

(a)

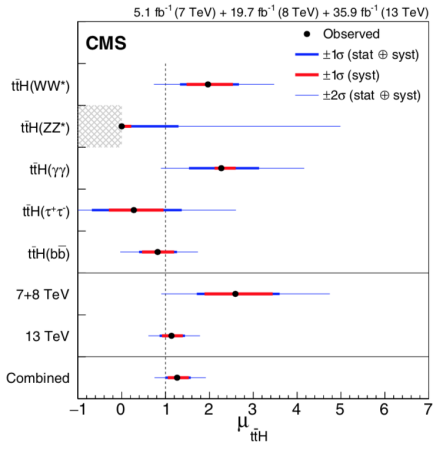

(b)

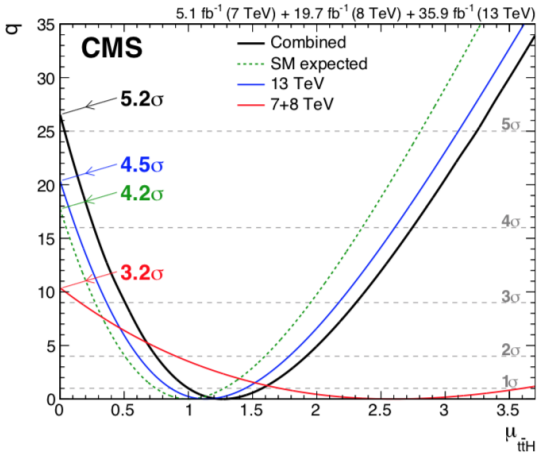

(c)

Figure 2.3: *Combined $t\bar{t}H$ production cross section, as well as cross sections measured in the individual analyses, divided by the SM prediction for both the ATLAS (a) and the CMS (b) collaborations. The total uncertainties, and the statistical and systematic uncertainties, are reported. (c) Test statistic q as a function of $\mu_{t\bar{t}H}$ for all decay modes at all center of mass energies. The expected SM result for the overall combination is also shown. The horizontal dashed lines indicate thep values for the background-only hypothesis obtained from the asymptotic distribution of q, expressed in units of the number of standard deviations.*

gluon fusion [55] disfavour negative signs of couplings.

Scenario	Channel	Obs. Limit (pb)	Exp. Limit
$k_t/k_V = -1$	$b\bar{b}$	6.07	$3.06^{+1.58}_{-0.97}$
	$\gamma\gamma$	1.31	$1.28^{+0.58}_{-0.36}$
	$\mu\mu + e\mu + \ell\ell\ell$	0.87	$0.82^{+0.39}_{-0.25}$
	Combined	**0.86**	$\mathbf{0.59^{+0.26}_{-0.17}}$
$k_t/k_V = 1$ (SM-like)	$b\bar{b}$	8.29	$3.83^{+1.97}_{-1.22}$
	$\gamma\gamma$	5.17	$3.59^{+1.46}_{-0.91}$
	$\mu\mu + e\mu + \ell\ell\ell$	1.40	$1.26^{+0.57}_{-0.37}$
	Combined	**2.04**	$\mathbf{1.04^{+0.43}_{-0.29}}$

Table 2.2: *Expected and observed 95% C.L. upper limits on the tH production cross section times $H \to WW + \tau\tau + ZZ + b\bar{b} + \gamma\gamma$ branching ratio for a scenario of inverted couplings ($k_t/k_V = -1.0$) and for a standard model-like signal ($k_t/k_V = 1.0$), in pb.*

2.2.2 Coupling with bottom quark

Despite the Branching Ratio of 58% – which makes the Higgs decay mode to bottom quark pairs the dominant one – the overwelming QCD background at Hadron Colliders coming from the direct production of $b\bar{b}$ pairs ($g \to b\bar{b}$) makes this channel a challenging one. Thus, the only reasonable strategy for targeting this decay mode is to exploit the peculiar topologies of the different Higgs production final states at trigger level, thus allowing the analyses to enhance sensitivity to the $H \to b\bar{b}$ process..

The first relevant result on the Higgs coupling to bottom quarks dates back to before the Higgs boson discovery itself. Indeed, the studies conducted at Tevatron showed a local excess of events of 2.8σ in the data compared to the background-only hypothesis in the mass range between 120 and 135 GeV [56], as shown in figure 2.5. Albeit very close to the evidence of such a Yukawa coupling, only the analysis of the data collected at LHC during 2016 and 2017 resulted first in the evidence [57, 58] and then in the observation [45, 46] from both the ATLAS and CMS collaborations independently. In both cases, the observation was achieved by combining all the possible production channels.

The mode with the highest sensitivity is the Higgs-Strahlung (or VH, in which V stands for Vector Boson) – due to the clear leptonic final states – that, alone, is able to reach an observed significance of 4.9σ and 4.8σ for the ATLAS and CMS collaborations respectively. The other channels that contributed to the observation are the associated production with a top pair [49, 50] and the Vector Boson Fusion channel [5, 6, 59], on which this document focuses and that will be described in the following chapters.

The combination of these channels further enhanced the significance, exceeding the conventional 5σ threshold required to be able to proclaim

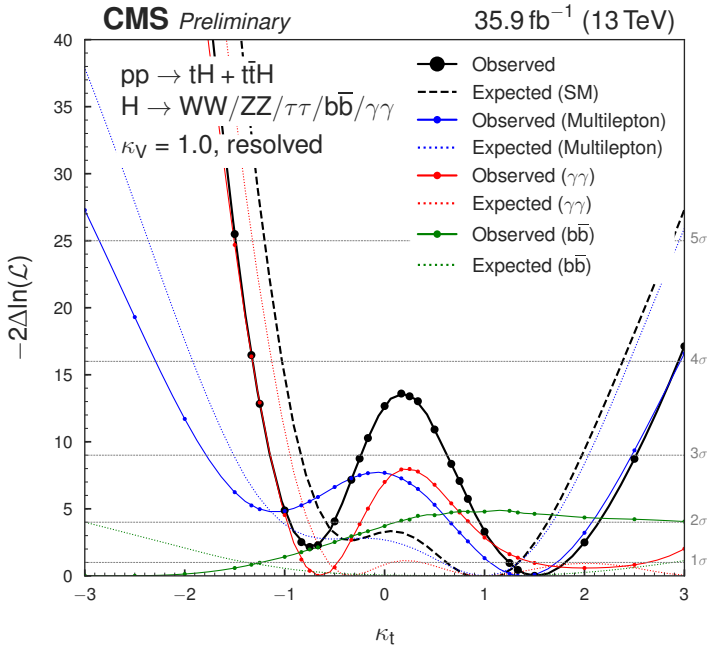

Figure 2.4: *Scan of $-2\Delta ln(\mathcal{L})$ for the combined fit of the $tH + ttH$ signal strength on the data (black line) and the individual channels (blue, red, and green), compared to fits on an Asimov dataset corresponding to the SM expectations (dashed lines). In each point the hypothesis of signal strength equal to one is tested against a fit with floating signal strength.*

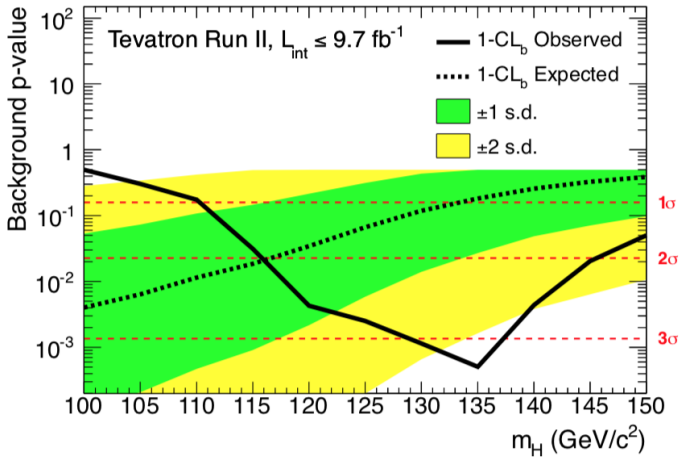

Figure 2.5: *The p-value as a function of m_H under the background-only hypothesis. Also shown are the median expected values assuming a SM signal is present, evaluated separately at each m_H. The associated dark and light-shaded bands indicate the 1σ and 2σ range of possible experimental outcomes.*

the observation: the ATLAS collaboration reported a signal strength of 1.01 ± 0.20, correponding to an observed (expected) significance of 5.4σ (5.5σ); and the CMS collaboration quoted a signal strength of 1.04 ± 0.20, corresponding to an observed (expected) significance of 5.6σ (5.5σ). The results are summarized in figure 2.6, in which the signal strengths for all the different channels, and for their combinations, are reported.

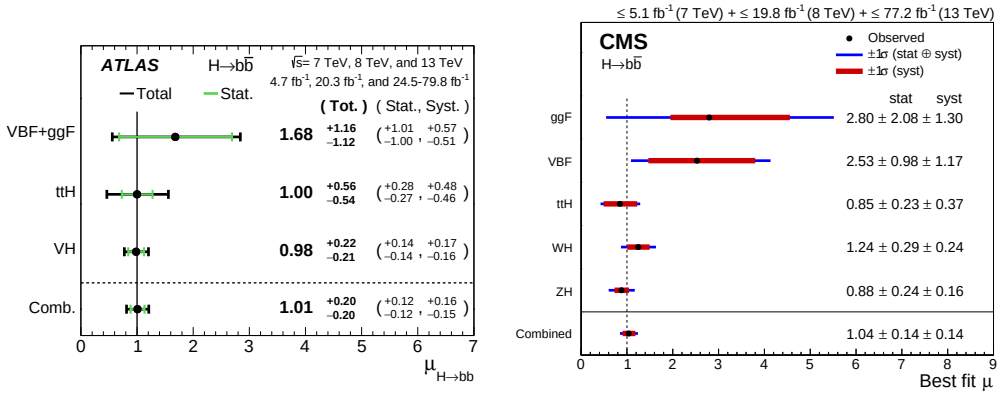

(a) **(b)**

Figure 2.6: *The fitted values of the Higgs boson signal strength parameter $\mu_H \to b\bar{b}$ separately for the VH, ttH and VBF+ggF analyses along with their combination, for both the ATLAS (a) and the CMS (b) collaborations.*

2.2.3 Coupling with charm quark

Measurements of the Yukawa coupling of the Higgs boson to quarks belonging to the second generation are difficult at hadron colliders, due to the small branching fractions, large backgrounds, and challenges in jet flavor identification. The available literature in this context shows that the Yukawa coupling to charm quarks can be probed with rare exclusive decays of the Higgs boson to a light vector meson or quarkonium state and a photon or the decay of the Higgs boson to c-quarks via the decay to $J/\psi\gamma$ [60–64]. These studies resulted in establishing upper limits.

The ATLAS collaboration recently published the very first search for a Higgs Boson decaying to a pair of charm quarks in the Higgs-Strahlung production channel, targeting the final states with two leptons (electrons and muons) : $pp \to ZH \to \ell\ell c\bar{c}$ [65]. The ability to correctly identify jets stemming from charm quarks (c-tagging) represents the main challenge of such a search. The tagging algorithms exploit the lifetimes and decay of hadrons. Unfortunately, c hadrons have characteristics very close to b hadrons, and as a result they are very challenging to correctly identify. However, the ATLAS collaboration performed a pioneering analysis, as far as charm tagging is concerned, by exploiting two multivariate algorithms for discriminating charm quarks from bottom and light quarks (see figure 2.7). The analysis resulted in an observed (expected) upper limit on μ_{ZH} at the 95% CL of 100 (150^{+80}_{-40}) times the SM predictions.

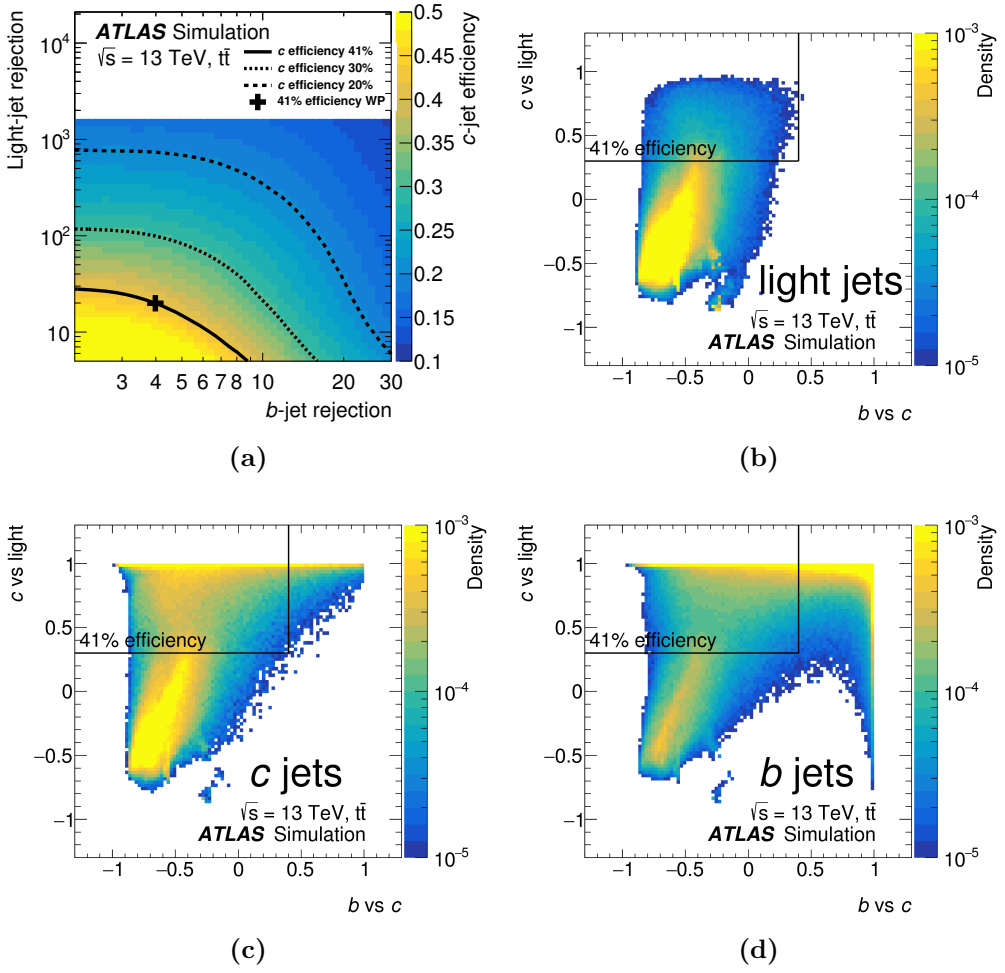

Figure 2.7: *The c-jet-tagging efficiency (colored scale) as a function of the b-jet and l/c-jet rejection as obtained from simulated $t\bar{t}$ events.*

2.2.4 Coupling with tau lepton

The SM Higgs boson decay to a τ lepton pair has the highest branching fraction amidst all leptonic Higgs boson decays. Recently, the ATLAS and CMS collaboration reported independently the observation of the Yukawa coupling with τ leptons [47, 48]. This was achieved by targeting the gluon-gluon fusion and the vector-boson fusion production mechanisms of the Higgs boson in all the possible decays (leptonic and/or hadronic) of the τ leptons.

These complex analyses rely on a few key points : efficient trigger for hadronic τ and light leptons at low p_T; good hadronic τ identification to reject fakes; and advanced techniques for best di-τ mass reconstruction, due to the neutrinos in the final state. While the *CMS* collaboration maintained a multivariate approach, the *ATLAS* collaboration switched to a cut-based approach during 2016. Despite the consequent impact on the uncertainties, *ATLAS* observed a Higgs cross section of $\sigma \times BR = 3.71^{+1.06}_{-0.95}$ *pb*, while *CMS* reported a signal strength of $\mu = 1.09^{+0.27}_{-0.26}$. In figure 2.9 the results obtained from the analysis of only the data collected during 2016 are reported. The combination with the results from Run-1 resulted in an observed (expected) significance of 6.4σ (5.4σ) for the ATLAS collaboration and 5.9σ (5.9σ) for the CMS collaboration.

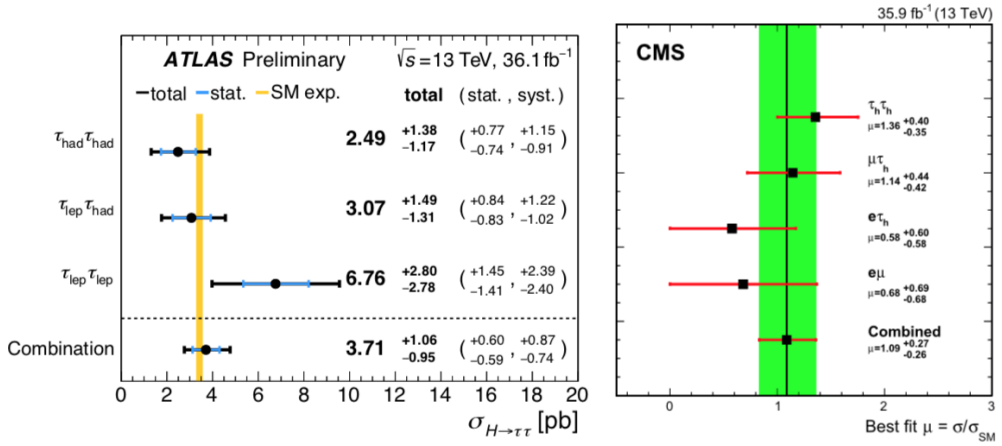

(a) **(b)**

Figure 2.8: *The measured values for the Higgs cross section, $\sigma_{H\to\tau\tau}$, for the ATLAS collaboration (a), and the Higgs signal strength, μ, obtained by the CMS collaborations (b). The result from the combined fit is shown.*

A complementary search conducted by the CMS collaboration, on the data collected during 2016, targets the production in association with a W or a Z boson [66]. These analyses focus on several final states. The ZH channel targets the $Z \to \ell\ell$ (with $\ell = e, \mu$) decays and combines them with the four possible τ leptonic and/or hadronic decay modes. The WH channel considers four final states in which the W boson decays leptonically to neutrinos and an electron or a muon, and at least one hadronic decay of

the τ leptons. Combining the two led to a signal strength of $2.5^{+1.4}_{-1.4}$, which corresponds to an observed (expected) significance of 2.3σ (1.0σ). The combination of the results from this analysis with the results obtained from the other production channels have been performed only considering the data collected during 2016, as shown in figure 2.9 and 2.10. The fitted signal strength corresponds to $1.24^{+0.29}_{-0.27}$, with an observed (expected) significance of 5.5 (4.8).

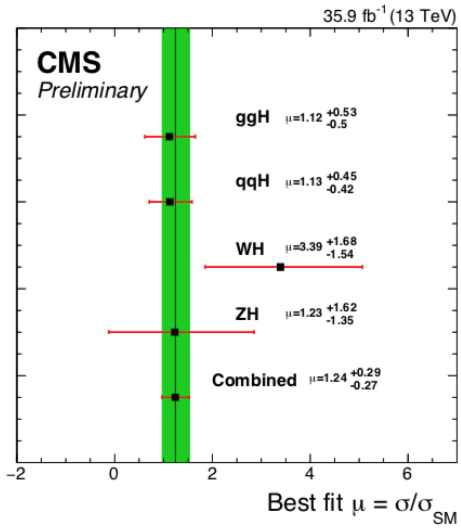

Figure 2.9: *Best-fit signal strength per Higgs boson production process using a combination of the WH and ZH analysis with the CMS analysis performed targeting the gluon fusion and vector boson fusion productions. The constraints from the combined global fit are used to extract each of the individual best fit signal strengths. The combined best fit signal strength is* $\mu = 1.24^{+0.29}_{-0.27}$.

2.2.5 Coupling with muon lepton

The study of the Higgs boson coupling with muons extends the study of the Yukawa couplings to leptons to the second generation. However, the small branching fraction of the $H \to \mu^+\mu^-$ process (2.18×10^{-4}) makes this channel particularly challenging and so far it does not provide enough sensitivity for claiming evidence of the SM process. Physics beyond the the SM [67–69] could enhance the branching ratio. Any deviation from the SM prediction could be a sign of new physics.

For the Yukawa coupling with muons we only set upper limits on the production rate obtained by combining the results from the data recordered at center of mass energies of 7, 8 and 13 TeV [70, 71]. Despite the two collaborations utilizing the data collected up to 2016 and 2017 for CMS and ATLAS respectively, no significant excess is observed above the expected background. The former collaboration observed (expected) upper limits of 2.64 (1.89) times the SM predictions, the latter observed (expected) upper limits of 2.1 (2.0) times the SM predictions.

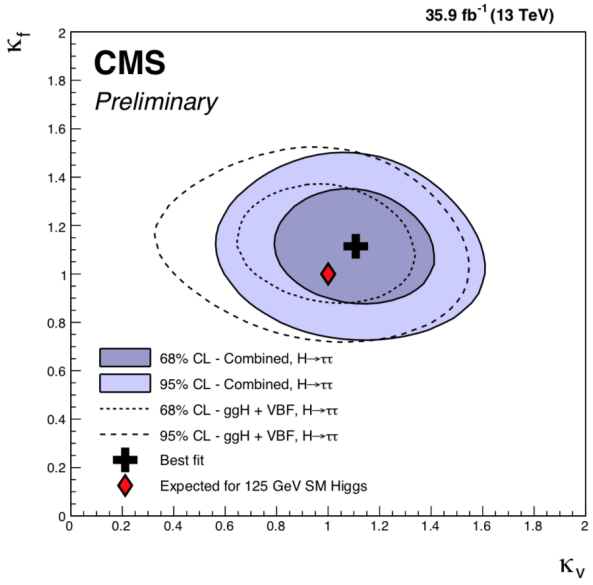

Figure 2.10: *Scan of the negative log-likelihood difference as a function of k_V and k_f. All nuisance parameters are profiled for each point. This scan is a combination of the WH and ZH targeted analysis with the CMS analysis performed in the same data set for the same decay mode but targeting the gluon fusion and vector boson fusion productions. The results for the gluon fusion and vector boson fusion analysis are shown as the overlaid dashed lines. For this scan, the included $H \to WW$ and $H \to ZZ$ processes are treated as signal.*

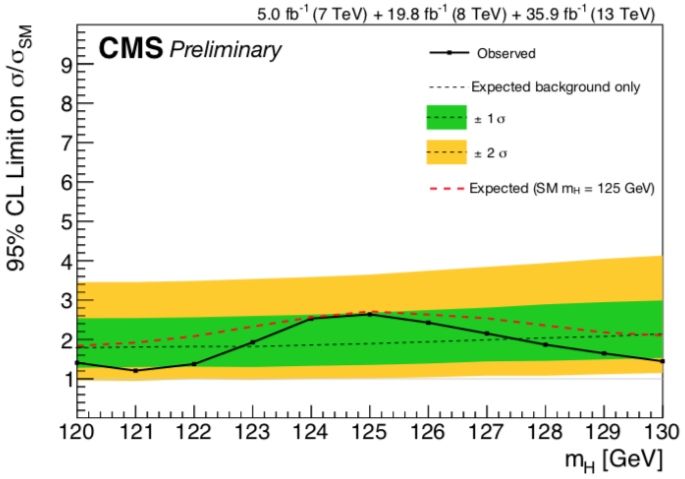

Figure 2.11: *The 95% CL upper limit on the signal strength modifier, μ, for the combination of the 7, 8, and 13 TeV datasets together with the expected limit obtained using the background-only hypothesis and in the signal-plus-background hypothesis (red-line).*

CHAPTER 3

The ATLAS b-Jet Trigger System

The raw input rate of events at LHC is 40 MHz. This impressive amount of events translates into an enourmous amount of data to be stored on disk for being analysed at a later stage. Unfortunately, we do not possess sufficient disk space to store all the events. Thankfully, we are interested only in a few of these events, since the majority of them cannot possess interesting phenomena. The trigger is an essential element for selecting only a few events, but the short bunch-crossing period of 25 ns, together with the need of high efficiency and selectivity, makes this task challenging. Moreover, multiple collisions may occur in the same bunch crossing. Since the phenomena someone is interested change from analysis to analysis, different trigger signatures have been developed. The b-jet trigger is one of these.

This chapter briefly describes the b-jet Trigger system of the *ATLAS* experiment. At first, a general overview of how the Trigger System is structured is provided, before focusing on the b-jet trigger software and characteristics. The *ATLAS* trigger strategy continuously evolved during Run-1 and Run-2 operations, to follow changes in data-taking conditions and analysis needs. In here, I will focus the discussion on the current trigger structure, summarizing the upgrades relevant to the b-jet triggers with respect to the previous years.

3.1 Trigger System

In order to identify and select interesting events amidst the huge amount of proton-proton collisions occurring at LHC, the ATLAS experiment uses a complex trigger system [72, 73]. This is structured as a two-layer system as shown in figure 3.1: a first hardware-based *Level-1 trigger* (*L1*); followed by a software-based *High Level trigger* (*HLT*) – resulting from the merging of the software-based triggers available during Run-1: *Level 2* (*L2*) and *Event Filter* (*EF*).

L1 acts as the first filter and must be able to cope with the huge rate

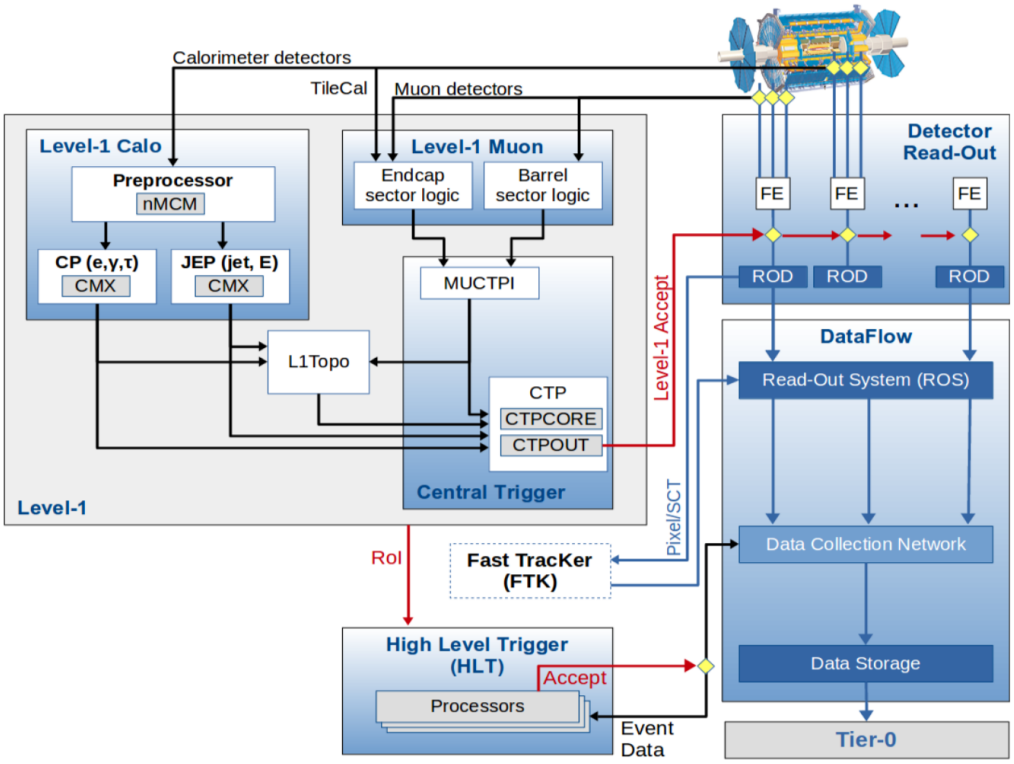

Figure 3.1: *Scheme of ATLAS Trigger System, including the Detector Read-Out and Data Flow systems.*

of inputs it receives. Thus, *L1* is requested to operate at very high frequency and with a very short latency ($\sim 2.5\mu s$), with the aim to reduce the trigger rate from 40 MHz to 100 kHz before the *HLT* kicks in. Using the informations retrieved by the calorimeter systems and the muon detectors – albeit with a reduced granularity – it identifies Regions of Interest (RoI) and, if some selection criteria are satisfied, it passes these to the *HLT*. These criteria are usually some transverse momentum, pseudorapidity and multiplicity thresholds that are defined by the triggers used during the data-taking. More complex criteria can also be applied (flavour tagging discrimant, invariant mass and geometrical separation are only a few of such criteria) according to what phase space the trigger aims at targeting. *L1* consists of four sub-systems: The Level-1 Calo Trigger (L1Calo) [74]; the Level-1 Muon Trigger (L1Muon) [75]; the Central Trigger Processor (CTP) [76]; and the Topological Processor (L1Topo) [77].

HLT analyses the *L1* RoIs using all the detector systems with their full granularity and, according to some additional selection criteria, further reduces the trigger rate to 1 kHz for storage.

All the different complementary selections, called trigger signatures, are gathered in groups and form a Trigger Menu, consisting of O(2000) trigger chains. Trigger chains are a sequence of algorithms that reconstruct physical quantities and take decisions based on their values. The interested reader may refers to [78–80] for a comprehensive description of the Trigger Menu and its evolution during Run-2 data-taking campaign.

During the long shutdown following Run-1 and during Run-2 operations, some upgrades to the detector and the trigger system have been applied, in particular: the addition of the Insertable b-Layer (IBL); and the introduction of the Topological Processor (L1Topo).

The Pixel detector [81] is the innermost part of the ATLAS detector and comprises three barrel layers and three disks on each side to guarantee at least three space points over the full tracking pseudo-rapidity range. The ATLAS IBL [82, 83] is an additional layer (the innermost component of the pixel detectors), installed in May 2014 at a radius of 3.3 cm from the beam axis – the closest tracking device to the beam pipe. The main motivation of the IBL is to maintain or improve the ATLAS performance during LHC operation despite possible irreversible radiation damage effects in the B-Layer of the Pixel detector, as well as the increasing bandwidth requirements resulting from the expected Phase-I LHC peak luminosity. The IBL detector has been successfully operating since 2015 improving the ATLAS tracking performance [84].

By Topological Processor the ATLAS comunity refers to an FPGA board that is part of the L1 Trigger system [77]. It has been introduced during Run-2 in order to cope with the increase in luminosity and the impressive input rate: the algorithms are implemented in VHDL and operated in parallel. It has been designed in order to support the computation of complex physics variables on which we can apply some selection criteria. It receives as inputs both L1Calo and L1Muon information and it allows a trigger decision to be made using more than just p_T or E_T, by exploiting the geometric and kinematic relationships between Trigger OBjects (TOBs) and event-level quantities. These decisions can be grouped in three categories: angular separation; invariant mass; and hardness of interaction.

If we restrain the discussion to the subject of this thesis, the VBF $H \to b\bar{b}$ analysis exploited L1Topo by adopting triggers that allow the computation of the invariant mass between jets (m_{JJ} or INVM) and the scalar sum of the p_T of Jets (HT)[1]. It we label with (i) the physical quantities of the i-th jet, these are defined as:

$$m_{JJ} = \sqrt{2E_T^{(1)}E_T^{(2)}\left[cosh(\eta^{(1)} - \eta^{(2)}) - cos(\phi^{(1)} - \phi^{(2)})\right]} \tag{3.1}$$

$$HT = \sum_i p_T^{(i)} \tag{3.2}$$

During the L1Topo commissioning phase, I personally took care of the validation and sign off of the INVM and HT L1Topo triggers, as well as the HLT triggers used by the VBF analysis that rely on L1Topo.

[1]ATLAS uses a right-handed coordinate system with its origin at the nominal interaction point (IP) in the centre of the detector and the z-axis coinciding with the axis of the beam pipe. The x-axis points from the IP to the centre of the LHC ring, and the y-axis points upward. Cylindrical coordinates (r,ϕ) are used in the transverse plane, ϕ being the azimuthal angle around the beam pipe. The pseudorapidity is defined in terms of the polar angle θ as η = -ln tan(θ/2). This is calculated relative to the primary vertex.

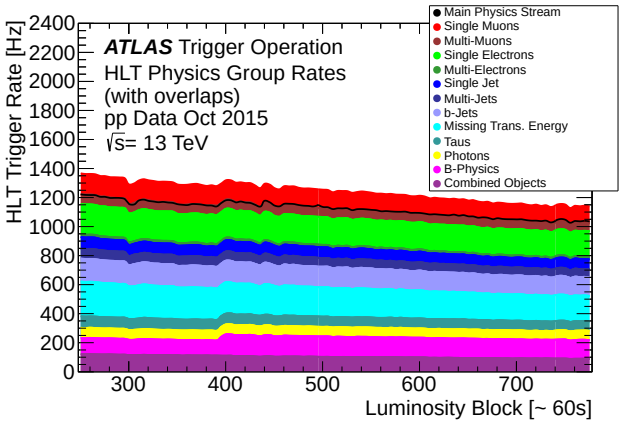

(a)

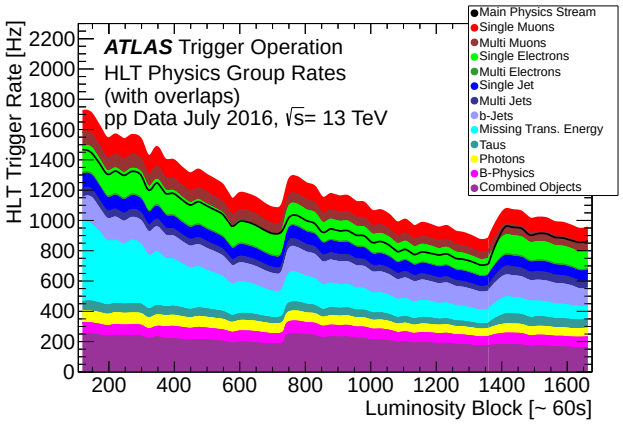

(b)

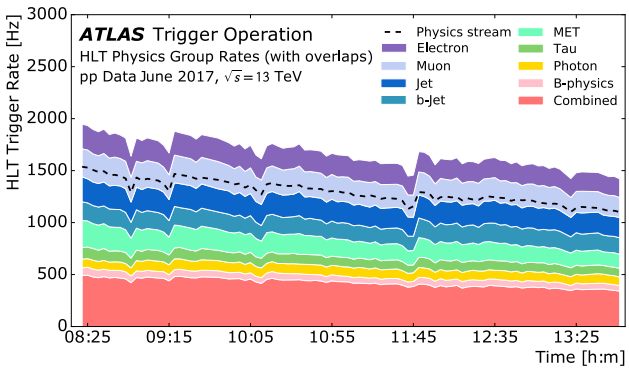

(c)

Figure 3.2: *Physics trigger group rates at the High Level Trigger (HLT) as a function of time in fills taken in 2015, 2016 and 2017. Presented are the rates of the individual trigger groups specific to trigger physics objects. Each of the groups contain single and multi triggers of the same object. The combined group represents multiple triggers of different objects, as combinations of electrons, muons, taus, jets and missing transverse energy. Common features to all rates are their exponential decay with decreasing luminosity during an LHC fill. The rates periodically increase due to change of prescales to optimise the bandwidth usage or LHC luminosity re-optimisations, dips are due to deadtime and spikes are caused by detector noise.*

3.2 b-Jet Triggers

The b-jet triggers exploit flavour tagging algorithms in order to identify at online level if a jet is likely to have been produced by heavy flavour quarks. Starting from January 2018, I am acting as the coordinator of the b-jet trigger signature of the ATLAS experiment. The aim is to assure the ability to run the jet flavour-tagging algorithms in the online environment for use in trigger chains while maintaining as low as achievable a resource usage in the HLT. The physics analyses that rely on this kind of triggers are characterized by the presence of b-hadrons in their final states. As a result, b-jet triggers are widely used in ATLAS, both for measurements within the Standard Model and for searches of new phenomena; the VBF $H \to b\bar{b}$ channel is one of the analyses that exploits them the most.

Discriminating a beauty jet from charm and light jets relies on exploiting the properties of b-hadrons: the long lifetime, which leads to a displaced (or secondary) vertex – typically a few mm from the primary vertex; the large impact parameter; the large mass; and the possible semi-leptonic decays of b-hadrons to electrons or muons (branching ratio $\sim$40%). Pinpointing the correct position of the primary and secondary vertices is pivotal. Tracking algorithms have been developed in order to perform track and vertex reconstruction. Tracking is extremely CPU expensive, so b-jet triggers are the highest CPU consumer amidst all the trigger signatures. As such, they – more than the other trigger signatures – must be able to balance performance and resource consumption in order to remain within the technical operational constraints.

An early rejection of events is the key to achieve this: we can stop the algorithm sequence as soon as we identify an event as lacking interesting phenomena. Thus, the trigger decision process is divided into multiple sequential steps – each step using greater granularity than the previous ones and different CPU consumptions. Also, the management of information is optimized in order to minimize the impact on the CPU, by computing and caching event level quantities. In this perspective, the structure of the b-jet trigger chains and the ordering of algorithms have undergone a series of changes during Run-1 and Run-2. These changes are: the availability of new tracking algorithms, to perform track reconstruction following a two-step approach (see section 3.2.1); a new calibration of the impulse of jets, called Global Sequential Calibration (see section 3.2.2); and the use of the offline software and taggers for flavour tagging (see section 3.2.3).

At present, the b-jet triggers foresee the following sequence of steps:

- Fast track reconstruction to be performed on the ensemble of L1 RoIs in order to identify the primary vertex coordinates. Since the primary vertex is a event-level information, it is computed only once in an event and cached so that it can be used in all b-jet chains.

- Jets are reconstructed from the information retrieved by the calorimetric system and a preliminary constraint on their p_T is applied.

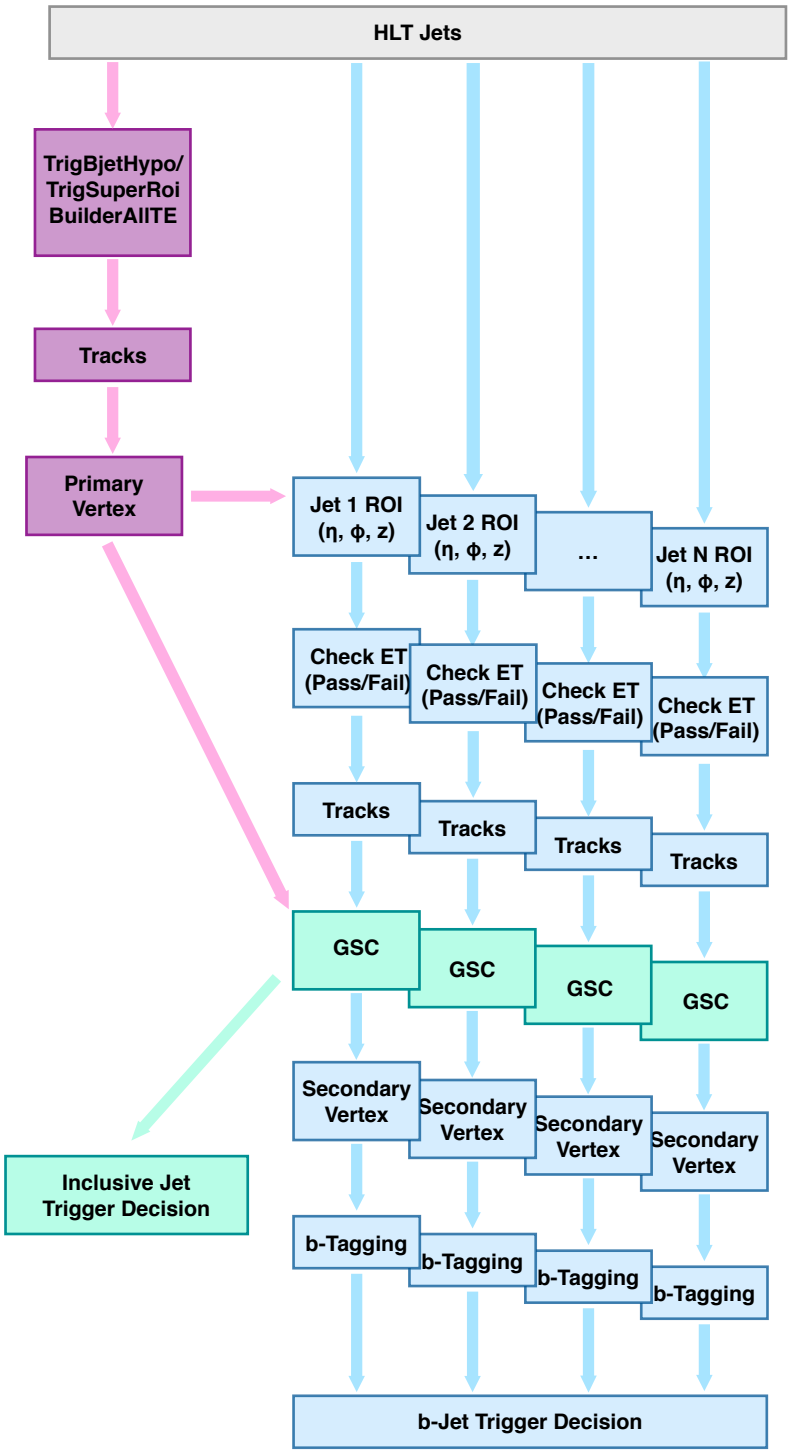

Figure 3.3: *Sequence of the algorithms that constitute the b-jet chains.*

- By imposing a constraint on the position of the Primary Vertex, the tracks associated to the reconstructed jets are measured precisely. Exploiting these reconstructed tracks, the Global Sequential Calibration is computed for each jet and another constraint is applied on the newly-calibrated p_T
- Secondary vertex is reconstructed and flavour tagging algorithms are run.

A schematic of the workflow is shown on figure 3.3. In addition to these pure b-jet triggers, the trigger menu also comprises combined b-jet and muon chains for use in flavour tagging calibration. The schematic of the workflow is similar to the previous one, with the exception of the muon reconstruction algorithms and the ΔR matching between jets and muons that is requested to assure overlapping between jets and muons.

3.2.1 Track Reconstruction Algorithm

During Run-1 operations, the track reconstruction was performed by processing separately the regions of the detector that were selected by the L1 trigger. Albeit such an approach is functional in a low pile-up environment, it is not advisable once the number of collisions occurring in parallel grows and the L1 RoIs start overlapping. In this scenario the same reconstruction algorithm is run multiples time in the same regions of the detector, thus leading to a series of unpleasant downsides: wasting CPU resources and potentially biasing on the primary vertex finding, by double-counting tracks in overlapping regions.

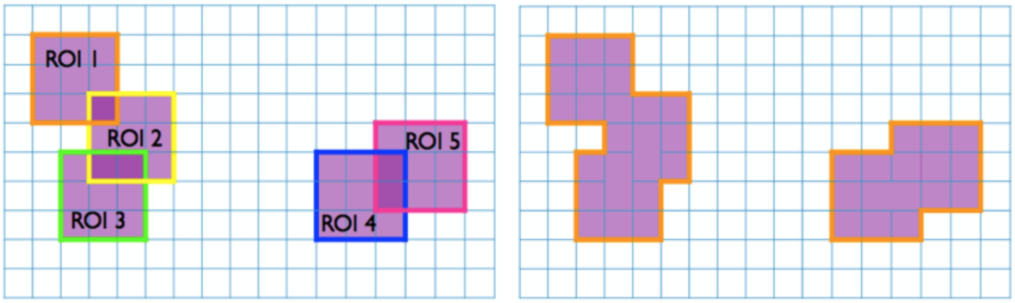

Figure 3.4: *Cartoon describing the construction of the "Super-RoI". On the left, the L1 RoIs in the $\eta-\phi$ plane may overlap, especially in a high pile-up unvironment. On the right, the overlapping L1 RoIs are merged into "Super-RoIs'.'*

As such, in 2016 a new track reconstruction algorithm has been introduced that relies on a two-step approach. The first step is the "fast tracking", in which the overlapping L1 RoIs are merged into a so-called "Super-RoI" (so that the same region of the detector is not processed multiple times) on which a fast reconstruction of tracks is performed, with the aim to identify the primary vertex position. The second step is the "precision tracking", that perform the track reconstruction on the original L1 RoI

that constitute the "Super-RoI", with the additional and strong constraint of the primary vertex.

This resulted in a more robust and reliable track reconstruction, with clear impact on the online flavour tagging capabilities of the ATLAS experiment. Also, this guarantees the possibility of applying an additional filter between the two levels: RoIs with no tracks pointing to the primary vertex are not taken into account.

3.2.2 Global Sequential Calibration

Jet reconstruction is based on calorimeter-based objects, whose local properties – together with global properties of the jets – bring the jet energy measurement to its calibrated scale. Jet structure variables affect the jet response of the ATLAS detector, and it can be improved by combining the calorimeter-based measurements with charged particle properties measured with the Inner Detector. The Global Sequential Calibration (GSC) [85, 86] has been introduced in 2017 for reducing fluctuations in the jet energy measurement and, thus, improving the jet energy resolution in the HLT. It is a sequential jet calibration that uses the transverse and longitudinal properties of the jet structure (longitudinal shower shapes of jets, and characteristics of associated tracks) in order to correct the energy scale of jets and provide a better energy resolution. Thus, it allows to correct from the dead material and non-compensation effects of the ATLAS calorimeters.

In terms of performance measurement we can define the "trigger jet efficiency" as the percentage of offline jets that satisfy a specific trigger. This can be expressed as a function of the jet p_T – a turn-on curve – as shown in figure 3.5. The sharper the turn-on, the better it is: the maximum trigger efficiency is reached at lower offline jet p_T, and this allows analyses to lower their p_T requirements, thus accessing a larger phase space and increasing the selected statistics.

The are two different GSC versions available: the first one using only the information from calorimeters; the other one using also tracks associated to jets. The latter provides improved performances with respect to the former, with sharper p_T turn-ons, as shown in figure 3.5. As of now, b-jets are the only signature that can afford to use this improved GSC correction: primary vertexing and precision tracking are the highest CPU-consuming activities, but they are required in order to perform b-tagging.

In order to reduce the resource load, b-jet chains foresee a sequence of two p_T cuts: one performed on non-calibrated jets reconstructed from calorimeters; another performed on GSC-corrected jets. Such a two-step approach has been required to avoid performing precision tracking on jets that cannot possibly satisfy the second p_T cut once calibrated, due to the magnitude of the GSC correction. The values of the p_T thresholds have been tuned by analysing the efficiency turn-on curves of the GSC-corrected p_T, reported on figure 3.6. This shows, for instance, that all jets with a GSC-corrected $p_T > 55$ GeV possess a non-calibrated $p_T > 45$ GeV.

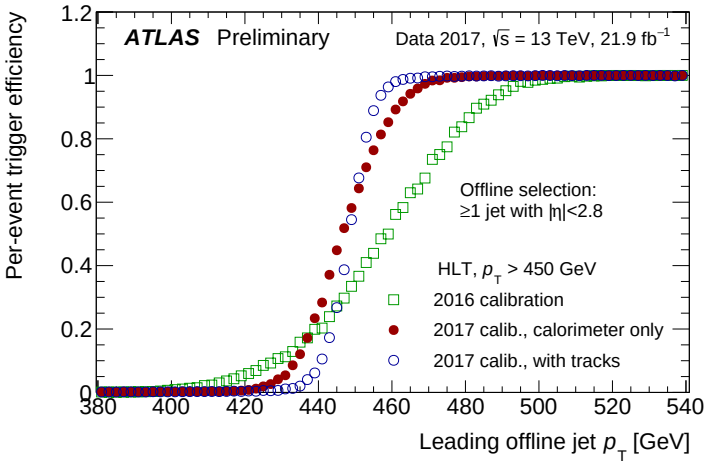

Figure 3.5: *Leading offline jet p_T turn-on curves for different jet calibrations and for $p_T > 450$ GeV. The jet calibration during 2017 introduced the Global-Sequential-Calibration (red and blue dots) and significantly improved the turn-on with respect to the 2016 calibration (green dots).*

Thus, it is a waste of resources to compute precision tracking for jets with $35 < p_T < 45$ GeV.

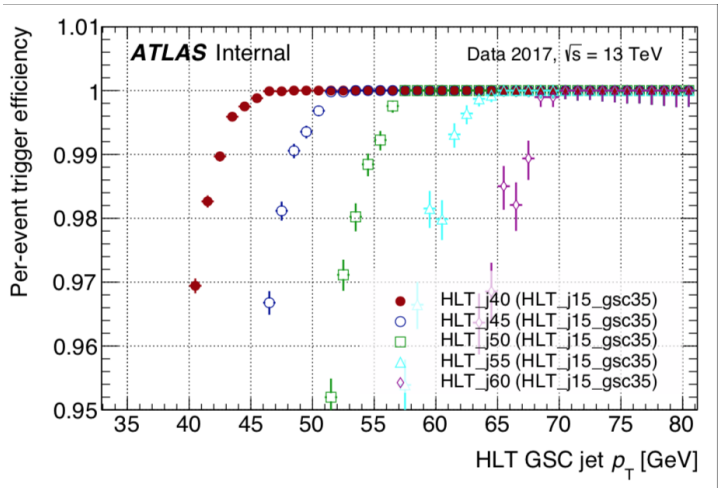

Figure 3.6: *GSC-calibrated jet p_T turn-on curves for different cuts on the non-GSC-calibrated p_T. Efficiency is here defined as the percentage of GSC-calibrated jets also satisfying a specific p_T cut on their non-GSC-calibrated energy (defined by the HLT_jXX triggers).*

3.2.3 Flavour tagging algorithms

The differences between b- and light-jets is reflected in several physical quantities (such as secondary vertex, mass, shower shape etc.), bringing different and complementary – albeit partially correlated – information that must be combined together. A first level of combination is performed with likelihood-based taggers, while Multivariate Techniques take care of the fi-

nal combination in order to produce the discriminating variable. As such, an impressive suite of algorithms have been developed that differ from one another via: the use of different multivariate techniques; the information used; and the different levels of complexity of the algorithms. Currently, likelihood-based taggers and Boosted Decision Trees are predominantly used for flavour tagging, but the ATLAS community is moving toward the use of more complex strategies such as Deep Learning or Recurrent Neural Networks [87]. The training phase is performed on two simulated samples of b-jets (signal hypothesis) and light- and c-jets (background hypothesis) obtained from simulated $t\bar{t}$ events. We identify three base taggers being used:

- **IP3D**: Uses information about the transverse and longitudinal impact parameter (IP) significances. It computes the probabilities that a jet is resulting from the fragmentation and the hadronization of a bottom or up quark (respectively pb^{IP3D} and pu^{IP3D}), as they have been inferred by the IP3D algorithm.

- **SV1**: Reconstructs the secondary vertex (SV) in the jet and uses information about the SV mass, the fraction of the sum of the transverse momentum (pt) of tracks associated to the SV to the sum of the p_{T} of all tracks in the jet ($\Sigma(p_{\mathrm{T}}^{\mathrm{SVtracks}})/\Sigma(p_{\mathrm{T}}^{\mathrm{Alltracks}})$), the number of two-track vertices in the jet, and the ΔR between the jet direction and the direction along the PV-SV axis. It computes the probabilities that a jet is resulting from the fragmentation and the hadronization of a bottom or up quark (respectively pb^{SV1} and pu^{SV1}), as they have been inferred by the SV1 algorithm.

- **Jet Fitter**: Reconstructs the complete b-hadron decay chain, exploiting the topological structure of weak b- and c-hadron decay inside jet. It uses a Kalman filter [88] to find a common line from the primary vertex, through the b vertex, to the vertex decay chain. Thus, it separates b- and c-hadron vertices and computes the discriminant properties.

Tagging algorithms resulting from the combination of these approaches prove to be more versatile and powerful. ATLAS uses two of them:

- **MV1**: Neural network that combines the output of IP3D, SV1 and IP3D+JetFitter[2] exploiting the little correlations between the IP3D and the secondary vertex-based weights, together with the different correlations for b-jet and the light-jet samples of IP3D+JetFitter weight and SV1.

- **MV2**: A Boosted Decision Tree discriminant that combines the output of IP3D and Jet Fitter with the inputs of SV1. Amidst its inputs there are also p_T and η of the jets, providing information in interpreting the separation power of the variables from the low-level taggers.

[2]The IP3D+JetFitter algorithm is the JetFitter algorithm itself, with the IP3D output weight as an additional input node. It is also referred to as JetFitterCombNN.

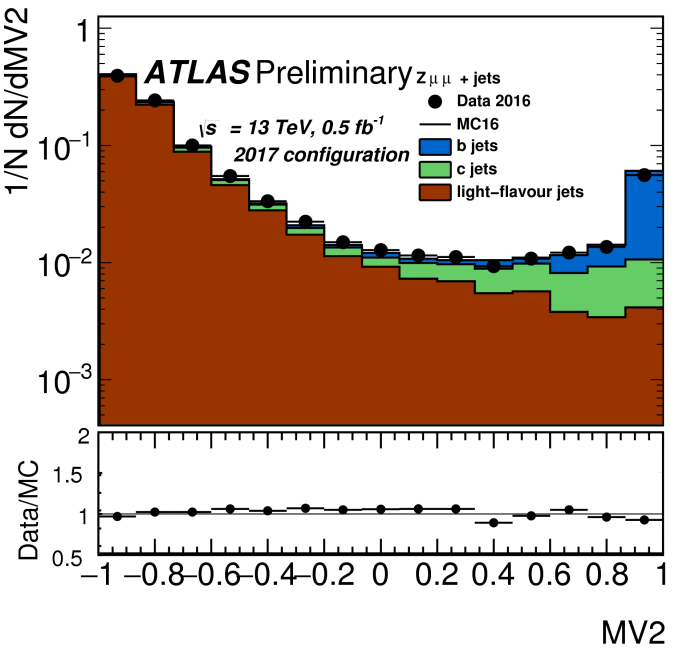

Figure 3.7: *Data-MC comparison of the offline MV2 output of for the 2017 configuration.*

Online flavour tagging

The use at trigger level of the offline flavour tagging software is highly desirable since it centralizes the developments of the algorithms and it maximises the correlation between online and offline flavour tagging. Nowaday, the b-jet trigger code can be though as a wrapper of the offline flavour tagging code. However, the two environments perform b-tagging on jets reconstructed with a different quality of the information. As such, two different ad-hoc training (or tunings) for the same algorithms are required in order to achieve the optimal performances at both levels.

Up to 2015, the online and offline environments were poorly correlated, with the b-jet trigger using some dedicated flavour tagging algorithms that differed from the offline taggers. This online-dedicated tagger was defined as a function of the outputs of IP3D and SV1, and is commonly referred to as "IP3D+SV1". The "IP3D+SV1" tagger weight was defined as

$$\begin{cases} 50; & \frac{pb^{IP3D}/pu^{IP3D} * pb^{SV1}/pu^{SV1}}{1+pb^{IP3D}/pu^{IP3D} * pb^{SV1}/pu^{SV1}} > 1 \\ -\log_{10}\left(1 - \frac{pb^{IP3D}/pu^{IP3D} * pb^{SV1}/pu^{SV1}}{1+pb^{IP3D}/pu^{IP3D} * pb^{SV1}/pu^{SV1}}\right); & otherwise \end{cases} \tag{3.3}$$

In the 2016-2018 period, the online-offline gap was severely reduced by the adoption of the same algorithms at both levels: MV2. However, the use of different tunings for the two environments results in difference performances even if the same tagger is considered. There are however two different versions of the MV2 algorithm. The difference resides in the training sample used.

- **MV2c10**: The background training sample is composed by light jets (90%) and c-jets (10%)

- **MV2c20**: The background training sample is composed by light jets (80%) and c-jets (20%)

Table 3.1 summarizes the different taggers used at both online and offline level during the Run-1 and Run-2 campaigns.

Year / Run	Online Algorithm	Offline Algorithm
2011	IP3D+SV1	MV1
2012	IP3D+SV1	MV1
2015	IP3D+SV1	MV2c20
2016	MV2c20	MV2c10
2017	MV2c10	MV2c10
2018	MV2c10	TBD

Table 3.1: *Flavour tagging algorithms used at online and offline levels for all the data-taking periods considered in this thesis. With the exception of 2017, the two environments always used different flavour tagging algorithms. For 2018, the recommended offline algorithm to be used in analyses has yet to be decided (TBD).*

3.3 Performances

At online level, b-tagging performances are represented by: light-jet and c-jet rejection curves, expressed in terms of b-jet efficiency; and by online efficiency with respect to the offline b-tagging. Concerning the latter, we can define as D the offline jets that satisfy a specific offline b-tagging working point and as N the subset of these offline jets that are also matched to online jets that satisfy a specific online b-tagging working point. We then define the online b-tagging efficiency with respect to the offline b-tagging as the ratio between N and D.

The upgrades that the ATLAS detector underwent and the software changes that were applied to the b-jet triggers translated in:

- Better management and lower consumption of the CPU resources that allowed ATLAS to deploy several b-jet chains during the different data-taking campaigns without impacting negatively the analyses by increasing the p_T and b-tagging thresholds too much.

- Increase of performances in terms of light- and c-jet rejection. This is shown in figures 3.8 and 3.9, which summarize the evolution of the b-jet trigger performances from 2015 to 2016 compared to the offline flavour tagging performances as of 2017.

- Improved robustness of the online b-tagging performances with respect to the pile-up, i.e. the mean number of interactions per crossing. This is shown in figure 3.10, where the online b-tagging efficiency with respect to the offline b-tagging is shown as a function of the pile-up for different online b-tagging working points.

- Improved correlation between online and offline flavour tagging, resulting in sharper turn-on curves of the online b-tagging efficiencies with respect to the offline

Other improvements are required for the Run-3 operations that will start in 2021. These improvements, some of which already under development, will be discussed in chapter 7.

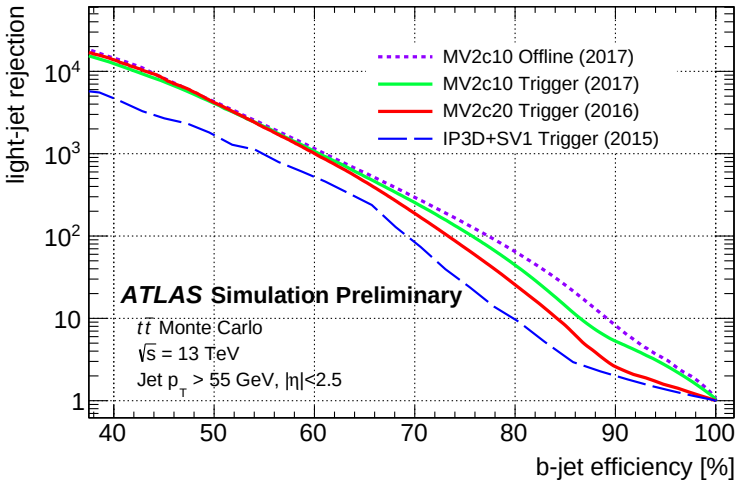

Figure 3.8: *Performance of b-tagging algorithms (measured using $t\bar{t}$ Monte Carlo events) in terms of light-jet rejection as a function of b-jet efficiency. Expected performance of b-tagging algorithm (MV2c10) for b-jet triggers in 2017 data-taking (green solid line) is compared to b-tagging algorithms used for b-jet triggers in 2016 (MV2c20) and 2015 (IP3D+SV1) data taking. Performance of b-tagging algorithm MV2c10 for offline jets is shown in purple dotted curve.*

3.4 b-Jet Trigger Emulation Tool

In addition to the above-mentioned improvements – some of which I contributed to develop and validate – a new tool for the emulation of b-jet triggers has been deployed for performing trigger studies and widely used in analyses during Run-2. I have taken care of the development and mantainment of this code.

The main purpose of such a software is to be able to compute the trigger decisions for any b-jet chain. This functionality is applicable to several use cases: when designing the new trigger strategy for the next iteration of an analysis; when a Monte Carlo simulation does not contain a trigger

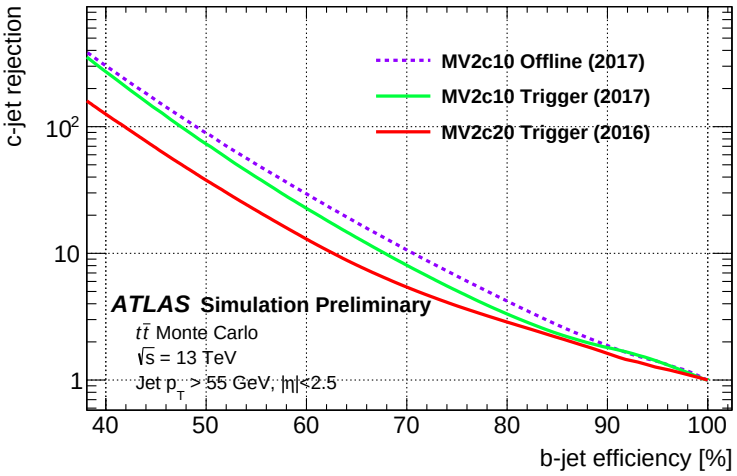

Figure 3.9: *Performance of b-tagging algorithms (measured using $t\bar{t}$ Monte Carlo events) in terms of c-jet rejection as a function of b-jet efficiency. Expected performance of b-tagging algorithm (MV2c10) for b-jet triggers in 2017 data-taking (green solid line) is compared to b-tagging algorithms used for b-jet triggers in 2016 (MV2c20). Performance of b-tagging algorithm MV2c10 for offline jets is shown in purple dotted curve.*

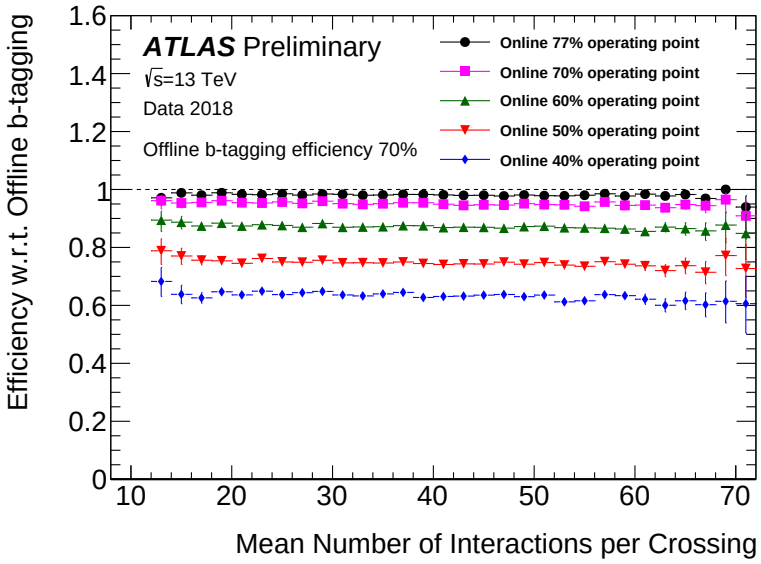

Figure 3.10: *The b-jet trigger efficiency with respect to the offline b-tagging algorithm (`MV2c10`) at the 70% efficiency operating point for various online efficiency operating points vs. the mean number of interactions per crossing. The relative b-jet trigger efficiency is measured in high purity di-lepton $t\bar{t}$ events collected in the 2018 data-set using dedicated single-lepton+jets triggers, which are unbiased with respect to the online b-tagging. Operating point efficiencies are defined using offline-reconstructed jets from an unbiased sample of Monte Carlo simulated $t\bar{t}$ events, where jets are labeled according to their hadron content. The online operating points were defined to have roughly the quoted efficiency using online-reconstructed jets matched to offline-reconstructed jets. Statistical uncertainties only are shown.*

required by an analysis (an extremely frequent case since Monte Carlo may be produced before the trigger menu is completed for data-taking); or for validating already-available triggers. In addition to this, the tool is provided with the capability of re-running the flavour tagging algorithms as they are used at online level, thus fully reproducing the b-jet trigger chain. Such a functionality can be easily used e.g. for evaluating the impact on performances resulting from the use of new flavour tagging algorithms.

The b-jet trigger emulation tool is now part of the official ATLAS software used at offline level and has been widely used for emulating triggers by physics analyses such as: VBF $H \to b\bar{b}$; $bH \to bb\bar{b}$; and $HH \to bb\bar{b}\bar{b}$. Moreover, it has been used for validating b-jet triggers, as well as L1Topo INVM and HT triggers, for 2017 and 2018 data-taking campaigns.

CHAPTER 4

Search for a VBF-produced Higgs boson in the bottom quark pair decay channel

In this and in the following two chapters we will describe two iterations of the same analysis: the first one performed analysing the data collected by the ATLAS collaboration during the 2012 data-taking campaign; the second one performed on the data collected during 2016 operations. The analysis focuses on the search for a Higgs boson produced via Vector Boson Fusion mechanism in the bottom quark pair decay channel: VBF $H \to b\bar{b}$. The two iterations are very similar on several levels: multivariate selection and statistical treatment in particular.

In this chapter in particular we will introduce the motivation for such a search and in the following chapters we will focus on the details of the analyses.

4.1 Motivation

In the periods when these analyses were conducted, the coupling of the Higgs boson with elementary particles had already been observed only for the bosonic decay modes: $H \to \gamma\gamma$, ZZ, W^+W^- [41]. Conversely little was still known as far as the fermions were concerned – with the exception of the τ leptons: the ATLAS and CMS collaborations had already announced the combined observation [89]. The Standard Model forsees numerous production mechanisms and decay modes of the Higgs boson, as shown in figure 1.3 and figure 1.5 respectively. The magnitude of the cross section and branching ratio depends on the mass of the Higgs boson; the latest precise measurement available quotes a value of 125.18 ± 0.16 GeV [39]. For such a mass value the decay to a pair of bottom quarks is the dominant one, with a branching ratio of $\sim 58\%$. The gluon-gluon fusion mechanism possesses the highest cross section, while the Vector Boson Fusion production mode is the second production mode in terms of magnitude.

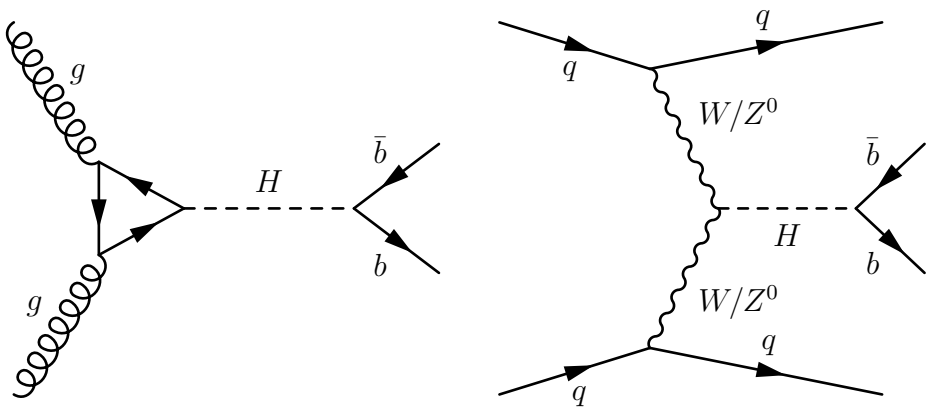

Figure 4.1: *Feynman diagrams of the resonant processes involved: the production of an Higgs boson via gluon-gluon Fusion (left); and the production of an Higgs or Z^0 boson via Vector Boson Fusion (right). The final states have two b-jets, resulting from the decay of the bosons.*

Channel	Branching Ratio [%]
$H \to b\bar{b}$	57.7
$H \to \tau\tau$	6.32
$H \to \mu\mu$	0.0219
$H \to c\bar{c}$	2.91
$H \to s\bar{s}$	0.0246

Table 4.1: *Values of the branching ratio for the different decay channels of the Higgs boson into pairs of fermions. Values taken from* `https://twiki.cern.ch/twiki/bin/view/LHCPhysics/CERNYellowReportPageBR2014`

However, a direct search of the $H \to b\bar{b}$ decay channel is not feasible at *LHC* if we focus on the gluon-gluon-fusion mechanism, due to the large amount of QCD background. This mainly consists in the direct bottom-quark pair production via the $g \to b\bar{b}$ channel and is indistinguishable from the gluon-gluon fusion production. Conversely, the VBF channel provides a specific event topology that can be exploited at trigger level by using b-jet triggers:

- the presence of four energetic jets: two originating from the light valence quarks of the colliding protons – labelled as VBF jets – which lie in the forward and backward regions of the detector; and two stemming from the bottom quarks – labelled as b-jets – which lie in the central region.

- Higgs bosons are colour singlets with no colour line to the bottom quarks; thus little QCD radiation and hadronic activity is expected between the two VBF jets, creating a huge rapidity gap between them.

The peculiar topology of the VBF production mode makes it feasible to perform a direct search in the $H \to b\bar{b}$ channel in the resolved regime.

The aim of these searches has been to investigate the Yukawa coupling with bottom quarks via direct search of the $H \to b\bar{b}$ decay, and to verify whether the bottom quarks actually acquire mass via the symmetry breaking mechanism as stated by the SM. The results of these analyses have been combined with other production channels and led to the observation of the $H \to b\bar{b}$ decay [45].

4.2 Data and simulated samples

The two analyses use $\sim$ 20 fb^{-1} and $\sim$ 36 fb^{-1} of data collected by the ATLAS experiment during 2012 and 2016 campaigns, respectively. After the quality requirements (good beam conditions, good detector performance and data quality) have been applied, the amount of data useful for the analyses corresponded to $\sim$ 20 fb^{-1} and $\sim$ 26 fb^{-1} for the two datasets. The missing luminosity in 2016 is due to a software bug affecting the trigger code used during data-taking, that obliged us to impose an additionl online transverse beamspot position requirement (i.e. to be within 2 mm of the nominal detector center), and resulted in several fb^{-1} to be marked as "not usable" for physics analysis.

The data sample receives contributions from different sources. These can be categorized in resonant and non-resonant. The former have, in the final state, a particle decaying to a $b\bar{b}$ pair:

- Higgs bosons decaying to $b\bar{b}$ pairs produced with the vector-boson fusion mechanism
- Higgs bosons decaying to $b\bar{b}$ pairs produced with the gluon-fusion mechanism
- Z bosons produced in association with jets, through different processes

The process $qq \to qqH \to qqb\bar{b}$ has a di-jet mass resonance (peak) at $m_{b\bar{b}} \sim$ 125 GeV. Similar reactions lie nearby: the gluon fusion-produced Higgs boson and the Z^0 boson – peaking at $m_{b\bar{b}} \sim$ 125 GeV and at $m_{b\bar{b}} \sim$ 90 GeV respectively. These three contributions cannot be fully isolated due to detector resolution effects. The non-resonant contribution includes QCD, $t\bar{t}$, single top,W+jets processes where QCD is the main component.

While a data-driven approach is used to estimate the amount and the shape of the non-resonant background – due to the lack of sufficient statistics of multi-jet MC – the resonant contributions have been modelled with MC samples, using the total cross-sections and the decay branching ratios supplied by the theory. The MC samples have been produced combining several simulation tools, so that we can obtain the most accurate theoretical predictions for these reactions. The simulation of particles, their momentum four-vectors as produced in collision, and the hadronization process have been simulated with *Powheg* [91, 92] and *Pythia8* [93]. The decay of the resonances into a $b\bar{b}$ pair have been reproduced with *MadGraph* [94].

The full ATLAS detector simulation is based on the *Geant4* [95] program corrected for all known detector effects. The high statistics production of the samples, after checking for any possible bias with respect to the fully simulated samples, has been made with Atlfast-II [90], which uses detailed parameterization of shower shapes of single particles instead of the full simulation of the calorimeter. The full list of the Monte Carlo samples used is shown in table 4.3.

DSID	Name Tag
2012 Analysis	
169723	PowhegPythia8_AU2CT10_VBFH125_bb e1788_a188_a224_r4348_p1328
169723	PowhegPythia8_AU2CT10_VBFH125_bb e1788_s1581_s1586_r4349_p1328
181707	PowhegPythia8_AU2CT10_ggH125NWA_bb_EF4jets e2512_a220_a205_r4540_p1328
181395	PowhegPythia8_AU2CT10_ggH125NWA_Inclusive e2091_a188_a224_r4348
181395	PowhegPythia8_AU2CT10_ggH125NWA_Inclusive e2091_s1581_s1586_r4349_r4348
206721	MadGraphPythia8_AU2CT10_Zbb_Np0 e3832_a188_a270_a271_r4348_p1328
206722	MadGraphPythia8_AU2CT10_Zbb_Np1 e3832_a188_a270_a271_r4348_p1328
206723	MadGraphPythia8_AU2CT10_Zbb_Np2 e3832_a188_a270_a271_r4348_p1328
206724	MadGraphPythia8_AU2CT10_Zbb_Np3 e3832_a188_a270_a271_r4348_p1328
206732	MadGraphPythia8_AU2CT10_Zbb_Np2_EW e4155_a188_a270_a271_r4348_p1328
206733	MadGraphPythia8_AU2CT10_Zbb_Np3_EW e4155_a188_a270_a271_r4348_p1328

Table 4.2: *The Monte Carlo samples used in the 2012 analyses, with their simulation and reconstruction tags. The DSID uniquely identifies all generator parameters, while the reconstruction tags define several simulation parameters such as: the lists of sequential bug fixes to the generator; the version of the detector geometry description that was used; the sequential revisions to the digitization of particle hits and to the reconstruction algorithms.*

DSID	Name Tag
2016 Analysis	
341565	PowhegPythia8EvtGen_CT10_AZNLOCTEQ6L1_ggH125_bb_EF4jets e3988_a766_a821_r7676_p2666
341566	PowhegPythia8EvtGen_CT10_AZNLOCTEQ6L1_VBFH125_bb e3988_a766_a821_r7676_p2666
342195	MadGraphPythia8EvtGen_A14NNPDF23_QCDZbbjj_Incl e4191_a766_a821_r7676_p2719
342196	MadGraphPythia8EvtGen_A14NNPDF23_EWKZbbjj_Incl e4191_a766_a821_r7676_p2719

Table 4.3: *The Monte Carlo samples used in the 2016 analyses, with their simulation and reconstruction tags. The DSID uniquely identifies all generator parameters, while the reconstruction tags define several simulation parameters such as: the lists of sequential bug fixes to the generator; the version of the detector geometry description that was used; the sequential revisions to the digitization of particle hits and to the reconstruction algorithms.*

CHAPTER 5

Analysis of data collected during 2012 operations

The data collected during 2012 have been analysed following two approaches: using a cut-based approach and a strategy relying on the use of Multivariate Analysis techniques. The latter constitutes the main analysis – which we will discuss in the following – since it reaches higher sensitivity than the cut-based approach, which is used as a cross-check analysis. The University of Genova group has taken care of the main analysis, while the cut-based approach has been handled by the University of Chicago ATLAS group.

5.1 Trigger Strategy

Events are selected by using b-jet triggers, summarized in table 5.1. The p_T thresholds of these triggers are 15 GeV at the first trigger level (*L1*) and 35 GeV at the last trigger stage (*EF*).

Channel	Trigger
2b-jets	EF_2b35_loose_4j35_a4tchad
1b-jet + vbf	EF_b35_medium_j35_a4tchad_vbf_3L1J15_FJ15
	EF_b35_medium_j35_a4tchad_vbf_2L1FJ15

Table 5.1: *The Triggers used during 2012 data-taking period. The general 2 b-jets trigger was available for the full 2012 period (20.2 fb^{-1}); the vbf-dedicated triggers were available for only $\sim$ 20% of the 2012 campaign ($\sim$ 4.4 fb^{-1}).*

The *ATLAS* collaboration did not dispose a vbf-dedicated triggers for the major part of the 2012 data-taking. The primary trigger – available for the full 2012 operations – simply requires 4 central jets, two of them passing the "medium" b-jet trigger selection. In addition to this, two vbf-dedicated triggers become available for a limited part of data-taking ($\sim$ 20% of the operations): they require the presence of one b-jet plus one or two forward

jets, with VBF-dedicated topology requirements. The trigger channels are labelled respectively as "2 b-jets" and "1 b-jet + vbf".

5.2 Event Selection

We select events containing exactly four jets with $p_T > 50$ GeV and $|\eta| < 4.5$. Sorted according to their pseudo-rapidity η, they are labelled based on their position in the ATLAS detector: "VBF-jets" for the two less central jets; and "b-jets" for the two more central jets, with the additional requirement of being matched to the online b-jets. In addition, the latter jets are required to be within the tracker acceptance ($|\eta| < 2.5$) and are then b-tagged offline. The offline b-tagging is obtained with a cut on the MV1 weight variable $w > 0.8119$ corresponding to a working point of 70% b-tagging efficiency.

An additional cut on the transverse momentum of the b-jets pair is required in order to both improve the signal over background ratio and the smoothness of the $m_{b\bar{b}}$ mass distribution. Figure 5.1 shows the $m_{b\bar{b}}$ spectrum of the selected events. The kinematic scupting at high $m_{b\bar{b}}$ values is a result of the p_T cut on each b-jet at 50 GeV: jets with large relative ΔR, and hence large $m_{b\bar{b}}$ mass, are selected. A cut of $p_T(b\bar{b}) > 100$ GeV was enough to remove this high $m_{b\bar{b}}$ peak.

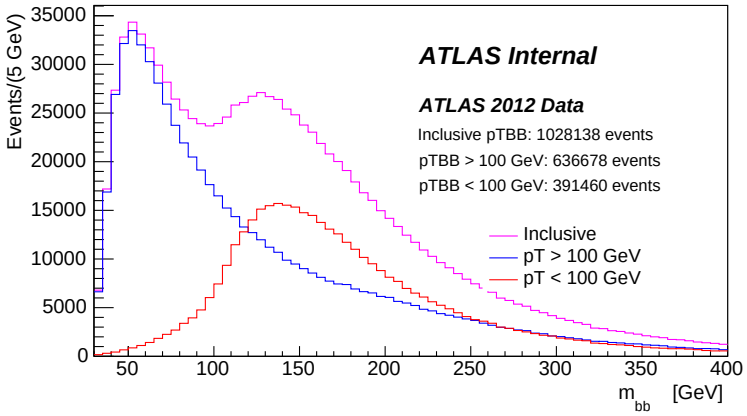

Figure 5.1: *The $m_{b\bar{b}}$ spectrum of the selected events and the effect of the cut on the transverse momentum of the b-jets pair, $p_T(b\bar{b})$*

Tables 5.2 and 5.3 summarize the cut-flows for the Higgs boson Monte Carlo samples (VBF- and ggF-produced), tables 5.4 and 5.5 show the cut-flows for the $Z \to b\bar{b}$ samples (QCD- and EW-produced), and table 5.6 illustrates the cut-flow for the data.

5.3 Multivariate Analysis

The cut-based event selection provided a first data screening, but has too large a background contribution – if compared with signal events – and re-

Cut	**N_{sig}**	**Cut efficiency**	**Total efficiency**
generated	18535	-	-
$n_{tracks}^{PV} > 3$	18528	1.00	0.999
LAr noise removal	18528	1.00	0.999
trigger	1031	0.06	0.056
4 jets with $p_T > 50\ GeV$	393	0.38	0.021
truth-matching	343	0.87	0.018
η-sorting	267	0.78	0.014
online RoIs b-jets matching	215	0.81	0.012
centrality of b-jets	214	0.99	0.012
offline b-tagging of b-jets	174	0.81	0.009
$p_T(b\bar{b}) > 100\ GeV$	129	0.74	0.007

Table 5.2: *Cutflow of the analysis on the signal VBF MC simulation sample. The statistical errors are always smaller then the last quoted digit. The signal yields are normalized to those expected on the full used luminosity.*

Cut	**N_{sig}**	**Cut efficiency**	**Total efficiency**
generated	45322	-	-
$n_{tracks}^{PV} > 3$	45315	1.00	0.9998
LAr noise removal	45315	1.00	0.9998
trigger	2037	0.04	0.0449
4 jets with $p_T > 50\ GeV$	697	0.34	0.0154
truth-matching	578	0.83	0.0127
η-sorting	183	0.32	0.0040
online RoIs b-jets matching	145	0.79	0.0032
centrality of b-jets	145	1.00	0.0032
offline b-tagging of b-jets	120	0.83	0.0027
$p_T(b\bar{b}) > 100\ GeV$	95	0.79	0.0021

Table 5.3: *Cutflow of the analysis on gluon fusion MC sample. The statistical errors are always smaller then the last quoted digit. The signal yields are normalized to those expected on the full used luminosity and the filter efficiency.*

Cut	**N_{sig}**	**Cut efficiency**	**Total efficiency**
generated	88003186	-	-
$n_{tracks}^{PV} > 3$	87999994	0.99996	0.99996
LAr noise removal	87999994	1.00000	0.99996
trigger	125474	0.00143	0.00143
4 jets with $p_T > 50\ GeV$	40046	0.31916	0.00046
truth-matching	28772	0.71847	0.00033
η-sorting	7145	0.24834	0.00008
online RoIs b-jets matching	5428	0.75972	0.00006
centrality of b-jets	5408	0.99632	0.00006
offline b-tagging of b-jets	4481	0.82843	0.00005
$p_T(b\bar{b}) > 100\ GeV$	3748	0.83661	0.00004

Table 5.4: *Cutflow of the analysis on strongly-produced Z + jets MC samples. The statistical errors are always smaller then the last quoted digit. The signal yields are normalized to those expected on the full used luminosity and summed over the different jet multiplicity categories.*

Cut	**N_{sig}**	**Cut efficiency**	**Total efficiency**
generated	46593	-	-
$n_{tracks}^{PV} > 3$	46470	0.997	0.997
LAr noise removal	46470	1.000	0.997
trigger	2775	0.060	0.060
4 jets with $p_T > 50\ GeV$	1134	0.409	0.024
truth-matching	804	0.709	0.017
η-sorting	285	0.354	0.006
online RoIs b-jets matching	221	0.774	0.005
centrality of b-jets	220	0.998	0.005
offline b-tagging of b-jets	182	0.826	0.004
$p_T(b\bar{b}) > 100\ GeV$	160	0.881	0.003

Table 5.5: *Cutflow of the analysis on EW-produced Z + jets MC samples. The statistical errors are always smaller then the last quoted digit. The signal yields are normalized to those expected on the full used luminosity and summed over the different jet multiplicity categories.*

Cut	N_{bkg}	Cut efficiency	Total efficiency
trigger and at least 4 jets	119881920	-	-
good runs list	114367080	0.95	0.954
$n_{tracks}^{PV} > 3$	114354170	1.00	0.954
LAr noise removal	114093210	1.00	0.952
trigger	46949274	0.41	0.392
4 jets with $p_T > 50\ GeV$	11877433	0.25	0.099
online RoIs b-jets matching	2857351	0.24	0.024
centrality of b-jets	2816464	0.99	0.023
offline b-tagging of b-jets	1417385	0.50	0.012
$p_T(b\bar{b}) > 100\ GeV$	874539	0.62	0.007

Table 5.6: *Cutflow of the analysis on data.*

quired a more restrictive selection. A further enhancement of the analysis sensitivity has been achieved by the use of MVA tecniques: some input variables related to the typical topology of VBF-produced events are combined to produce a discriminating variable for distinguishing the background candidates from the signal candidates. We optimized the MVA in order to maximize the VBF significance. We tested several MVA tools, implemented in the ROOT-integrated [96] TMVA package (*Toolkit for Multivariate and Data Analysis*) [97]: Boosted Decision Tree (BDT); Neural Networks; likelihoodPCA; and H-matrix discriminant – the best method being the one with the most discriminating ROC curve, i.e. the Boosted Decision Tree.

For the training and testing phases of the MVA algorithm we used the data in the mass sidebands (defined as $70 < m_{b\bar{b}} < 90$ GeV and $150 < m_{b\bar{b}} < 190$ GeV) for describing the background and the available Monte Carlo samples for describing the $H \to b\bar{b}$ signal. The samples are divided in two: one half being used for the training, the other half for the testing of the MVA. The use of the sidebands is justified since the input variables have similar shapes in the two side bands. The remaining differences between the two regions might lead to a non-optimal tuning of the discriminant variable but does not produce any bias on the signal strength since the background normalization is determined during the fit procedure.

The analysis strategy relies on a background-plus-signal fit of the $m_{b\bar{b}}$ spectrum; thus we took into account only variables with a negligible correlation with $m_{b\bar{b}}$:

- $\boldsymbol{m_{JJ}}$: the invariant mass of the VBF-jet pair.
- $\boldsymbol{\Delta\eta_{JJ}}$: the pseudorapidity separation between the two VBF-jets.
- $\boldsymbol{\eta_J^*}$: the pseudarapidity separation between the VBF-jet pair and the Higgs candidate ($\eta_J^* = \frac{1}{2}(\eta_{J_1} + \eta_{J_2}) - \frac{1}{2}(\eta_{b1} + \eta_{b2})$)
- $\boldsymbol{H_T}$: the scalar sum of the transverse momenta of additional jets (with $p_T > 20$ GeV, calibrated, passing the LAr removal and the electron

overlap removal as the four main jets in the event) in the central region of the detector, i.e. $|\eta| < 2.5$.

- **cos $\boldsymbol{\theta}$**: the cosine of the polar angle of the vector $\vec{p}_{J_1} \times \vec{p}_{J_2}$ in the Higgs boson rest frame.
- **max($|\boldsymbol{\eta_J}|$)**: The maximum pseudorapidity value of one of the light jets.
- The calorimeter widths of the jets originated by the light quarks. These variables aim to separate jets issued from quark hadronization from those produced from gluon hadronization. They constitute our quark/gluon discriminant.

Figure D.2 illustrates the input variables to the MVA and figure 5.3 shows the MVA output. The events have been categorized according to the BDT score in mutually exclusive regions. The choice of the BDT slices was tuned for obtaining the configuration that optimizes the VBF signal significance, defined as

$$\Sigma_{stat}(\mu) \equiv \left[\sum_{i=1}^{4} \left(\frac{S_i}{\sqrt{S_i + B_i}} \right)^2 \right]^{-\frac{1}{2}} \tag{5.1}$$

where i labels the BDT region, S and B represent the VBF signal and expected background events in the range $100 < m_{b\bar{b}} < 140$ GeV. The resulting BDT regions are the following:

- **Category 0** covers the range $-1.00 < BDT < -0.08$
- **Category I** covers the range $-0.08 < BDT < +0.01$
- **Category II** covers the range $+0.01 < BDT < +0.06$
- **Category III** covers the range $+0.06 < BDT < +0.09$
- **Category IV** covers the range $+0.09 < BDT < +1.00$

Category 0 possesses the lowest VBF significance. As a consequence, the data it contains will not be used in the signal search. The remaining regions have been used for the signal extraction.

5.4 Fit Strategy

The signal extraction consists in a simultaneous profile likelihood fit in the four BDT regions defined in section 5.3. The fit covers the range $70 < m_{b\bar{b}} < 300$ GeV. The shape of resonant contributions ($H \to b\bar{b}$ and $Z \to b\bar{b}$) are described using the expected distribution from Monte Carlo simulation, while the shape of the combinatorial background will be determined on real data. The yields of all the fit components have been determined on data,

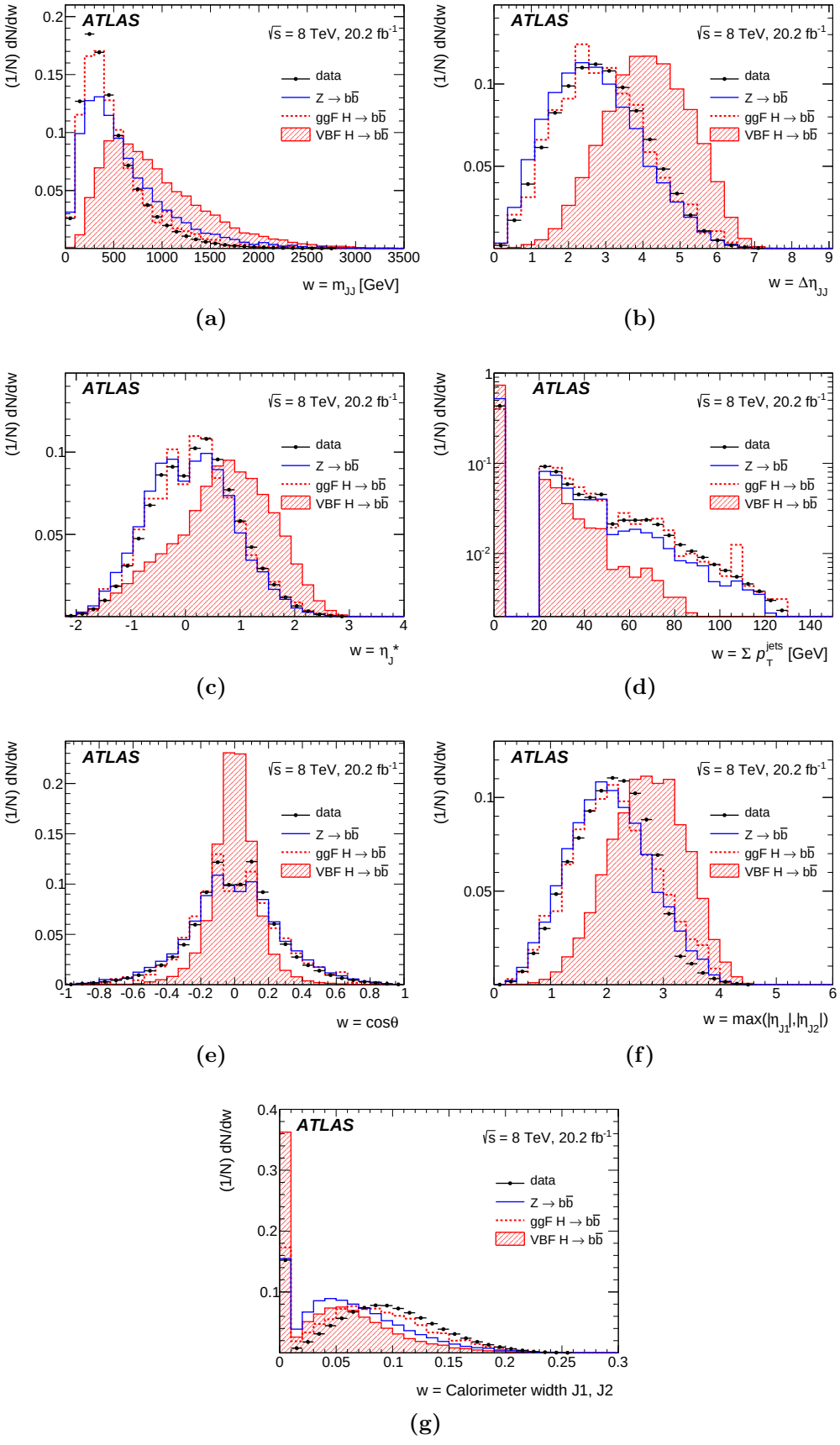

Figure 5.2: *Distributions of the input variables for the multivariate analysis.*

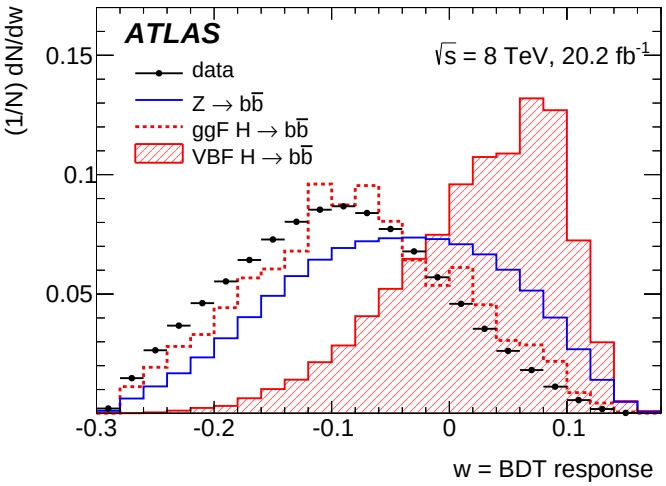

Figure 5.3: *Distribution of the BDT response, on data and signal MC.*

with the exception of the $Z \to b\bar{b}$ contribution which is contrained to the SM expectation using independent constraints in each BDT region in addition to a common constraint, representing the uncorrelated and correlated terms of the systematic uncertainty.

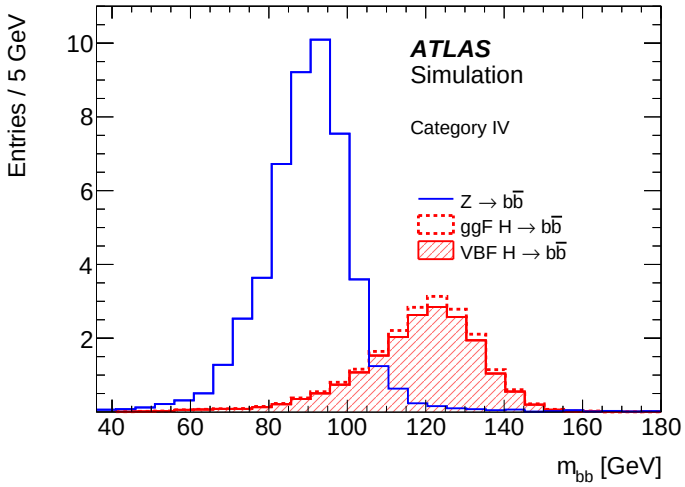

Figure 5.4: *The shape of the invariant mass of the b-jets produced in Z decays and in Higgs decays ($m_{b\bar{b}}$) produced in gluon fusion and vector boson fusion production.*

Figure 5.4 shows the $m_{b\bar{b}}$ shape for VBF and gluon fusion processes. The two distributions are essentially identical indicating that no separation between the two processes is possible from the $m_{b\bar{b}}$ fit. In the rest of the analysis any residual contribution of gluon fusion production to the Higgs yield will be treated as signal.

The background shape is described with an analytic function. We considered several functions for the background description and we found only a few could describe it:

- The linear combination of exponentials

$$f(x) = a_0 e^{-\frac{x}{a_1}} - e^{-\frac{x}{a_2}} \tag{5.2}$$

  where we indicated as a_0, a_1 and a_2 some real positive variables and as x the observable, i.e. $m_{b\bar{b}}$.

- Bernstein polynomials of different order n. Given $x \in [a, b]$ these are defined as

$$B_n(x) = \sum_{\nu=0}^{n} \beta_\nu \binom{n}{\nu} \frac{(x-a)^\nu (b-x)^{n-\nu}}{(b-a)^n} \tag{5.3}$$

  with β_ν the Bernstein coefficients.

- Combination of the above functions

We selected for each BDT region a different background model and provided both a candidate and an alternative background model. Their choice is based on few considerations: the probability associated to the χ^2 values; the number of floating parameters; and bias studies. The latter consists in assessing the biases introduced, during the fitting procedure, when parametrizing the background with different pdfs. Such a study has been performed by generating several TOY Monte Carlo simulations with a background description and fitting it with an alternative function. We retained only the functions with a $\mathcal{P}(\chi^2, dof) > 0.05$, with a bias on the Higgs signal strength μ smaller than its statistical error and as few free-parameters as possible. Table 5.7 summarizes the nomial and the alternative functions used for describing the background in the different BDT regions.

	Category I	Category II	Category III	Category IV
Nominal	$O(4)$ Bernstein	$O(3)$ Bernstein		
Alternative	$O(2)$ Bernstein $\times$ Expo	3 Expo	2 Expo	Expo

Table 5.7: *Reference and alternative combinatorial background parametrizations in each BDT category.*

The statistical analysis of the data makes use of a binned likelihood function $\mathcal{L}(\mu, \theta)$ constructed as the product of Poisson probability terms over the bins of the $m_{b\bar{b}}$ distribution, which is used as the variable for the signal extraction, in the four BDT output categories. The Higgs signal (Z background) strength parameter, μ (μ_Z), multiplies the expected SM Higgs (Z) boson production cross section in each bin. Systematic uncertainties are introduced as nuisance parameters (NPs) and they are parametrized by Gaussian constraints. The NPs are here indicated with θ: some of them only affect the H and Z fit models, others only the other background models. The expected number of Higgs and background events in each bin is therefore a

function of θ. The resulting binned likelihood function $\mathcal{L}(\mu, \theta)$ used in the statistical analysis is the following:

$$\mathcal{L}(\mu,\theta) = Pois(n|\mu H(\theta) + \mu_Z Z(\theta) + B(\theta)) \left[\frac{\mu n^H_{b,c}(\theta) + \mu_Z n^Z_{b,c}(\theta) + n^B_{b,c}(\theta)}{\mu H(\theta) + \mu_Z Z(\theta) + B(\theta)} \right] \tag{5.4}$$

5.5 Systematic Uncertainties

The sources of systematic uncertainty can be categorized in different components: experimental uncertainties; uncertainties on the modelling of the non-resonant background; and theoretical uncertainties on the Higgs and Z processes. The uncertainties can affect both the normalisation and the kinematic distributions. Table 6.2 summarized the magnitude of the systematic contribution on both the main analysis and the cut-based analysis.

Source of uncertainty		Uncertainty on μ	
		MVA	Cut-Based
Experimental Uncertaities	Detector-related	$+0.2/-0.3$	$+1.6/-1.2$
	MC statistics	± 0.4	± 0.1
Theoretical Uncertaities	MC signal modelling	± 0.1	± 1.3
	Z yield	$+0.5/-0.5$	± 1.4
Non-resonant background modelling	Choice of function	± 1.0	± 1.0
	Sidebands statistics	± 1.7	± 3.7
Statistical Uncertainties		± 1.3	
Total		± 2.3	$+4.6/-4.4$

Table 5.8: *Systematic uncertainties and their contribution in both the MVA and the Cut-Based Analysis*

5.5.1 Experimental uncertainties

The dominant experimental uncertainties on the Higgs signal yield arise from the statistical uncertainty due to the finite size of the MC samples, the jet energy scale uncertainty (JES), and the b-jet triggering and tagging. Several sources contribute to the uncertainty on the jet energy scale [98]: in situ jet calibration; pile-up-dependent corrections; and the flavour composition of jets in different event classes. The jet energy scale uncertainty affects both the $m_{b\bar{b}}$ shape for the Higgs signal and the Z background and the value of the BDT output, causing migration of events between BDT categories. The b-jet trigger and tagging efficiencies are another source of systematic uncertainty, contributing 10% to the total uncertainty. They are calibrated using multijet events containing a muon and $t\bar{t}$ events, respectively [99]. The uncertainty on the jet energy resolution contributes about 4%. The uncertainty on the integrated luminosity is 1.9% [100].

5.5.2 Modelling uncertainties on the $m_{b\bar{b}}$ shape of the non-resonant background

The uncertainties on the shape of the $m_{b\bar{b}}$ distribution for the non-resonant background is the largest source of systematic uncertainty. The dominant contributions to this source come from the limited number of events in the $m_{b\bar{b}}$ sidebands of the data used for the fit to the nominal function and from the choice of the function.

The background uncertainty has been assessed following the method used by the *ATLAS* di-jet resonance search [101]. It is performed by means of TOY MC simulations. Its contribution consists of two independent components: the statistical uncertainties on the background function fit parameters ($F1$); and the systematics stemming from the arbitrary choice of the fit functions ($F2$).

For each BDT region the procedure adopted is the following:

- we fit real data on the side bands with the nominal background description and create with the resulting function a reference histogram $F(\text{ref})$;
- we generate N TOY MC simulations using real data: in each bin the number of simulated event is extracted from a Gaussian distribution centred on the number of event in real data with a standard deviation corresponding to the uncertainty in that bin. Each toy has been fitted on the side bands with both the background models, together with the floating Z component. For each simulation k we create the histograms of the resulting nominal and alternative background function: $F(k)$ and $G(k)$ respectively;
- for each toy we compute two histograms: one is given by the difference between the nominal function obtained and the reference one $dF(k) \equiv F(k) - F(\text{ref})$; the other one is given by the difference between the two background models $dG(k) \equiv G(k) - F(k)$;
- with these histograms we build the error matrices for the two independent contributions of the background uncertainty:

$$F1_{i,j} \equiv \frac{1}{N}\sum_{k=1}^{N} dF_i(k)dF_j(k) \tag{5.5}$$

$$F2_{i,j} \equiv \frac{1}{N}\sum_{k=1}^{N} dG_i(k)dG_j(k) \tag{5.6}$$

where indices i, j identify the bin numbers while k identifies the toy number;

- we decompose these matrices in their independent contributions ΔF_i, retaining the most relevant ones (the weight being given by their eigenvalues): each contribution will be introduced as an additional nuisance parameter in the profile likelihood fit. More details about the eigenvectors decomposition are given in Appendix B.

A re-parametrization F of the reference fitting function can be done as the original function plus a linear combination of the most relevant contributions to the error matrices ΔF_i:

$$F = F(\text{ref}) + \sum_i \alpha_i \Delta F_i. \tag{5.7}$$

The resulting function allows for a linearization of the uncertainties, which leads to a more stable fitting procedure, and is an approximation of the nominal function with floating parameters.

This procedure aims to avoid a double counting of the statistical power of our data, because the data are used to determine the starting point of the fit ($F(\text{ref})$), and the changes in the shape (ΔF_i), but are not used to constrain the fit itself.

In order to minimize possible biases coming from the presence of a signal, this linearization procedure is done using only the side bands, and then is used to fit the complete $m_{b\bar{b}}$ range.

5.5.3 Theoretical uncertainties

The uncertainties on the MC modelling of the Higgs signal events contribute about 10% to the total uncertainty on the Higgs yield. The sources for these uncertainties are higher order QCD corrections, the modelling of the underlying event and the parton shower, the PDFs, and the $H \to b\bar{b}$ branching ratio. An uncertainty on higher order QCD corrections for the cross-sections and acceptances is estimated by varying the factorisation and renormalisation scales, μ_F and μ_R, independently by a factor of two around the nominal values [102] with the constraint $0.5 \leq \mu_F/\mu_R \leq 2$. The uncertainty due to higher order corrections to the p_T spectrum of the Higgs boson is estimated by comparing the results between LO and NLO calculations for VBF production and by varying the factorisation and renormalisation scales for ggF production. Uncertainties related to the simulation of the underlying event and the parton shower are estimated by comparing distributions obtained using Powheg+Pythia8 and Powheg+Herwig [103]. The uncertainties on the acceptance due to uncertainties in the PDFs are estimated by studying the change in the acceptance when different PDF sets such as MSTW2008NLO [104] and NNPDF2.3 [105] are used or the CT10 PDF set parameters are varied within their uncertainties. The largest variation in acceptance is taken as a systematic uncertainty. The uncertainty on the $H \to b\bar{b}$ branching ratio is also accounted for. The uncertainty on higher order QCD corrections to the $Z \to b\bar{b}$ yield is estimated by varying the factorisation and renormalisation scales around the nominal value in the

manner described above. It is found to be about 40-50%, depending on the BDT category, out of which about 25% is correlated. These correlated and uncorrelated uncertainties are used to constrain the Z yield in the fit. This process results in about 20-25% to the total uncertainty on the Higgs yield.

5.6 Results

A statistical fitting procedure based on the RooStats framework [106, 107] is used to estimate the Higgs signal strength, μ, from the data. The test statistic q_μ is constructed according to the profile-likelihood ratio:

$$q_\mu = 2ln(\mathcal{L}(\mu, \theta_\mu)/\mathcal{L}(\hat{\mu}, \theta_\mu)) \tag{5.8}$$

where $\hat{\mu}$ and θ are the parameters that maximise the likelihood, and θ_μ are the nuisance parameter values that maximise the likelihood for a given μ. This test statistic is used both to measure the compatibility of the background-only model with the data, and to determine exclusion intervals using the CLs method [108, 109].

The ratios of Z yields to the SM predictions (μ_Z) are found to be compatible in all of the four BDT regions. Combined over the four categories, the fit further constrains μ_Z to 0.7 ± 0.2. The correlation between μ_Z and μ_H has been found to be 0.22, as described in Appendix C.

The combined Higgs signal strength is

$$\mu_H = \frac{\sigma_{measured}}{\sigma_{SM}} = -0.8 \pm 2.3 \tag{5.9}$$

where the uncertainty includes both the statistical (± 1.3) and systematic ($+1.8/-1.9$) components. In the absence of a signal, the limit on the Higgs signal strength at 95% confidence level (CL) is expected to be 5.4. When Standard Model production is assumed, the expected limit is found to be 5.7. The observed limit is 4.4.

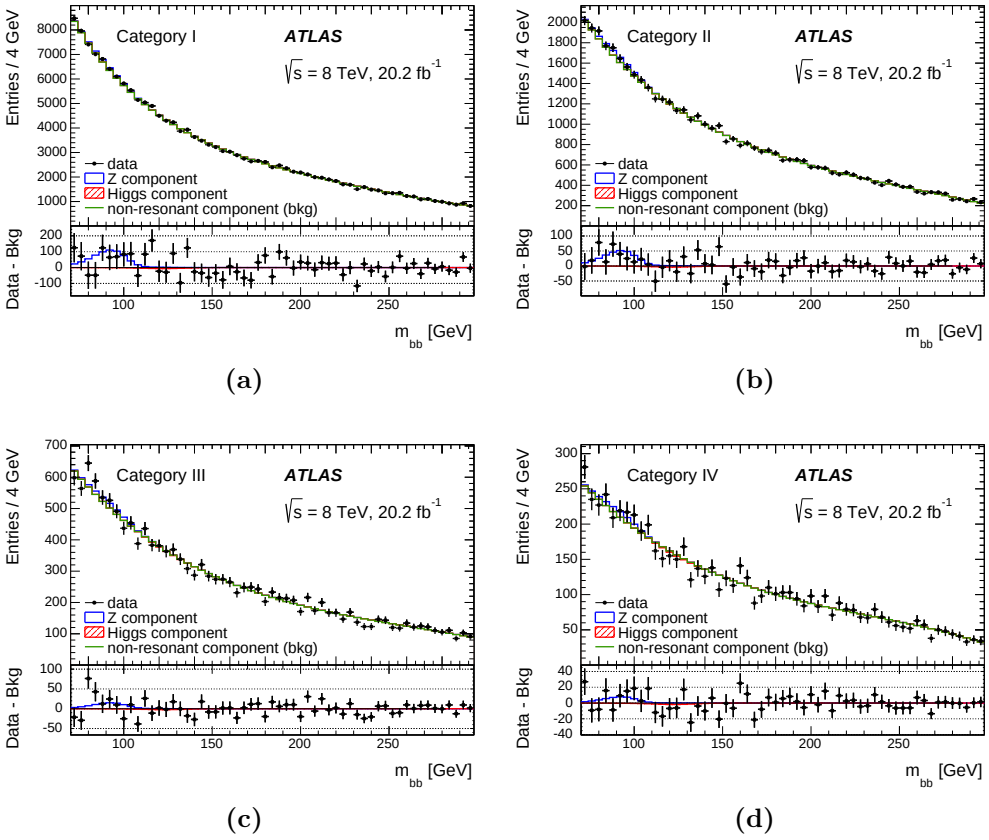

Figure 5.5: *Results of the profile likelihood fit to the $m_{b\bar{b}}$ distributions in the four BDT categories. The points represent the data, and the histograms represent the non-resonant background and the Z (blue line) and Higgs contributions (red line). In the lower panels, the data after subtraction of the non-resonant background are compared with the fit to the Z and Higgs contributions.*

CHAPTER 6

Analysis of data collected during 2016 operations

The data collected during 2016 have been analysed using a multivariate approach. The analysis has been the result of a collaboration with the SLAC national accelerator laboratory ATLAS group. Moreover, the results of the analysis have been combined together with a complementary channel that requires the presence of a high-momentum photon in the central region of the detector [110], which resulted in the publication of a combined paper [111].

The search in the $pp \to H\gamma jj \to b\bar{b}\gamma jj$ signature benefits from a large reduction of the QCD background with respect to the inclusive $b\bar{b}jj$ channel [112, 113]. Since gluons do not radiate photons, the gluon-induced component of the multi-jet background is suppressed. Moreover, destructive interference between diagrams with hard central photons emitted from the initial-state quark and the final-state quark further suppresses central photon emission in the background processes. The additional requirement of a photon – iradiated from an internal vector boson or from the incoming/outgoing quarks – in the final state provides a clean trigger signature.

In the following we will focus the discussion mainly to the "fully-hadronic" analysis, mentioning from time to time the $H\gamma jj \to b\bar{b}\gamma jj$ analysis. The results will refer to their combination.

6.1 Trigger Strategy

Events are selected by using b-jet triggers, summarized in table 6.1. In the 2016 analysis we focused on a different trigger approach with respect to the previous iteration of the analysis, aimed at increasing the trigger efficiency. The triggers are categorized in two topologies: a *four-central* channel – that requires four jets in the central part of the detector, two of which b-tagged; and a *two-central* channel – that requires two jets in the central part of the detector and at least one in the forward region of the detector. The p_T thresholds of these triggers are 15 GeV at the first trigger level ($L1$), while

at the last trigger stage (*HLT*) it varies according to the trigger topology.

Channel	Trigger
four-central	HLT_2j45_bmv2c2070_split_2j45
	HLT_2j35_bmv2c2060_split_2j35
two-central	HLT_j80_bmv2c2070_split_j60_bmv2c2085_split_j45_320eta490

Table 6.1: *The triggers used during the 2016 data-taking period. The two four-central triggers have been used in two different data-taking period.*

The *four-central* channel possesses two trigger chains with different p_T and b-tagging thresholds. These triggers were used in different periods: the change in the HLT thresholds was due to CPU constrains during data-taking. At first, at least four jets with $p_T > 45$ GeV, two of which also satisfying the 70% MV2c20 b-tagging working point, were required. Then, these requirements were changed by requiring the presence of at least four jets with $p_T > 35$ GeV, two of which also satisfying the 60% MV2c20 b-tagging working point.

The *two-central* channel requires two jets with $|\eta| < 3.2$: one with $p_T > 60$ GeV and satisfying the 85% MV2c20 b-tagging working point; another with $p_T > 80$ GeV and satisfying the 70% MV2c20 b-tagging working point. Moreover, a jet in the forward region of the detector ($3.2 < |\eta| < 4.9$) and with a minimum p_T of 45 GeV is required.

The Monte Carlo samples available for the 2016 analysis didn't posses all the required triggers. The missing triggers were emulated with the Trigger Emulation Tool described in section 3.4.

6.2 Event Selection

The definition of two trigger categories translated, also during event selection, in targeting two different – and exclusive – event topologies according to the position of the jets in the detector. The naming convention being the same, these two categories are labelled as *four-central* channel and *two-central* channel.

Concerning the *four-central channel*, we require at least four offline jets – two of which are b-tagged – in the central region of the detector ($|\eta| < 2.8$): two jets with $|\eta| < 2.5$ that must satisfy a $p_T > 55$ GeV threshold and pass the offline 70% b-tagging requirements; and two additional jets with $p_T > 55$ GeV. In order to avoid overlap with the *two-central channel*, events with a jet with $p_T > 60$ GeV and $3.2 < |\eta| < 4.4$ have been vetoed.

Concerning the *two-central channel*, we require at least one VBF jet in the forward region ($|\eta| > 3.1$) in addition to the two b-tagged jets in the central part of the detector: at least one jet with $p_T > 95$ GeV; and at least one additional jet with $p_T > 70$ GeV. The forward jet must satisfy the $p_T > 60$ GeV requirement. Lastly, the event must have at least one more jet with $p_T > 20$ GeV and $|\eta| < 4.4$.

Similarly to what was observed during the previous analysis – and shown in figure 5.1 – there is a kinematic sculpting of the $m_{b\bar{b}}$ distribution in the low $m_{b\bar{b}}$ region coming from the p_T requirement on the jets. This sculpting has been reduced by applying an additional cut on the p_T of the $b\bar{b}$ system: $p_{T_{b\bar{b}}} > 150$ GeV and $p_{T_{b\bar{b}}} > 160$ GeV for the *four-central* channel and *two-central* channel respectively.

6.3 Multivariate Analysis

The chosen multivariate algorithm is a BDT, trained with the *scikit-learn* package [114]. For the training and testing phases of the MVA algorithm we have used the data in the $m_{b\bar{b}}$ sidebands (defined as $80 < m_{b\bar{b}} < 100$ GeV and $150 < m_{b\bar{b}} < 190$ GeV) for describing the background and the available Monte Carlo samples for describing the $H \to b\bar{b}$ signal. The samples are divided in two, one half being used for the training, the other half for the testing of the MVA algorithm. Here as well, the small differences in the background distributions in the sidebands only results in a sub-optimal discrimination power of the BDT. This does not introduce any bias during the signal extraction since the background normalization and shape are determined during the fit.

Since we aimed for a combined result with the $H\gamma jj \to b\bar{b}\gamma jj$ analysis, the two searches have been harmonized as much as possible. Thus, some the input variables for the BDT are in common between the two studies. Appendix D shows the distributions of these variables for the photon analysis. The selected input variables for the BDT have a minimal collelation with $m_{b\bar{b}}$:

- m_{jj}: the invariant mass of the VBF jet pair
- p_T^{jj}: the transverse momentum of the VBF jet pair
- N_{trk}^{j1}, N_{trk}^{j2}: the number of tracks with $p_T > 0.5$ GeV in the VBF jets, $j1$ and $j2$. This variable discriminates between gluon jets, which are more abundant in the background processes, and light-quark jets, which are present in the signal. The variable is only used for jets with $|\eta| > 2.5$
- $p_T^{balance}$: the ratio of the vectorial and scalar sums of the jet trasverse momenta. This variable discriminates between electroweak signal processes, which tipically are balanced, and multijet QCD events, which are less ballanced
- $cos(\theta)$: cosine of the angle between the normal directions of the planes spanned by the VBF jet pair and signal b-jet pair in the center of mass frame of the $b\bar{b}jj$ system, which is related to the angular dynamics of the production mechanism

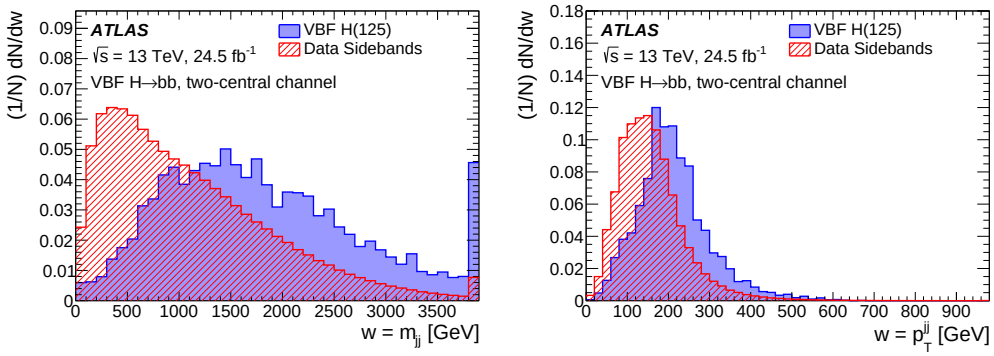

(a)

(b)

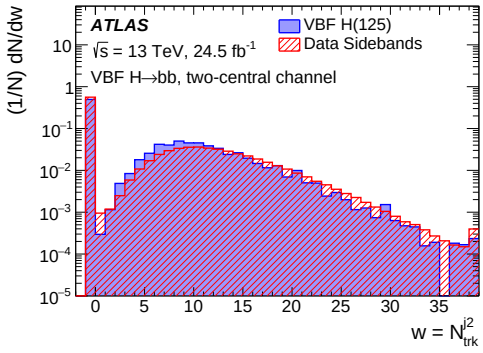

(c)

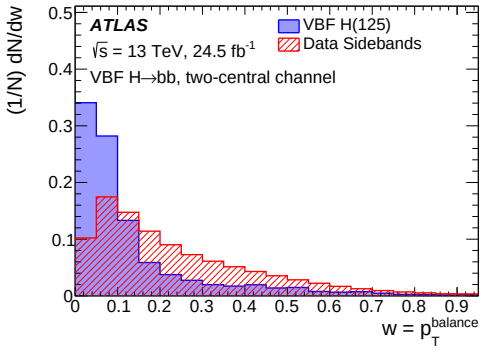

(d)

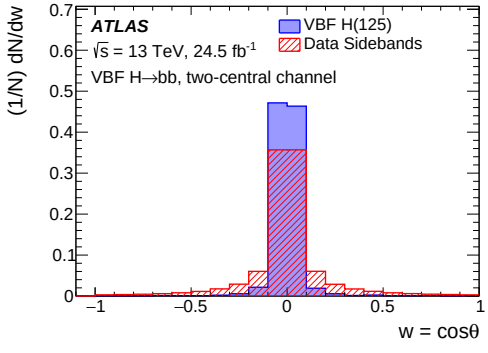

(e)

Figure 6.1: *Distributions (two-central channel) of the input variables for the multivariate analysis.*

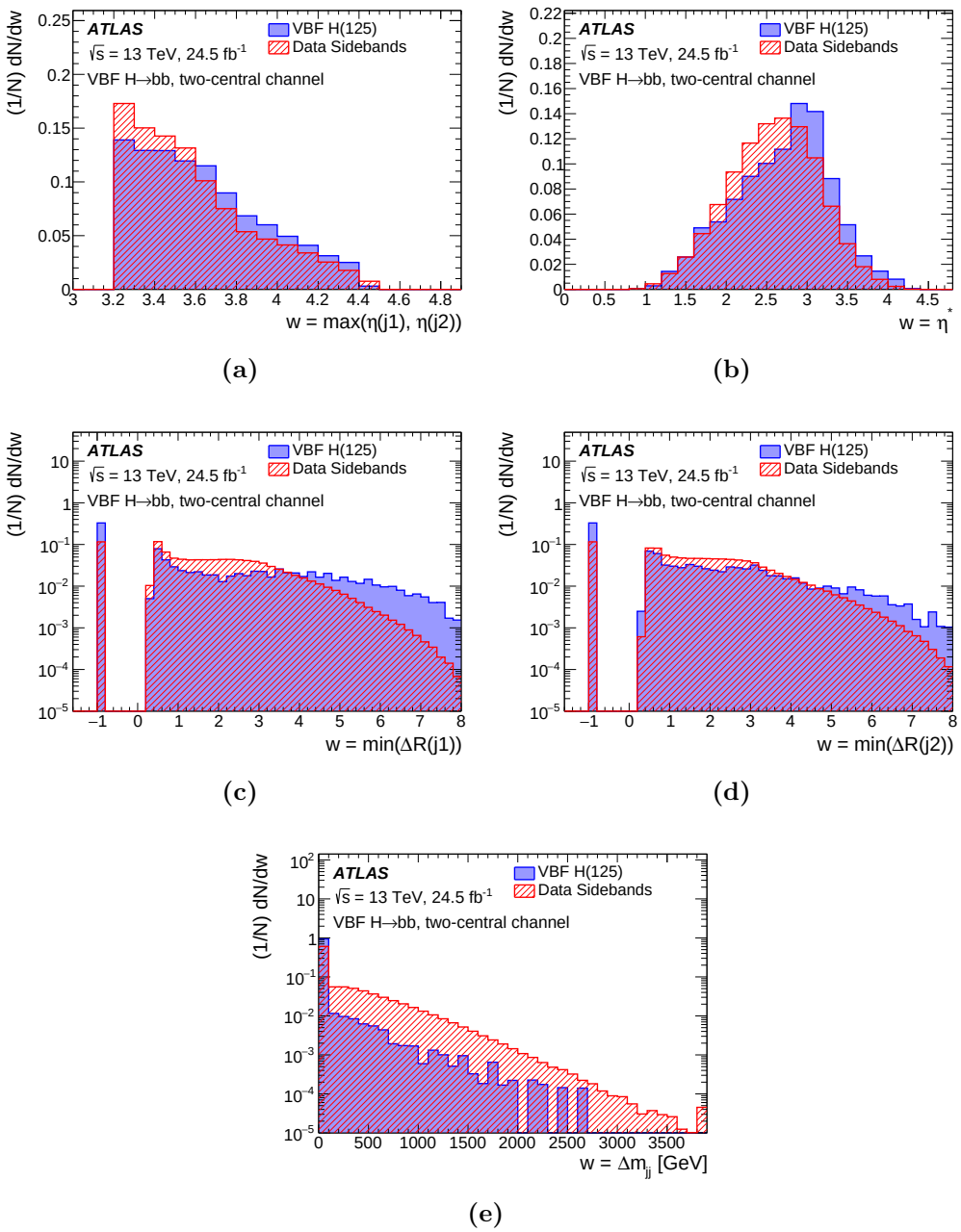

Figure 6.2: *Distributions (two-central channel) of the input variables for the multivariate analysis.*

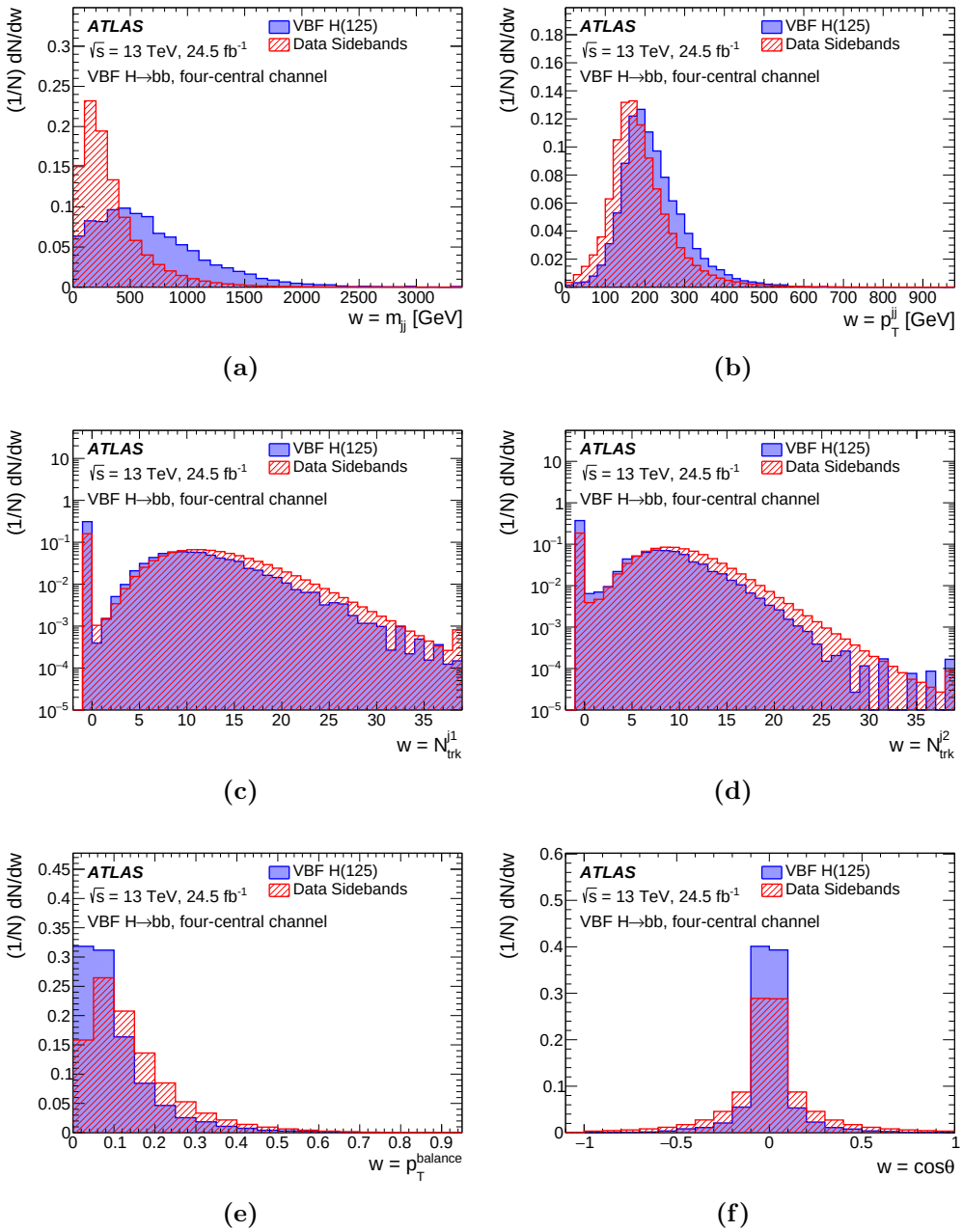

Figure 6.3: *Distributions (four-central channel) of the input variables for the multivariate analysis.*

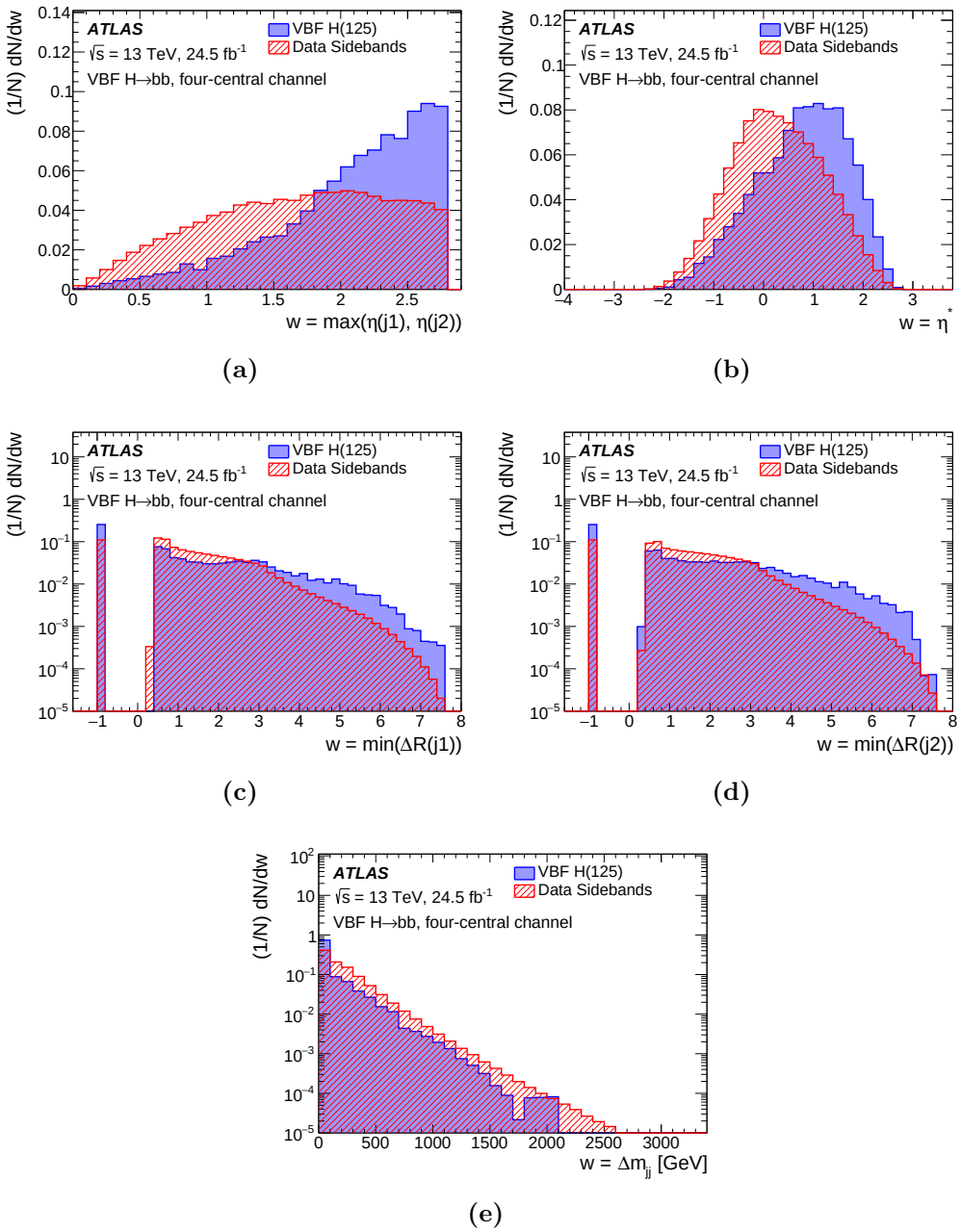

Figure 6.4: *Distributions (four-central channel) of the input variables for the multivariate analysis.*

- $max(|\eta_{j1}|, |\eta_{j2}|)$: the maximum absolute value of the VBF jet pseudorapidities

- $\eta^* = \frac{1}{2}(|\eta_{j1}| + |\eta_{j2}| - |\eta_{b1}| - |\eta_{b2}|)$: the average pseudorapidity difference between VBF and signal jets. This variable discriminates between QCD multijets events, which have no average pseudorapidity difference, and VBF processes, where the VBF jets are on average more forward than the signal jets

- $min\Delta R(j1)$: minimum angular separation between the leading VBF jet and the closest jet with $p_T > 20$ GeV nad $|\eta| < 4.4$ which is not a signal or VBF jet

- $min\Delta R(j2)$: minimum angular separation between the sub-leading VBF jet and the closest jet with $p_T > 20$ GeV nad $|\eta| < 4.4$ which is not a signal or VBF jet

- Δm_{jj}: the difference between the invariant mass of the VBF jet pair and the largest invariant mass of any jet pair in the event, excluding the two jets forming the Hggs boson candidate

These are shown in figure 6.1 and figure 6.2 for the *two-central* channel and figure 6.3 and figure 6.4 for the *four-central* channel. Figure 6.5 show the output MVA distributions.

Events have been categorized according to the BDT outputs in different regions. For the *two-central* channel, the BDT regions have been defined according to a conservative approach that ensures a constraining power of the $Z \to b\bar{b}$ contribution sufficient to prevent biasing the Higgs signal strength. We defined two regions:

- **SR-II**: $BDT < -0.006$

- **SR-I**: $BDT > -0.006$

For the *four-central* channel, the BDT regions have been defined in order to maximise $\frac{S}{\sqrt{B}}$, where S and B are the number of signal end expected background events in the $100 < m_{b\bar{b}} < 140$ GeV region, respectively. We defined five regions:

- **Region 0**: $-1.00 < BDT \leq +0.002$

- **SR-IV**: $+0.002 < BDT \leq +0.015$

- **SR-III**: $+0.015 < BDT \leq +0.026$

- **SR-II**: $+0.026 < BDT \leq +0.033$

- **SR-I**: $+0.033 < BDT \leq 1.00$

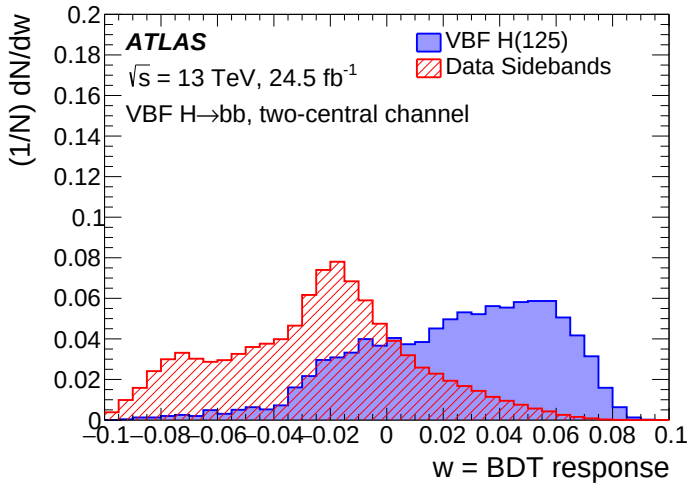

(a)

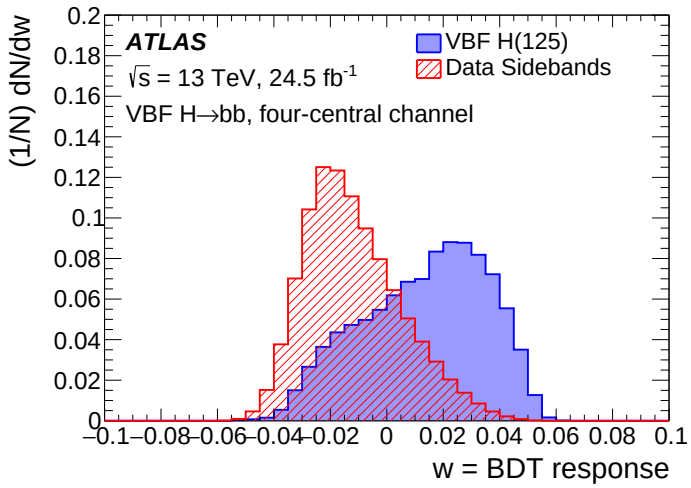

(b)

Figure 6.5: *Distribution of the BDT response for the two-central channel (top) and the four-central channel (bottom), on data and signal MC simulation.*

Region 0 possesses the lowest VBF significance. As a consequence, the data it contains will not be used in the signal search. The remaining regions have been used for the signal extraction.

From simulation it is determined that only 0.11% and 0.047% of the inclusive VBF signal MC would pass selections of both analyses given that they pass two-central and four-central, respectively. For the two analyses to remain orthogonal, our analysis vetos data events selected by the $H\gamma jj \rightarrow b\bar{b}\gamma jj$ analysis.

6.4 Fit Strategy

The strategy for the statistical treatment is similar to what has been already described in section 5.4, with few differences. The shape of resonant contributions ($H \rightarrow b\bar{b}$ and $Z \rightarrow b\bar{b}$) have been modelled with Bukin functions, while the shape of the combinatorial background will be determined on real data. The yields of all the fit components have been determined on data. The $Z \rightarrow b\bar{b}$ normalization is allowed to float independently in the BDT categories.

The criteria followed for selecting the analytical function for describing the background are based on few considerations: the probability associated to the χ^2 values; the probability associated to the F-Test, which is performed with respect to the $n+1$ order function; spurious signal tests, in order to check possible biasses on the Higgs yield. Among the candidates satisfying the above conditions, the function with the smallest number of degrees of freedom is chosen. We retained only the functions with a $\mathcal{P}(\chi^2, dof) > 0.05$ and $\mathcal{P}(F-Test) > 0.05$. Following these criteria only $O(3)$ Bernstein polynomials were found to be suitable analytical models of the background, with the exeption of SR-IV of the *four-central* channel for which a $O(4)$ Bernstein polynomial was needed.

The statistical analysis follows what was done in the previous iteration of the analysis: a binned profile likelihood fit performed simultaneously in all the BDT regions. The Higgs signal (Z) strength parameter, μ (μ_Z), multiplies the expected SM Higgs (Z) boson production cross section in each bin. Systematic contributions are accounted for through NPs, as was done in 2012.

Finaly, a second fit has been performed in order to extract the VBF-specific strength μ_{VBF} following the same procedure as described above.

6.5 Systematic Uncertainties

The systematic uncertainties for the background and signal expectations are divided into experimental, theoretical uncertainties and non-resonant background uncertainty. All uncertainties are propagated to the BDT input variables and then to the final likelihood fits, with the exception of the

luminosity uncertainty, which is taken as a constant uncertainty. Table 6.2 summarized the magnitude of the systematic contributions.

Source of uncertainty	$\sigma(\mu_H)$		$\sigma(\mu_{VBF})$	
Total statistical uncertainty	+1.3	−1.3	+1.6	−1.5
Data statistical uncertanty	+0.6	−0.4	+0.9	−0.9
Non-resonant background	+1.0	−1.0	+1.2	−1.2
$Z + jets$ normalization	+0.5	−0.5	+0.5	−0.5
Total systematic uncertainty	+0.6	−0.4	+0.6	−0.5
Higgs boson modeling	+0.3	−0.1	+0.2	−0.1
JES/JER	+0.3	−0.2	+0.4	−0.2
b-tagging	+0.2	−0.1	+0.2	−0.1
Other experimental uncertainty	+0.4	−0.3	+0.4	−0.4
Total	+1.4	−1.3	+1.7	−1.6

Table 6.2: *Systematic uncertainties and their contribution for both the μ_H and μ_{VBF} extraction procedures.*

6.5.1 Experimental uncertainties

The major sources of jet-related uncertainty comes from the jet energy scale (JES) and jet energy resolution (JER). These are determined by using Z, photon, and multijet p_T-balancing techniques in data [115]. The systematic uncertainty due to the JER is calculated by increasing the resolution within its uncertainties, smearing the jet energy by the resulting change in resolution, and comparing the result to the nominal shape and normalization in simulation.

The uncertainties related to the b-tagging of jets are accounted for as scale factors. These are determined from data using $t\bar{t}$ events, $W + c$ and D^* meson events, and multi-jet data [116, 117].

The effects of uncertainties related to the number of tracks associated with a jet, is derived by removing or adding tracks according to the tracking efficiency and fake-rate estimates [118]. Uncertainties in the modeling of track multiplicity are derived from the measurement of the charged-particle multiplicity inside jets from $\sqrt{s} = 8$ TeV pp collisions [119].

Other uncertainties affect the $H\gamma jj \rightarrow b\bar{b}\gamma jj$: photon energy uncertainties. These are computed from calibration studies in data and data-to-simulation comparisons [120, 121]. In order to take into account a shift between the data and simulation distributions the photon isolation energy a data-driven correction is applied and the difference between the uncorrected and corrected isolation energy is taken as a systematic uncertainty.

6.5.2 Theoretical Uncertanties

The value of the $H \to b\bar{b}$ branching ratio and its uncertainty are taken from the LHC Higgs Cross Section Working Group [122] and are calculated with the HDECAY program [123]. Uncertainties in the cross section and acceptance for VBF and ggF signals due to the missing higher-order terms in perturbative QCD calculations are evaluated by varying the choice of renormalization scale and factorization scale independently by factors of 0.5 and 2.0.

The uncertainty from the parton-shower and underlying-event models is estimated by comparing the nominal sample, which uses PYTHIA 8.2 for parton showering, with an alternative sample using HERWIG 7.0 for parton-shower generation. This uncertainty is 4%–12%.

The contributions of the VH and $t\bar{t}H$ Higgs boson production modes to the signal regions of the all-hadronic channels are also taken into account. They are small in the most sensitive signal regions (0.2%–3%) and rise to 20% in the least sensitive regions.

6.5.3 Non-resonant background uncertainties

The uncertainty due to the non-resonant background modeling is included by determining the largest spurious signal induced in Asimov data sets derived with alternative functions. These alternative functions must pass the χ^2 and F-test as described in section 6.4. The size of the spurious signal is taken as the uncertainty.

6.6 Results

The Higgs boson signal strength is extracted from an extended maximum-likelihood fit to the b-tagged di-jet invariant mass spectrum $m_{b\bar{b}}$ in data. The fit covers the $m_{b\bar{b}}$ range from 80 GeV to 200 GeV

Two different extraction procedures have been performed: one for extracting the inclusive signal strenght μ_H, which comprises all production modes (ggF, VBF, VH and $t\bar{t}H$); one for extraction of the VBF-only signal strength μ_{VBF}. In the former, the ratio of the different production mechanisms are fixed to the SM expectations. In the latter, the contributions from the non-VBF components are constrained to the SM predictions. Figure 6.6 shows the fit to the $m_{b\bar{b}}$ spectrum obtained when extracting μ_H.

A test statistic q_μ based on the profile likelihood function is used to determine the compatibility of the background-only model with the data, and to determine exclusion intervals using the CLs method. We derive 95% C.L. upper limits on $H \to b\bar{b}$ production in both the inclusive and VBF channels. The results are consistent with Standard Model expectations within the uncertainties.

The observed signal strength for the inclusive signal and the VBF-signal

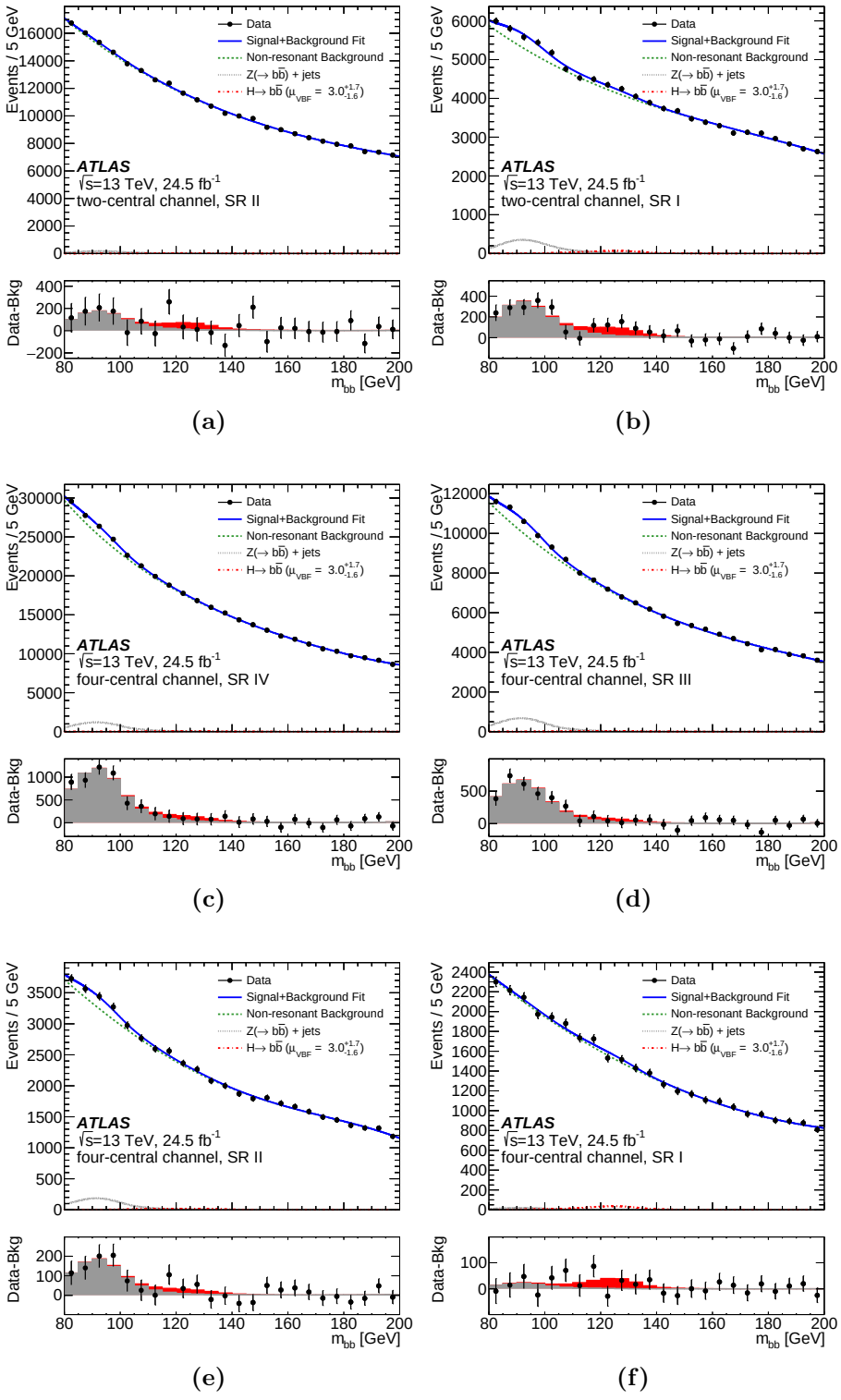

Figure 6.6: *Results of the profile likelihood fit to the $m_{b\bar{b}}$ distributions in the BDT categories. The points represent the data, and the histograms represent the non-resonant background (blue line) and the Z (grey line) and Higgs contributions (ref line). In the lower panels, the data after subtraction of the non-resonant background are compared with the fit to the Z and Higgs contributions.*

have been foud to be respectively:

$$\mu_H = \frac{\sigma_H}{\sigma_{SM}} = 2.5^{+1.4}_{-1.3} \tag{6.1}$$

$$\mu_{VBF} = \frac{\sigma_{VBF}}{\sigma_{SM}} = 3.0^{+1.7}_{-1.6} \tag{6.2}$$

The observed significances of both the inclusive and VBF-only production are 1.9σ, compared with 0.8σ expected for the inclusive production and 0.7σ expected for the VBF production. Figure 6.7 and table 6.3 show the signal extraction results.

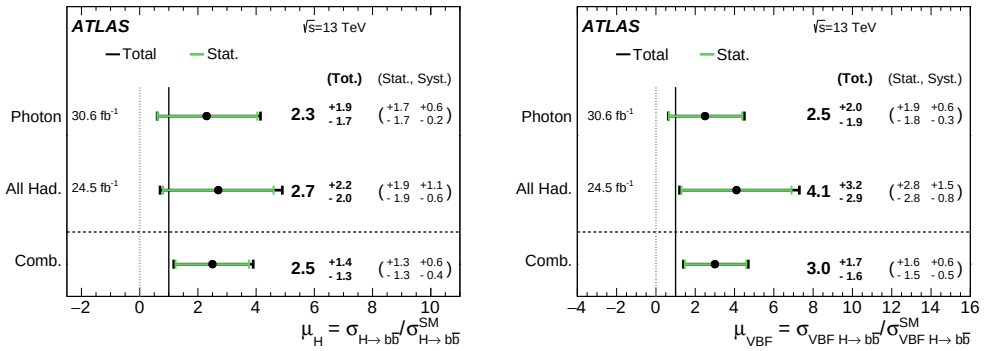

(a) **(b)**

Figure 6.7: *Summary of the all-hadronic, photon and combined results for the fitted signal strength parameters μ_H and μ_{VBF}.*

	Inclusive Production	VBF production
Expected significance	0.8σ	0.7σ
Observed significance	1.9σ	1.9σ
Expected limit on signal strength	$2.5^{+1.0}_{-0.7}$	$3.0^{+1.3}_{-0.8}$
Observed limit on signal strength	4.8	5.9
Expected signal strength	1.0 ± 1.2	1.0 ± 1.5
Observed signal strength	$2.5^{+1.4}_{-1.3}$	$3.0^{+1.7}_{-1.6}$

Table 6.3: *Expected and observed results for the Higgs boson production rate, for both inclusive production and VBF production only, relative to the Standard Model prediction. The limits shown refer to 95% CL upper limits.*

CHAPTER 7

Future Improvements

In this chapter we will discuss some of the possible improvements, both at analysis and at trigger level. The improvements to the analysis affect the next iteration of the VBF $H \to b\bar{b}$ analysis, with the aim of enhancing the trigger acceptance and to reduce the uncertainty related to the background modelling. The improvements to b-jet trigger – and online flavour tagging – are foreseen for Run-3 and are aimed mainly at improving performances at high p_T and to address the software and CPU requirements for the next data-taking period.

7.1 Improving the b-tagging performances at high p_T

The b-tagging performances are represented by the light-jet and c-jet rejection curves expressed in terms of b-jet efficicency (e.g. figures 3.8 and 3.9). As a function of p_T these performances decrese, a symptom that the MVA algorithms are less and less capable of distringuishing between light-, c- or b-jets. This behavour has a huge impact for the analyses aiming at phase spaces with highly impulsive b-jets, in particular seaches in the boosted regimes.

Two considerations can be made. Firstly, the training and testing of the flavour tagging algorithms are usually performed on a $t\bar{t}$ Monte Carlo sample that is limited in statistics at high p_T. As a consequence, the b-tagging algorithm does not efficiently learn to discriminate b-jets from light- or c-jets. Secondly, the MV2 algorithms receives as input the outputs from lower-level-taggers such as IP3D. The use of recurrent-neural-network track-based taggers may improve impact parameter resolutions for high p_T tracks. For b-jets, track impact parameters are intrinsically correlated. If there is a track with a large impact parameter, then there is likely a second track with large impact parameter. If no displaced decay is present, like in light-flavor jets, such correlations should not exist. Recurrent neural network makes use of the track impact parameter correlation.

Thus, the introduction of two new elements in the online flavour tagging

will result in enhanced performances of b-jet triggers at high p_T: MVA training on an mixed sample of $t\bar{t}$ and Z' events – the so-called Hybrid tuning –; and the addition of new taggers based on recurrent-neural-networks.

Figure 7.1 shows the online efficiency with respect to the offline b-tagging as a function of the impulse of the offline jets. The offline b-tagging working point has a 70% efficiency on b-jets, while the online b-tagging working point has a 60% efficiency. The taggers used are MV2c10 for the offline, and MV2c20 for the online environment.

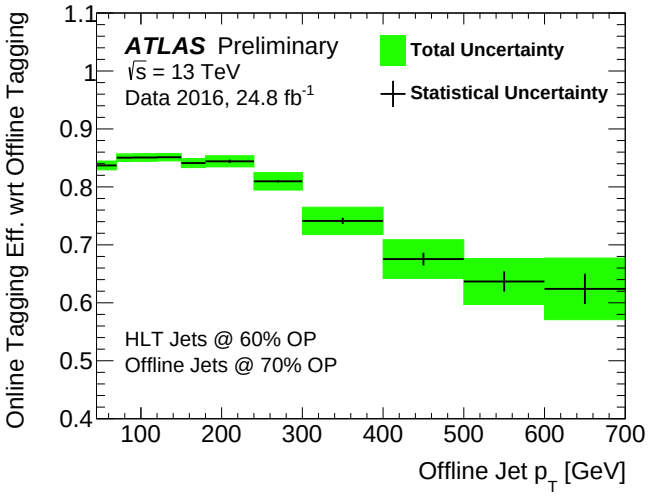

Figure 7.1: *The b-jet trigger efficiency at the 60% online operating point with respect to offline b-tagging at the 70% offline operating point as a function of offline jet-p_T. Systematics account for non b-jet contamination and the simulation-based extrapolation to high jet-p_T.*

The decrese of efficiency is symptomatic of the presence of some additional differences between the online and offline environments – albeit the software is the same – that makes us loose efficiency at high p_T with respect to the offline b-tagging. This is a current subject of our investigations.

7.1.1 Hybrid flavour tagging tuning

The use of a $t\bar{t}$-only training sample is not optimal if the phase space we are interested in comprises high-p_T jets: the training sample provides a poor statistics in that region of the p_T spectrum, with a consequent lack of efficient performance of the MVA algorithms. Indeed, the b-tagging efficiency decreases with p_T. In order to overcome this issue, a new training sample has been introduced, while keeping the algorithms structure unchanged: a mixture of $t\bar{t}$ events (for low-p_T); and Z' (for high p_T), where the heavy vector boson (Z') has a mass of 1 TeV and is produced by the generator with a flat p_T spectrum. The mixture is based on the b-Hadron p_T for b-jets, and on the jet p_T for c- and light-jets. Figure 7.2 shows the b-Hadron p_T distributions of both the $t\bar{t}$ and Z' samples: while the former is concentrated at $p_T < 400$ GeV, the latter exstends to much higher values.

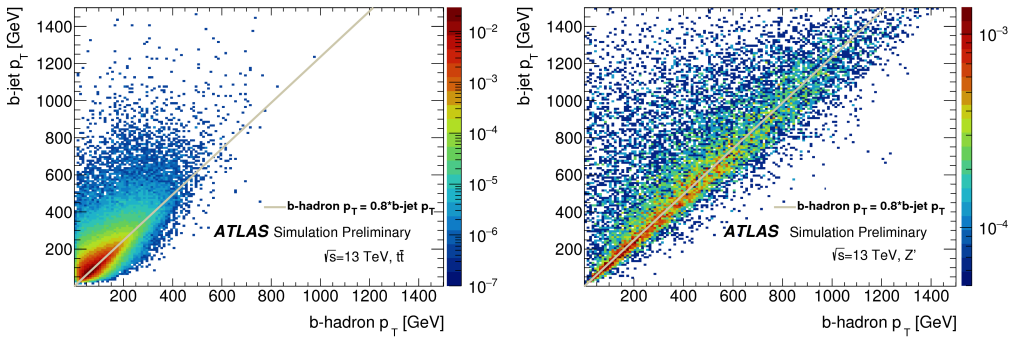

(a) (b)

Figure 7.2: *Two-dimensional correlations between the b-hadron and the b-jet transverse momenta for $t\bar{t}$ (a) and Z' (b) events.*

Introduced at first in the offline environment, this new hybrid tuning has been migrated to the online level. In 2018 a new online tagger, the hybrid MV2c10, has been deployed during data taking for commissioning purposes. This is expected to improve performances at high p_T ($p_T > 275$ GeV), while keeping almost unchaged the performances al lower p_T: in this region the training sample is completely dominated by the $t\bar{t}$ sample.

7.1.2 New taggers

New b-tagging algorithms may improve performances of b-tagging at high p_T. Amidst high level taggers, we may cite two variants of the already mentioned MV2 algorithm that use some additional input variables: MV2Mu that receives as input the output of the Soft Muon Tagger (SMT) algorithm – based on the reconstruction of muons coming from semileptonic decays of heavy-flavour hadrons – ; and MV2MuRnn that uses the outputs of SMT and of a recurrent Neural Network Track-based IP taggers (RNNIP). Figure 7.3 shown the ligh-jet and c-jet rejection curves as a function of p_T produced by these new taggers at offline level [124].

The introduction of SMT and RNNIP produces a performance enhancement, with the two algorithms contributing with different magnitude according to the p_T region. While SMT produces significant performance gains at low p_T ant none at medium-high p_T, the RNNIP algorithm shows the opposite behaviour by starting to improve performances at around 300 GeV. However, at online level the use of the SMT is not yet feasible due to CPU constrains: this would require adding muon reconstruction to the already complex b-jet trigger algorithm sequence, thus increasing the CPU comsumption of the b-jet trigger signature. We are currently evaluating the introduction of RNNIP at online level.

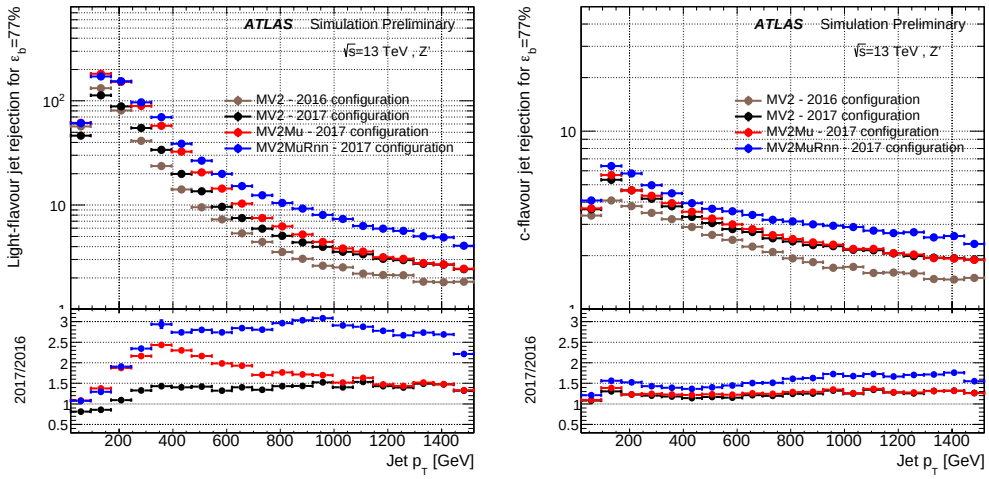

(a) **(b)**

Figure 7.3: *Light-flavour (a) and c-jet (b) rejection as a function of the jet p_T for the offline MV2 in the 2016 configuration (brown markers), MV2 (black markers) in the 2017 configuration, MV2Mu (red markers) and MV2MuRnn (blue markers). The algorithm evaluation is performed on Z' events. The ratio is calculated with respect to the 2016 configuration.*

7.2 Fast Tracker (FTK)

Tracking is the main CPU consumer within the b-jet chain sequence (see figure 3.3). This represents a processing time problem that forbids a full-scan tracking to be performed due to the current technical constrains. However, flavour tagging relies on a precise computation of tracks and vertices and as such the granularity of the information cannot be sacrified. To overcome this problem, the rate of execution of the tracking algorithm is limited so that tracking is performed on a few selected regions of the detector: a sub-set of the *L1* regions of interests. Moreover, the higher the number of interactions μ, the higher the p_T and/or b-tagging thresholds we have to apply in order to satisfy the CPU constrains.

The so-called Fast Tracker (FTK) [125] is a system of electronics with the aim of performing global tracking reconstruction with good resolution after L1 selection and to provide reconstructed tracks to HLT. FTK is based on an associative memory system that takes care of pattern recognition by comparing hits at reduced resolution with prestored patterns in a highly-parallelized fashion. This opens up the possibility of computing b-tagging on multi-jet triggers at a higher rate than currently possible and can allow us to lower the p_T thresholds of our triggers, giving analyses access to phase spaces not available in the past. This could potentially provide the ATLAS trigger with the sensitivity for models with many moderate momentum b-quarks which were previously inaccessible [126].

At the present moment FTK is already implemented in b-jet chains in three different fashions. These three flavours differ according to where in the b-jet sequence of algorithms and how FTK tracks are used. Figure 7.4

describes how these FTK-chains are implemeted, in comparison with the current b-jet chain sequence.

- **FTKVtx**: FTK tracks are used only for determining the Primary Vertex position, precision tracking will be performed as currently done
- **FTK**: FTK tracks will be used both for determining the Primary Vertex position and for precision tracking
- **FTKRefit**: same use of FTK tracks as in FTK, but for precision tracking we perform a refit of the tracks with offline-like track fitter

We are evaluating the effect on the impact parameters (e.g. d_0 and z_0 resolution) given by the different configurations. These variables are inputs to the MV2 b-tagging algorithms, thus they have a huge inpact on the b-tagging performances. As such, new flavour tagging online tunings have to be produced so that the maximum of tagging performances can be achieved.

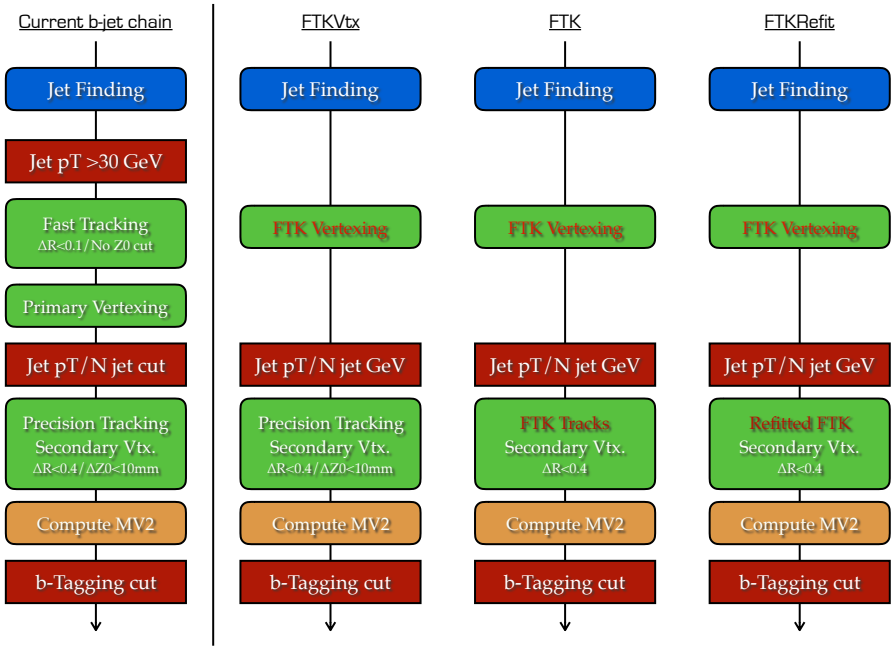

Figure 7.4: *Comparison of the current b-jet trigger sequence of algorithm and the sequence of algorithms including FTK tracks. Att the three different FTK b-jet chains flavours are reported.*

7.3 AthenaMT

Inside the ATLAS comunity the software framework of the collaboration is called Athena. This has been designed in order to process events in a

serial fashion, thus running algorithm sequentially on each event. This is the current configuration of the ATLAS software framework.

The inevitable increase in the number of CPU cores and threads, and the consequent increase of their cost, foreseen for addressing the technical needs of future operation at High Luminosity LHC (HL-LHC), require the deployment of new techniques to reduce the memory usage. A concurrent execution of algorithms on multi-core processors will reduce the total memory requirement and increase event throughput: parallelisation of algorithms within an event; event-wise parallelisation; and reentrant algorithms, such that a single algorithm instance can be executed concurrently in different threads. This new multi-thread software framework is commonly referred to as AthenaMT [127, 128].

Despite the change to a multi-thread software is required for Run-4 operations, such a major change of the HLT framework would need to be deployed already during the next long shutdown preceeding Run-3. The target is to have the upgraded HLT software ready for 2021 operations. Thus, a massive campaign of code migration – from a sequential to a parallel implementation – is being conducted. I am taking care of the b-jet trigger code migration to this multi-threads environment, which requires a complete redesign of b-jet chain's sequence of algorithms.

7.4 Improvements on the VBF $H \to b\bar{b}$ analysis

The main problems that affect the VBF $H \to b\bar{b}$ analysis are the low trigger acceptance and the huge background modelling systematics. These problems affected both iterations of this analysis, and we have tried to address these problems by introducing new triggers and revising the statistical tratment. This is true as well for the next iteration of this analysis, which will analyse the data collected during 2017 and 2018 operations.

7.4.1 VBF Triggers

New trigger options have been evaluated and adopted for the future interactions of the analysis, with the aim to increase the trigger efficiency and to lower as much as possible the p_T thresholds. Firstly, new HLT triggers have been introduced during 2017 that exploit the use of L1Topo items for computing, already at L1, the invariant mass (m_{JJ}) and the scalar sum of jet's p_T (H_T). Secondly, the decoupling of the jet topology and the b-tagging requirements – obtained by requiring a logical AND between a pure jet trigger and a b-jet trigger. Some preliminary studies showed that the use of these new triggers results in: lower p_t threshold with respect to previous triggers; gain in trigger acceptance; and higher signal efficiency, with less background in the signal window. These new triggers are summarized in table 7.1.

2017 and 2018 Trigger	
Without L1Topo	HLT_j55_gsc80_bmv2c1070_split _j45_gsc60_bmv2c1085_split_j45_320eta490
	HLT_j45_gsc55_bmv2c1070_split _2j45_320eta490_L1J25.0ETA23_2J15.31ETA49
	HLT_j80_0eta240_j60_j45_320eta490 _AND_2j35_gsc45_bmv2c1070_split
With L1Topo	HLT_ht300_2j40_0eta490_invm700 _L1HT150-J20s5.ETA31_MJJ-400-CF _AND_2j35_gsc45_bmv2c1070_split

Table 7.1: *List of the b-jet triggers available during 2017 and 2018 data-taking period that the VBF $H \to b\bar{b}$ analysis will use. This comprises a trigger relying on L1Topo.*

Concerning the triggers non relying on L1Topo, there are three of them. One trigger requires two jets in the central region of the detector – one with $p_T > 80$ GeV and satisfying the online 70% b-tagging working point, and another one with $p_T > 60$ GeV and satisfying the online 85% b-tagging working point – and one in the forward region with $p_T > 45$ GeV. A second trigger that impose one jet in the central region with $p_T > 55$ GeV and satisfying the online 70% b-tagging working point, and two jets with $p_T > 45$ GeV in the forward region of the detector. A third trigger (only available in 2018) decouples the jet topology and the b-tagging requirements. This trigger requires at least three jet: one jet with $p_T > 80$ GeV and $|\eta| < 2.4$; a second one with $p_T > 60$ GeV and $|\eta| < 3.2$; and a third one with $p_T > 45$ GeV and $3.2 < |\eta| < 4.9$. In addition to this, two jets with $p_T > 45$ GeV and satisfying the online 70% b-tagging working point are required. These jets may be the same jets asked by the first part of this trigger.

Concerning the trigger relying on L1Topo, it imposes an m_{JJ} of at least 400 GeV, and an $HT > 150$ GeV. The former requires one jet in the central region of the detector ($|\eta| < 3.1$) and one in the forward region ($|\eta| > 3.1$), the latter quantity is computed considering L1 jets with $p_T > 20$ GeV. At HLT level, the requirements on HT and the invariant mass are 300 and 700 GeV respectively. The jet topology and the b-tagging requirements are independently imposed: two jets with $p_T > 40$ GeV and with $|\eta| < 4.9$ are required; and two jets with $p_T > 40$ GeV and satisfying the 70% online b-tagging working point.

7.4.2 Background Modelling

The main source of uncertainties in both the iterations of the VBF $H \to b\bar{b}$ analysis come from the background modelling systematic. The fits were performed by using a different analytical function for each BDT category, the only common parameter was the Higgs signal strength μ_H. This led

to a huge number of floating parameters, and thus to a big contribution of the background modelling systematic. The use of a common analytical function across multiple BDT regions would be advisable, providing a huge constraining power on the background shape. However, the $m_{b\bar{b}}$ distributions were found not to be suitable for accomodating such a situation.

The different $m_{b\bar{b}}$ distributions in the BDT regions are a result of the use of not-fully mass-decorellated input variables to the MVA algorithm. This correlation propagated to the BDT output. There are however different techniques available for removing this correlation [129], thus minimizing the sculpting of the background jet mass distributions. This results in a more robust background estimation. One of these techniques implies the use of Adversarial-Neural-Networks (ANN) [130] in order to reduce the correlation with the $m_{b\bar{b}}$ mass [131].

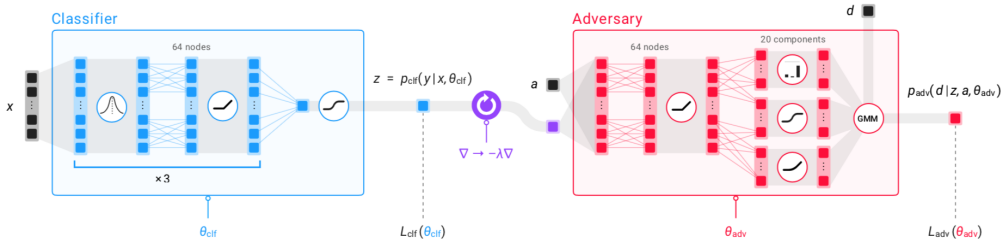

Figure 7.5: *Scheme of an Adversarial Neural Network (ANN). Two different Multivariate Algorithms are trained: a classified, which is aimed at discriminating the signal and the background; and an adversary, tasked with inferring the $m_{b\bar{b}}$ mass from the output of the classifier.*

The ANN trains two Neural Networks: a classifier, aiming at discriminating the signal and the background; and an adversary, tasked with inferring the $m_{b\bar{b}}$ mass from the output of the classifier. If a correlation between the classifier's output and $m_{b\bar{b}}$ is present, then the adversary network will be able to infer the invariant mass, beyond random guessing. Such a MVA algorithms tries balancing the classification and the decorrelation tasks. This is done with an optimization of the classifier loss L_{clf} and the adversary loss L_{adv}:

$$L_{clf} - \lambda L_{adv} \tag{7.1}$$

The trade-off between the two is given by the λ parameter: in the case $\lambda \to 0$, the ANN reduces to the classifies; in the case $\lambda \to \infty$, the ANN only retains information completely independent of $m_{b\bar{b}}$. The λ parameter is an additional hyperparameter of the ANN and can be tuned according to some figure of merit.

Conclusions

This thesis presented a search for a Higgs boson produced via Vector Boson Fusion mechanism in the bottom quark pair decay channel, VBF $H \to b\bar{b}$ and illustrated how the use of flavour-tagging-based (b-jet) triggers is the key element for making such a study feasible. Two different iterations of the analysis have been published by the ATLAS collaboration, analysing $\sim 20\ fb^{-1}$ (at $\sqrt{s} = 8$ TeV) and $\sim 36\ fb^{-1}$ (at $\sqrt{s} = 13$ TeV) of collected-data respectively. They target the distinct final state of the VBF $H \to b\bar{b}$ signal that foresees the presence of four energetic jets: two b-jets from the Higgs boson decay, in the central region of the detector; and two jets, in the forward/backward region. This VBF-specific event topology is exploited both at trigger level and during the multivariate analysis in order to improve the sensitivity of the analysis.

The analysis of the 2012-collected data resulted in a Higgs signal yield of $\mu_H = -0.8 \pm 1.3(stat.)^{+1.8}_{-1.9}(syst.) = -0.8 \pm 2.3$. The upper limit on μ is observed to be $\mu = 4.4$ at the 95% CL,to be compared to the expected limits of 5.4 in the background-only hypothesis and 5.7 if Standard Model production is assumed. The analysis of the 2016-collected data resulted in a Higgs signal yield of $\mu_H = 2.5^{+1.4}_{-1.3}$, after the combination with the $H\gamma jj \to b\bar{b}\gamma jj$ channel. This translates into an observed (expected) 95% CL upper limits on the Higgs boson production cross section times branching ratio of 4.8 ($2.5^{+1.0}_{-0.7}$) times the Standard Model expectation.

The combination of this analysis with other production mechanisms (VH and $t\bar{t}H$) led to the observation of the Yukawa coupling with bottom quarks: the observed excess over the expected Standard Model background possesses a significance of 5.4 standard deviations compared to an expectation of 5.5. The measured signal strength with respect to the SM expectation is found to be $\mu_H = 1.01 \pm 0.12(stat.)^{+0.16}_{-0.15}(syst.)$. Such a result would not be achieved without this combination: the VH analysis alone (Run-1 and Run-2) resulted in a signal strength with respect to the SM prediction of $\mu_H = 0.98 \pm, 0.14(stat.)^{+0.17}_{-0.16}(syst.)$, corresponding to an observed significance of 4.9 standard deviations compared to an expectation of 5.1

APPENDIX A

Multivariate discriminant distribution in data sidebands

The dependence of the multivariate discriminant variable on the b-jet invariant mass pair has been studied by comparing the BDT distribution for data in the upper ([150,190] GeV) and lower ([70,90] GeV) sidebands.

The distributions for the eight input variables are shown in Fig. A.1, while Fig. A.2 shows the distributions for the BDT output.

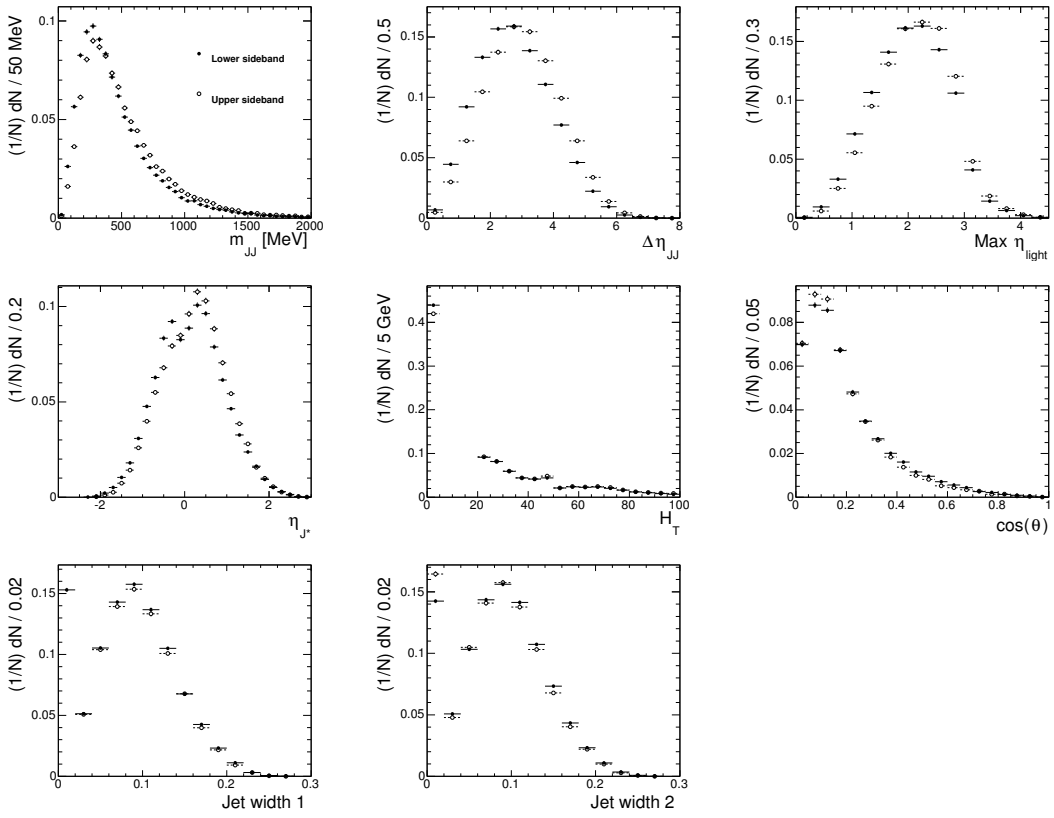

Figure A.1: *Distributions of BDT input variables for data in lower and upper sidebands*

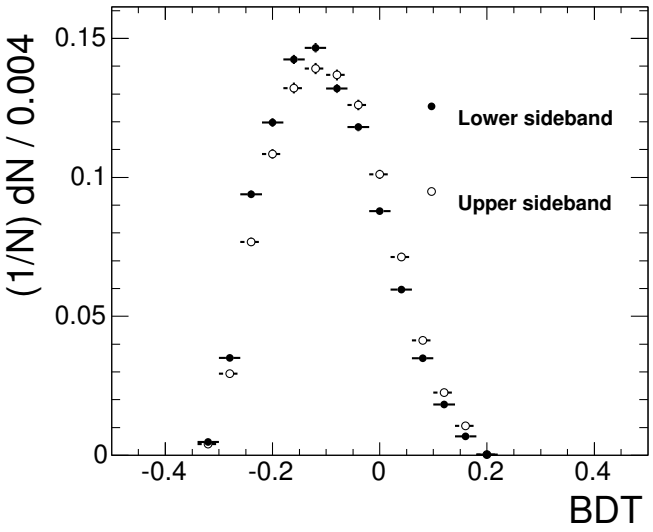

Figure A.2: *Distribution of BDT output variable for data in lower and upper sidebands*

APPENDIX B

Background systematics decomposition

The background systematics has been assessed by decomposing the bin-by-bin correlation matrices, obtained by means of TOY MC simulations, into their eigenvectors and retaining the most relevant ones (the weight being given by the corresponding eigenvalue). Each contribution has been introduced as an additional nuisance parameter in the profile likelihood.

Table B.1 summarizes the eigenvalues of the two matrices ($F1$ and $F2$), highlighting the contributions we retained in the analysis. Figure B.1 and B.2 show the weighted eigenvectors for each BDT region.

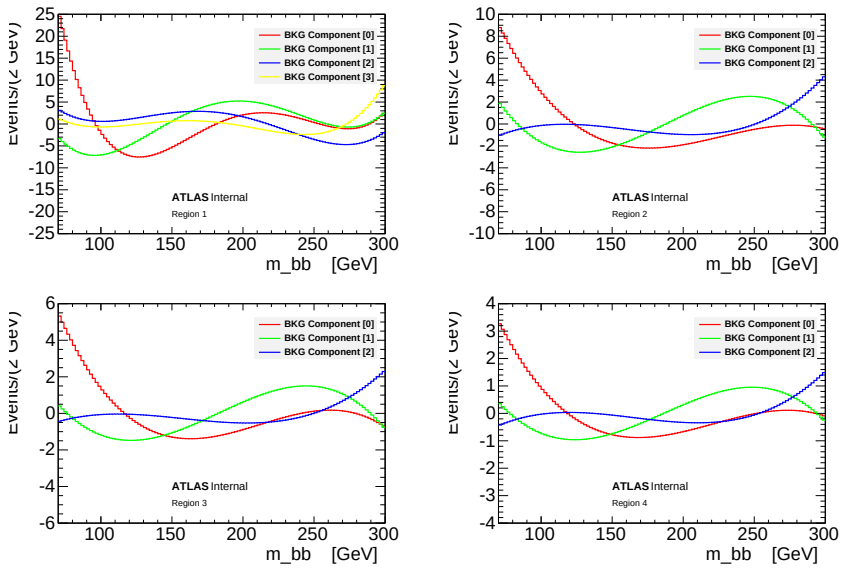

Figure B.1: *The retained background contributions for the $F1$ matrix in the four BDT regions.*

The effect on the systematic assessment due to the truncation of the eigenvectors has been investigated. For each BDT region we compared the quadratic sums of the eigenvector variations in each bin with the RMS

$F1$								
#	Region I		Region II		Region III		Region IV	
0	3630.04	X	733.277	X	243.61	X	97.5952	X
1	1824.93	X	357.527	X	123.292	X	51.2066	X
2	760.996	X	157.108	X	45.5687	X	18.2584	X
3	430.066	X	$< 1e-13$		$< 1e-14$		$< 1e-14$	
4+	$< 1e-13$		–		–		–	

$F2$								
#	Region I		Region II		Region III		Region IV	
0	64160	X	7755.06	X	435.875	X	257.587	X
1	734.17	X	185.74	X	63.1064	X	59.9399	X
2	325.538	X	32.0589	X	7.84637	X	2.11678	
3	22.4794	X	4.33319	X	1.74817	X	0.06060	
4	0.538303		1.14883		0.571695		0.01504	
5	0.293957		0.277527		0.028735		$< 1e-8$	
6	0.118331		0.0438789		0.007881		–	
7	$< 1e-5$		0.000202157		$< 1e-5$		–	
8+	–		$< 1e-7$		–		–	

Table B.1: *Eigenvalues of the correlation matrices, sorted accordingly to their magnitude. We retained the most relevant contributions, here highlighted with a X. Whenever not listed, the eigenvalue is negligible.*

spread obtained straight from the toys (i.e. the square root of the diagonal matrix elements).

Figure B.3 and B.4 show that the eliminated background's components are negligible and thus that the truncation of the eigenvectors does not introduce an underestimation of the background systematics.

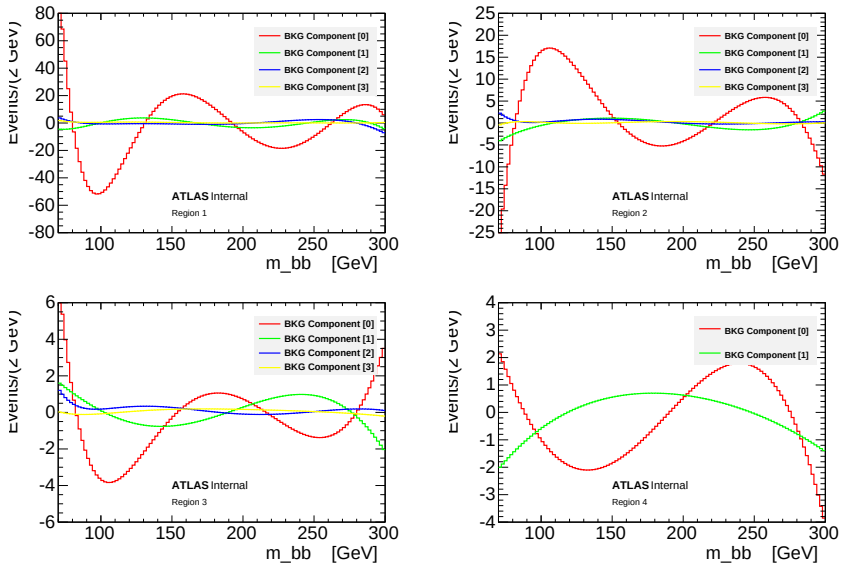

Figure B.2: *The retained background contributions for the F2 matrix in the four BDT regions.*

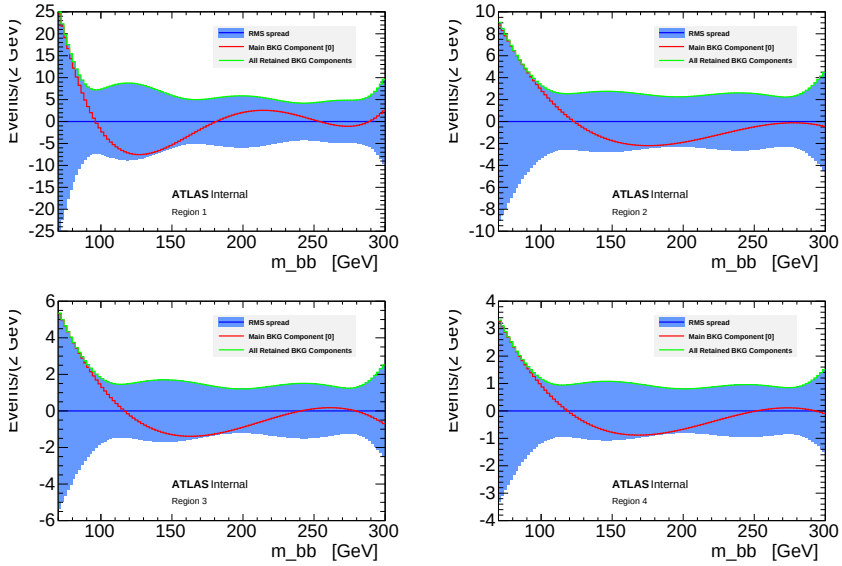

Figure B.3: *Comparison, in the four BDT regions, between the quadratic sum of F1's eigenvector variations in each bin (green line) and the RMS spread obtained from the toy MCs (blue histogram), i.e. the square root of F1's diagonal elements. The main background component is shown in red.*

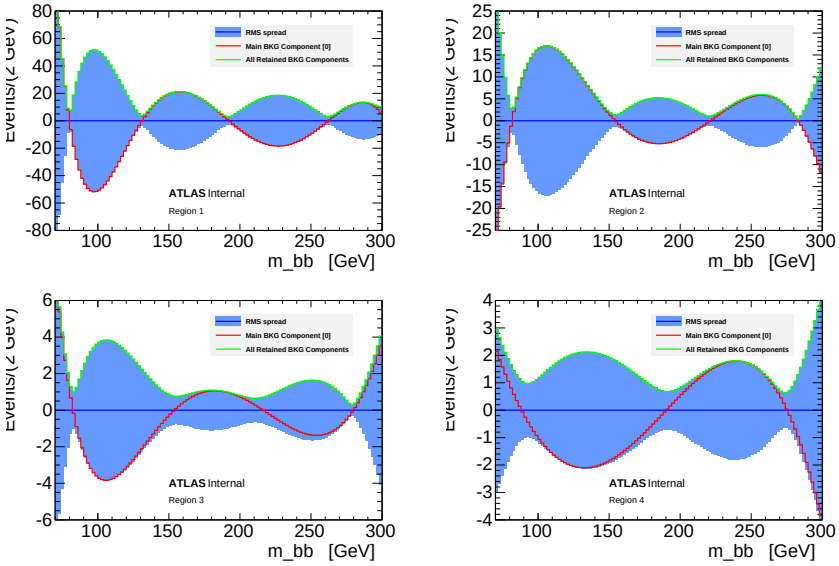

Figure B.4: *Comparison, in the four BDT regions, between the quadratic sum of F2's eigenvector variations in each bin (green line) and the RMS spread obtained from the toy MCs (blue histogram), i.e. the square root of F2's diagonal elements. The main background component is shown in red.*

APPENDIX C

Higgs and combined Z correlation

Error propagation is the problem of finding the distribution of a function of random variables. In this contest, considering a multiple-input system with several outputs, one can also evaluate the statistical dependence between these outputs – i.e. their correlation.

If we consider a system with several input variables X_i and multiple output variables Y_i, which are known functions of the inputs $Y_i = f_i(X_j)$, one can calculate the covariance between these outputs as:

$$\sigma_{Y_A Y_B} = \sum_i \sum_j \left(\frac{\partial f_A}{\partial X_i}\right) \left(\frac{\partial f_B}{\partial X_j}\right) \sigma_{X_i} \sigma_{X_j} V_{i,j} \tag{C.1}$$

where we indicated with $V_{i,j}$ the correlation between the X_i and X_j input variables and with σ_{X_i} the uncertainty on X_i.

For this specific analysis the system considered has two outputs: the Higgs signal strength $\hat{\mu}$ and the combined Z yield, as obtained in eq. **??**. The input variables are the nuisance parameters included in the profile likelihood fit.

For semplicity, we can indicate these two outputs as Y and Z:

$$Y = f(X_i) \equiv \hat{\mu} \tag{C.2}$$

$$Z = g(X_i) \equiv \frac{\sum_{c=I}^{IV} \mu_Z \times \alpha_{Z,c} \times N_{Z,c}}{\sum_{c=I}^{IV} N_{Z,c}} \tag{C.3}$$

Given the defintions of $f(X_i)$ and $g(X_i)$ equation C.1 can be reduced. Thus, only the correlations between $\hat{\mu}$ and μ_Z and the $\alpha_{Z,c}$ contribute to this calculation (the $N_{Z,c}$ being not correlated with anything). The relevant correlations, taken from the correlation matrix obtained in the profile likelihood fit, are reported on table C.1.

$$\sigma_{YZ} = \sum_j \frac{\partial g}{\partial X_j} \times \sigma_{\hat{\mu}} \times \sigma_j \times V_{\hat{\mu},j} \tag{C.4}$$

The derivatives are given by:

$$\frac{\partial g}{\partial \mu_Z} = \frac{\sum_{c=I}^{IV} \alpha_{Z,c} \times N_{Z,c}}{\sum_{c=I}^{IV} N_{Z,c}} \tag{C.5}$$

$$\frac{\partial g}{\partial \alpha_{Z,c}} = \frac{\mu_Z \times N_{Z,c}}{\sum_{c=I}^{IV} N_{Z,c}} \tag{C.6}$$

Dividing the covariance by the uncertainties on Y and Z (evaluated with eq. **??**) one obtaines the correlazion between these output variables. The calculation here described produces a correlation value of 0.22.

Parameter	Correlation with $\hat{\mu}$
μ_Z	2.05×10^{-1}
$\alpha_{Z,I}$	7.41×10^{-3}
$\alpha_{Z,II}$	7.20×10^{-2}
$\alpha_{Z,III}$	7.66×10^{-2}
$\alpha_{Z,IV}$	5.99×10^{-2}

Table C.1: *Correlation between the signal yield $\hat{\mu}$ and the relevant nuisance parameters that contribute to the calculation of the combined Z yield.*

APPENDIX D

Multivariate variables for the $H\gamma jj \to b\bar{b}\gamma jj$ channel

The selected input variables for the BDT have a minimal collelation with $m_{b\bar{b}}$:

- m_{jj}: the invariant mass of the VBF jet pair
- p_T^{jj}: the transverse momentum of the VBF jet pair
- N_{trk}^{j1}, N_{trk}^{j2}: the number of tracks with $p_T > 0.5$ GeV in the VBF jets, $j1$ and $j2$. This variable discriminates between gluon jets, which are more abundant in the background processes, and light-quark jets, which are present in the signal. The variable is only used with jets with $|\eta| > 2.5$
- $p_T^{ballance}$: the ratio of the vectorial and scalar sums of the jet (and photon, if applicable) trasverse momenta. This variable discriminates between electroweak signal processes, which tipically are balanced, and multijet QCD events, which are less ballanced
- $cos(\theta)$: cosine of the angle between the normal directions of the planes spanned bythe VBF jet pair and signal b-jet pair in the center of mass frame of the $jjbb$ system, which is related to the angular dynamics of the production mechanism
- $max(|\eta_{j1}|, |\eta_{j2}|)$: the maximum absolute value of the VBF jet pseudo-rapidities
- $\Delta R(b1, \gamma)$, $\Delta R(b2, \gamma)$: angular separation between the signal b-jets and the photon
- $\Delta\eta_{jj}$: η separation between the VBF jets
- $centrality(\gamma, jj) = \left| \frac{y_\gamma - \frac{y_{j1}+y_{j2}}{2}}{y_{ji}-y_{j2}} \right|$: centrality of the photon relative to the VBF jets

- $\Delta\phi(bb, jj)$: azimuthal angle between the VBF jet pair and the signal b-jet pair

Figure D.3 shows the output BDT distribution.

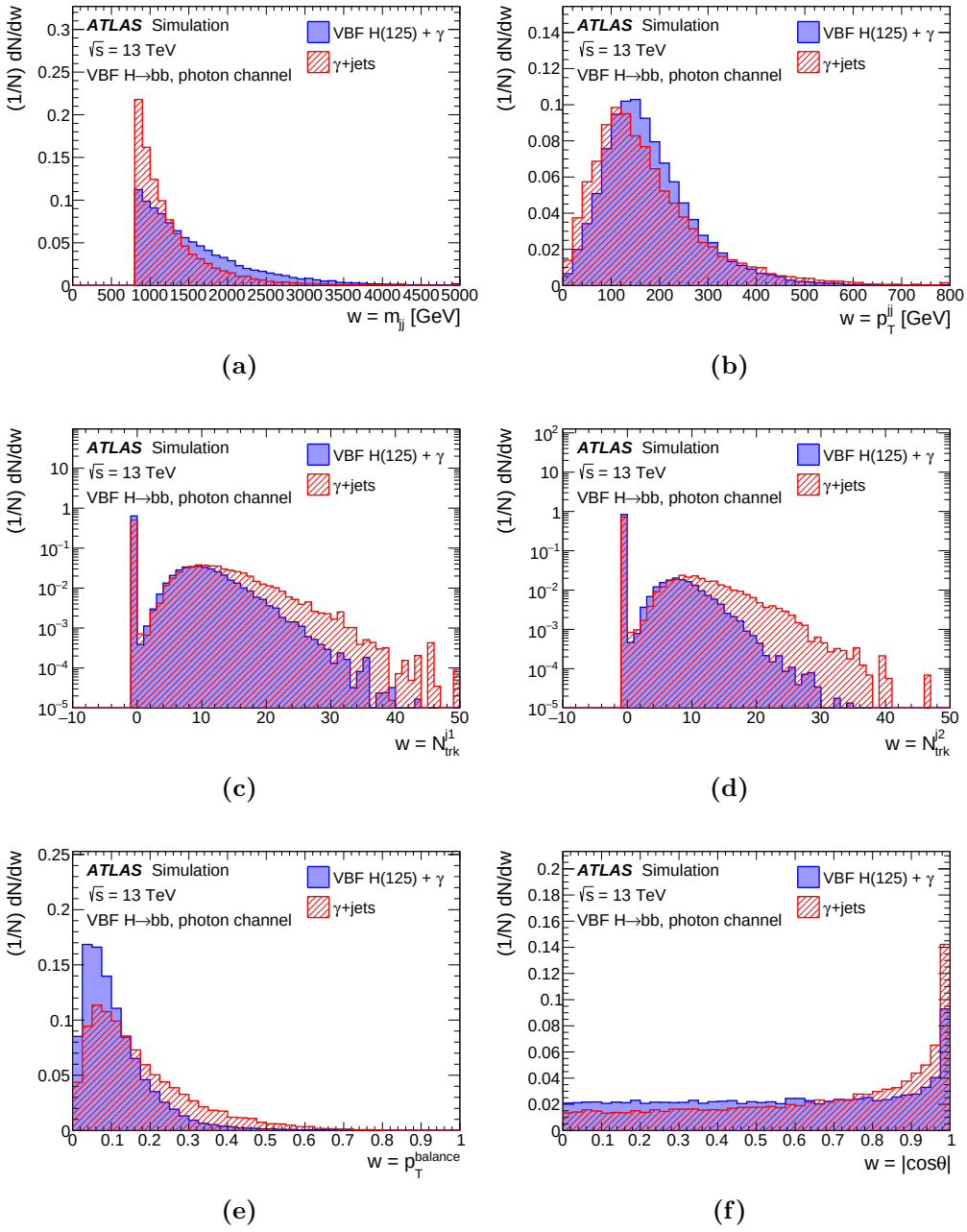

Figure D.1: *Distributions of the input variables for the multivariate analysis.*

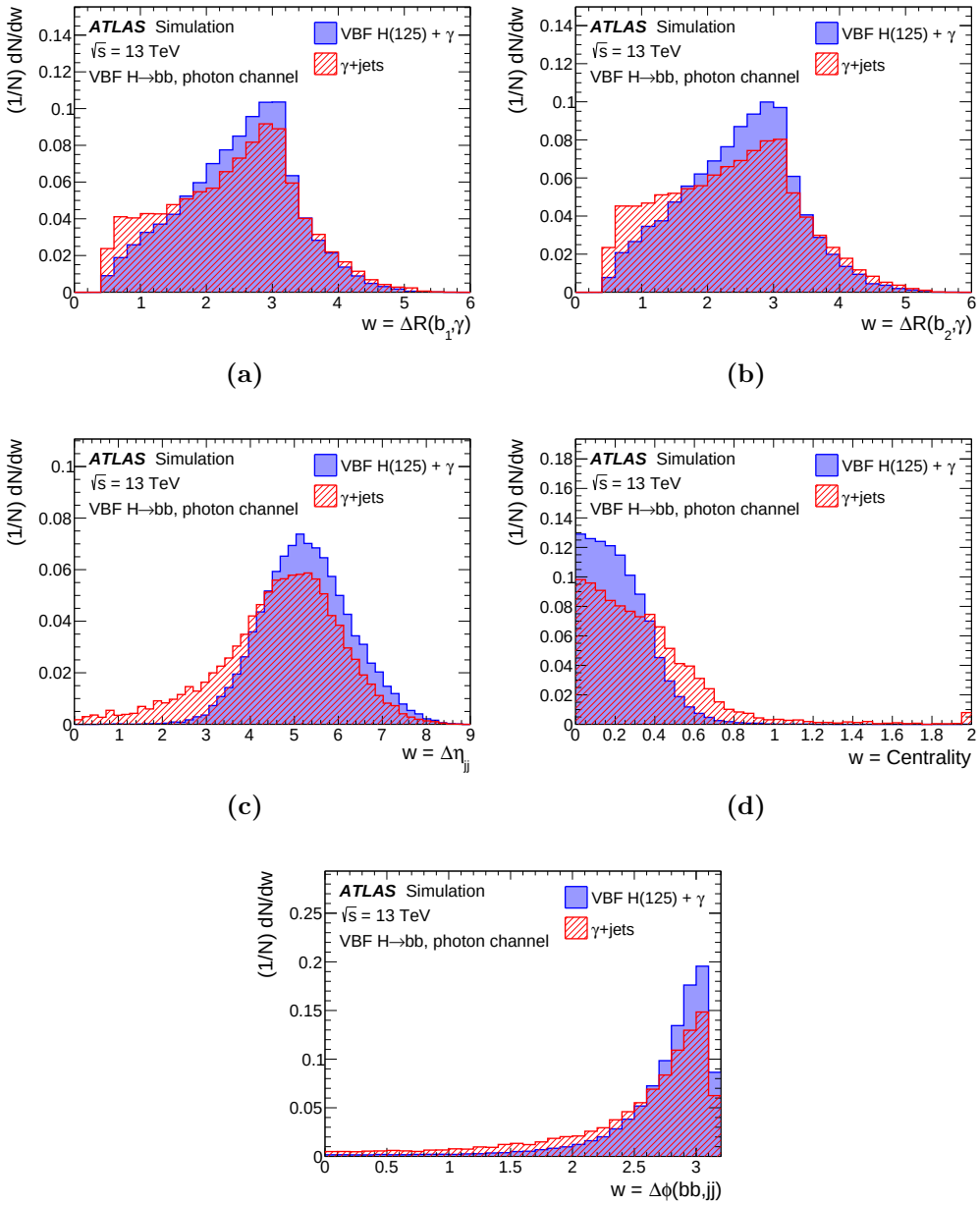

Figure D.2: *Distributions of the input variables for the multivariate analysis.*

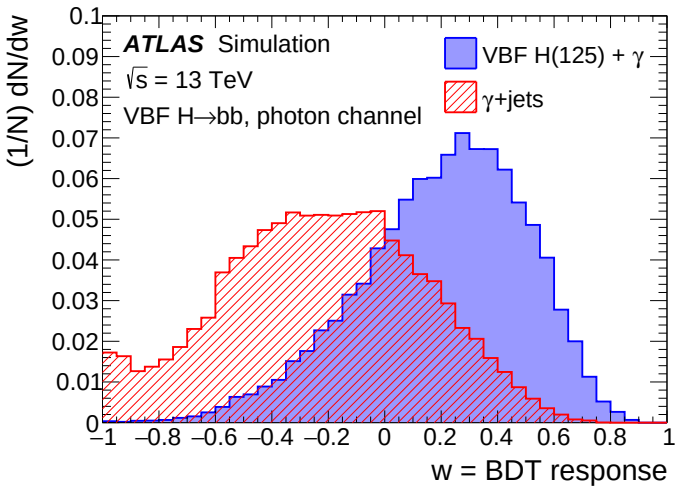

Figure D.3: *Distribution of the BDT response on data and signal MC.*

List of Figures

List of Tables

Bibliography

[1] LHC Study Group and European Organization for Nuclear Research. *Design study of the Large Hadron Collider (LHC): a multiparticle collider in the LEP tunnel*. Number 3. Not Avail, 1991.

[2] Lyndon Evans and Philip Bryant. Lhc machine. *Journal of Instrumentation*, 3(08):S08001, 2008.

[3] Georges Aad, E Abat, J Abdallah, AA Abdelalim, A Abdesselam, O Abdinov, BA Abi, M Abolins, H Abramowicz, E Acerbi, et al. The atlas experiment at the cern large hadron collider. *Journal of Instrumentation*, 3(08):S08003, 2008.

[4] Atlas Collaboration et al. Atlas detector and physics performance technical design report. *CERN/LHCC*, 15:1999, 1999.

[5] Morad Aaboud, G Aad, B Abbott, J Abdallah, O Abdinov, B Abeloos, R Aben, OS AbouZeid, NL Abraham, H Abramowicz, et al. Search for the standard model higgs boson produced by vector-boson fusion and decaying to bottom quarks in $\sqrt{s} = 8$ tev pp collisions with the atlas detector. *Journal of High Energy Physics*, 2016(11):112, 2016.

[6] Morad Aaboud et al. Search for Higgs bosons produced via vector-boson fusion and decaying into bottom quark pairs in $\sqrt{s} = 13$ TeV pp collisions with the ATLAS detector. *Phys. Rev.*, D98(5):052003, 2018.

[7] Sheldon L Glashow. Partial-symmetries of weak interactions. *Nuclear Physics*, 22(4):579–588, 1961.

[8] Abdus Salam and John Clive Ward. On a gauge theory of elementary interactions. *Il Nuovo Cimento (1955-1965)*, 19(1):165–170, 1961.

[9] Steven Weinberg. A model of leptons. *Phys. Rev. Lett.*, 19:1264–1266, Nov 1967.

[10] Nobelprize.org. The Nobel Prize in Physics 1979. `http://www.nobelprize.org/nobel_prizes/physics/laureates/1979/`, 2014.

[11] G Arnison, A Astbury, B Aubert, C Bacci, G Bauer, A Bezaguet, R Böck, TJV Bowcock, M Calvetti, T Carroll, et al. Experimental observation of isolated large transverse energy electrons with associated missing energy at s= 540 gev. *Physics Letters B*, 122(1):103–116, 1983.

[12] M Banner, R Battiston, Ph Bloch, F Bonaudi, K Borer, M Borghini, J-C Chollet, AG Clark, C Conta, P Darriulat, et al. Observation of single isolated electrons of high transverse momentum in events with missing transverse energy at the cern pp collider. *Physics Letters B*, 122(5):476–485, 1983.

[13] FJ Hasert, S Kabe, W Krenz, J Von Krogh, D Lanske, J Morfin, K Schultze, H Weerts, GH Bertrand-Coremans, J Sacton, et al. Observation of neutrino-like interactions without muon or electron in the gargamelle neutrino experiment. *Physics Letters B*, 46(1):138–140, 1973.

[14] Gerhart Luders. On the equivalence of invariance under time reversal and under particle-antiparticle conjugation for relativistic field theories. *Kong. Dan. Vid. Sel. Mat. Fys. Med.*, 28:1–17, 1954.

[15] Carlo M Becchi and Giovanni Ridolfi. *An introduction to relativistic processes and the standard model of electroweak interactions*. Springer, 2006.

[16] Juerg Beringer, JF Arguin, RM Barnett, K Copic, O Dahl, DE Groom, CJ Lin, J Lys, H Murayama, CG Wohl, et al. Review of particle physics. *Physical Review D*, 86(1), 2012.

[17] KA Olive, Particle Data Group, et al. Review of particle physics. *Chinese Physics C*, 38(9):090001, 2014.

[18] CS Wu, E Ambler, RW Hayward, DD Hoppes, and RP Hudson. Experimental test of parity conservation in beta decay. *Phys. Rev*, 104:1315, 1956.

[19] G Arnison, A Astbury, B Aubert, C Bacci, G Bauer, A Bezaguet, R Böck, TJV Bowcock, M Calvetti, P Catz, et al. Experimental observation of lepton pairs of invariant mass around 95 gev/c^2 at the cern sps collider. *Physics Letters B*, 126(5):398–410, 1983.

[20] Po Bagnaia, M Banner, R Battiston, Ph Bloch, F Bonaudi, K Borer, M Borghini, J-C Chollet, AG Clark, C Conta, et al. Evidence for $z^0 \to e^+e^-$ at the cern pp collider. *Physics Letters B*, 129(1):130–140, 1983.

[21] Murray Gell-Mann. A schematic model of baryons and mesons. *Physics Letters*, 8(3):214–215, 1964.

[22] G Zweig. An SU_3 model for strong interaction symmetry and its breaking; Version 2. (CERN-TH-412):80 p, Feb 1964. Version 1 is CERN preprint 8182/TH.401, Jan. 17, 1964.

[23] Sheldon L Glashow, Jean Iliopoulos, and Luciano Maiani. Weak interactions with lepton-hadron symmetry. *Physical Review D*, 2(7):1285, 1970.

[24] J. Aubert, U. Becker, P. Biggs, J. Burger, M. Chen, G. Everhart, P. Goldhagen, J. Leong, T. McCorriston, T. Rhoades, M. Rohde, Samuel Ting, Sau Wu, and Y. Lee. Experimental observation of a heavy particle j. *Phys. Rev. Lett.*, 33:1404–1406, Dec 1974.

[25] J. Augustin, A. Boyarski, M. Breidenbach, F. Bulos, J. Dakin, G. Feldman, G. Fischer, D. Fryberger, G. Hanson, B. Jean-Marie, R. Larsen, V. Lüth, H. Lynch, D. Lyon, C. Morehouse, J. Paterson, M. Perl, B. Richter, P. Rapidis, R. Schwitters, W. Tanenbaum, F. Vannucci, G. Abrams, D. Briggs, W. Chinowsky, C. Friedberg, G. Goldhaber, R. Hollebeek, J. Kadyk, B. Lulu, F. Pierre, G. Trilling, J. Whitaker, J. Wiss, and J. Zipse. Discovery of a narrow resonance in e^+e^- annihilation. *Phys. Rev. Lett.*, 33:1406–1408, Dec 1974.

[26] Kuang-Ta Chao, Nathan Isgur, and Gabriel Karl. Strangeness$^-$2 and$^-$3 baryons in a quark model with chromodynamics. *Phys. Rev. D*, 23:155–162, Jan 1981.

[27] Nathan Isgur and Gabriel Karl. p. *Phys. Rev. D*, 18:4187–4205, Dec 1978.

[28] Nathan Isgur and Gabriel Karl. Positive-parity excited baryons in a quark model with hyperfine interactions. *Phys. Rev. D*, 19:2653–2677, May 1979.

[29] Volker Crede and Winston Roberts. Progress towards understanding baryon resonances. *Reports on Progress in Physics*, 76(7):076301, 2013.

[30] Makoto Kobayashi and Toshihide Maskawa. Cp-violation in the renormalizable theory of weak interaction. *Progress of Theoretical Physics*, 49(2):652–657, 1973.

[31] Nicola Cabibbo. Unitary symmetry and leptonic decays. *Physical Review Letters*, 10(12):531, 1963.

[32] Franz Mandl and Graham Shaw. *Quantum field theory*. John Wiley & Sons, 2010.

[33] Jeffrey Goldstone. Field theories with ≪superconductor≫ solutions. *Il Nuovo Cimento*, 19(1):154–164, 1961.

[34] Jeffrey Goldstone, Abdus Salam, and Steven Weinberg. Broken symmetries. *Physical Review*, 127(3):965, 1962.

[35] Yoichiro Nambu. Quasi-particles and gauge invariance in the theory of superconductivity. *Phys. Rev.*, 117:648–663, Feb 1960.

[36] François Englert and Robert Brout. Broken symmetry and the mass of gauge vector mesons. *Physical Review Letters*, 13(9):321–323, 1964.

[37] Peter W Higgs. Broken symmetries, massless particles and gauge fields. *Physics Letters*, 12(2):132–133, 1964.

[38] Peter W Higgs. Spontaneous symmetry breakdown without massless bosons. *Physical Review*, 145(4):1156, 1966.

[39] M. Tanabashi et al. Review of Particle Physics. *Phys. Rev.*, D98(3):030001, 2018.

[40] C Patrignani. C. patrignani et al.(particle data group), chin. phys. c 40, 100001 (2016). *Chin. Phys. C*, 40:100001, 2016.

[41] Georges Aad, T Abajyan, B Abbott, J Abdallah, S Abdel Khalek, AA Abdelalim, O Abdinov, R Aben, B Abi, M Abolins, et al. Observation of a new particle in the search for the standard model higgs boson with the atlas detector at the lhc. *Physics Letters B*, 716(1):1–29, 2012.

[42] Serguei Chatrchyan, Vardan Khachatryan, Albert M Sirunyan, A Tumasyan, W Adam, E Aguilo, T Bergauer, M Dragicevic, J Erö, C Fabjan, et al. Observation of a new boson at a mass of 125 gev with the cms experiment at the lhc. *Physics Letters B*, 716(1):30–61, 2012.

[43] ATLAS Collaboration et al. Observation of higgs boson production in association with a top quark pair at the lhc with the atlas detector. *arXiv preprint arXiv:1806.00425*, 2018.

[44] AM Sirunyan, A Tumasyan, W Adam, F Ambrogi, E Asilar, T Bergauer, J Brandstetter, M Dragicevic, J Erö, A Escalante Del Valle, et al. Observation of t t^{-} h production. *Physical Review Letters*, 120(23):231801, 2018.

[45] M Aaboud, G Aad, B Abbott, O Abdinov, B Abeloos, DK Abhayasinghe, SH Abidi, OS AbouZeid, NL Abraham, H Abramowicz, et al. Observation of $h \to b\bar{b}$ decays and vh production with the atlas detector. *Physics Letters B*, 2018.

[46] CMS Collaboration et al. Observation of higgs boson decay to bottom quarks. *arXiv preprint arXiv:1808.08242*, 2018.

[47] Cross-section measurements of the Higgs boson decaying to a pair of tau leptons in proton–proton collisions at $\sqrt{s} = 13$ TeV with the ATLAS detector. Technical Report ATLAS-CONF-2018-021, CERN, Geneva, Jun 2018.

[48] Search for the standard model Higgs boson decaying to a pair of τ leptons and produced in association with a W or a Z boson in proton-proton collisions at $\sqrt{s} = 13$ TeV. Technical Report CMS-PAS-HIG-18-007, CERN, Geneva, 1900.

[49] Morad Aaboud, Georges Aad, Brad Abbott, Ovsat Abdinov, Baptiste Abeloos, SH Abidi, OS AbouZeid, NL Abraham, Halina Abramowicz, Henso Abreu, et al. Search for the standard model higgs boson produced in association with top quarks and decaying into a b b$^-$ pair in p p collisions at s= 13 tev with the atlas detector. *Physical Review D*, 97(7):072016, 2018.

[50] Albert M Sirunyan et al. Search for $t\bar{t}H$ production in the $H \to b\bar{b}$ decay channel with leptonic $t\bar{t}$ decays in proton-proton collisions at $\sqrt{s} = 13$ TeV. 2018.

[51] Morad Aaboud, Georges Aad, Brad Abbott, Ovsat Abdinov, Baptiste Abeloos, SH Abidi, OS AbouZeid, NL Abraham, Halina Abramowicz, Henso Abreu, et al. Evidence for the associated production of the higgs boson and a top quark pair with the atlas detector. *Physical Review D*, 97(7):072003, 2018.

[52] CMS Collaboration et al. Evidence for associated production of a higgs boson with a top quark pair in final states with electrons, muons, and hadronically decaying *tau* leptons at $\sqrt{s}$ =13 tev. *arXiv preprint arXiv:1803.05485*, 2018.

[53] CMS Collaboration. Search for the associated production of a Higgs boson and a single top quark in pp collisions at $\sqrt{s} = 13\,\text{TeV}$. 2018.

[54] Sanjoy Biswas, Emidio Gabrielli, Fabrizio Margaroli, and Barbara Mele. Direct constraints on the top-higgs coupling from the 8 tev lhc data. *Journal of High Energy Physics*, 2013(7):73, 2013.

[55] Benoît Hespel, Fabio Maltoni, and Eleni Vryonidou. Higgs and z boson associated production via gluon fusion in the sm and the 2hdm. *Journal of High Energy Physics*, 2015(6):65, 2015.

[56] T Aaltonen, VM Abazov, B Abbott, BS Acharya, M Adams, T Adams, GD Alexeev, G Alkhazov, A Alton, B Álvarez González, et al. Evidence for a particle produced in association with weak bosons and decaying to a bottom-antibottom quark pair in higgs boson searches at the tevatron. *Physical Review Letters*, 109(7):071804, 2012.

[57] ATLAS Collaboration. Evidence for the $h \to b\bar{b}$ decay with the atlas detector. *Journal of High Energy Physics*, 2017(12):24, 2017.

[58] CMS Collaboration. Evidence for the higgs boson decay to a bottom quark–antiquark pair. *Physics Letters B*, 780:501–532, 2018.

[59] Vardan Khachatryan, AM Sirunyan, Armen Tumasyan, W Adam, E Asilar, T Bergauer, J Brandstetter, E Brondolin, M Dragicevic, J Erö, et al. Search for the standard model higgs boson produced through vector boson fusion and decaying to b b. *Physical Review D*, 92(3):032008, 2015.

[60] Gilad Perez, Yotam Soreq, Emmanuel Stamou, and Kohsaku Tobioka. Constraining the charm yukawa and higgs-quark coupling universality. *Physical Review D*, 92(3):033016, 2015.

[61] Geoffrey Bodwin, Frank Petriello, Stoyan Stoynev, and Mayda Velasco. Higgs boson decays to quarkonia and the h c^- c coupling. *Physical Review D*, 88(5):053003, 2013.

[62] Alexander L Kagan, Gilad Perez, Frank Petriello, Yotam Soreq, Stoyan Stoynev, and Jure Zupan. Exclusive window onto higgs yukawa couplings. *Physical review letters*, 114(10):101802, 2015.

[63] Georges Aad, B Abbott, J Abdallah, S Abdel Khalek, O Abdinov, R Aben, B Abi, M Abolins, OS AbouZeid, H Abramowicz, et al. Search for higgs and z boson decays to j/ψ γ and υ (n s) γ with the atlas detector. *Physical review letters*, 114(12):121801, 2015.

[64] Morad Aaboud, G Aad, B Abbott, J Abdallah, O Abdinov, B Abeloos, R Aben, OS AbouZeid, NL Abraham, H Abramowicz, et al. Search for higgs and z boson decays to ϕ γ with the atlas detector. *Physical review letters*, 117(11):111802, 2016.

[65] Morad Aaboud, G Aad, B Abbott, O Abdinov, B Abeloos, SH Abidi, OS AbouZeid, NL Abraham, H Abramowicz, H Abreu, et al. Search for the decay of the higgs boson to charm quarks with the atlas experiment. *Physical review letters*, 120(21):211802, 2018.

[66] CMS Collaboration. Search for the standard model Higgs boson decaying to a pair of τ leptons and produced in association with a W or a Z boson in proton-proton collisions at $\sqrt{s} = 13$ TeV. 2018.

[67] Gian F Giudice and Oleg Lebedev. Higgs-dependent yukawa couplings. *Physics Letters B*, 665(2-3):79–85, 2008.

[68] Natascia Vignaroli. Searching for a dilaton decaying to muon pairs at the lhc. *Physical Review D*, 80(9):095023, 2009.

[69] Avital Dery, Aielet Efrati, Yonit Hochberg, and Yosef Nir. What if br (h–¿\mu\mu)/br (h–¿\tau\tau) does not equal m_\muˆ 2/m_\tauˆ 2? *arXiv preprint arXiv:1302.3229*, 2013.

[70] Search for the standard model Higgs boson decaying into two muons in pp collisions at sqrt(s)=13TeV. Technical Report CMS-PAS-HIG-17-019, CERN, Geneva, 2017.

[71] The ATLAS collaboration. A search for the rare decay of the Standard Model Higgs boson to dimuons in *pp* collisions at $\sqrt{s} = 13$ TeV with the ATLAS Detector. 2018.

[72] Georges Aad et al. Performance of the ATLAS Trigger System in 2010. *Eur. Phys. J.*, C72:1849, 2012.

[73] Morad Aaboud et al. Performance of the ATLAS Trigger System in 2015. *Eur. Phys. J.*, C77(5):317, 2017.

[74] R Achenbach, P Adragna, V Andrei, P Apostologlou, B Åsman, C Ay, BM Barnett, B Bauss, M Bendel, C Bohm, et al. The atlas level-1 calorimeter trigger. *Journal of Instrumentation*, 3(03):P03001, 2008.

[75] D Berge, G Schuler, A Krasznahorkay, P Farthouat, P Klofver, T Pauly, S Haas, T Wengler, A Messina, R Spiwoks, et al. The atlas level-1 muon to central trigger processor interface. 2007.

[76] Ralf Spiwoks, S Ask, Nick Ellis, P Farthouat, P Gällnö, J Haller, A Krasznahorkay, T Maeno, T Pauly, H Pessoa-Lima, I Resurreccion-Arcas, G Schuler, J M De Seixas, R Torga-Teixeira, and T Wengler. The ATLAS Level-1 Central Trigger Processor (CTP). Technical Report ATL-DAQ-CONF-2005-030. CERN-ATL-DAQ-CONF-2005-030, 2005.

[77] Eduard Simioni, S Artz, B Bauss, V Büscher, A Kaluza, R Degele, K Jakobi, C Kahra, A Reiss, J Schäffer, et al. The topological processor for the future atlas level-1 trigger: from design to commissioning. In *Real Time Conference (RT), 2014 19th IEEE-NPSS*, pages 1–5. IEEE, 2014.

[78] 2015 start-up trigger menu and initial performance assessment of the ATLAS trigger using Run-2 data. Technical Report ATL-DAQ-PUB-2016-001, CERN, Geneva, Mar 2016.

[79] Trigger Menu in 2016. Technical Report ATL-DAQ-PUB-2017-001, CERN, Geneva, Jan 2017.

[80] Trigger Menu in 2017. Technical Report ATL-DAQ-PUB-2018-002, CERN, Geneva, Jun 2018.

[81] G Aad, M Ackers, FA Alberti, M Aleppo, G Alimonti, J Alonso, EC Anderssen, A Andreani, A Andreazza, JF Arguin, et al. Atlas pixel detector electronics and sensors. *Journal of Instrumentation*, 3(07):P07007, 2008.

[82] M Capeans, G Darbo, K Einsweiller, M Elsing, T Flick, M Garcia-Sciveres, C Gemme, H Pernegger, O Rohne, and R Vuillermet. ATLAS Insertable B-Layer Technical Design Report. Technical Report CERN-LHCC-2010-013. ATLAS-TDR-19, Sep 2010.

[83] Alessandro La Rosa, ATLAS collaboration, et al. The atlas insertable b-layer: from construction to operation. *Journal of Instrumentation*, 11(12):C12036, 2016.

[84] Soshi Tsuno. Physics performance of the atlas pixel detector. *Journal of Instrumentation*, 12(01):C01025, 2017.

[85] Inputs to Jet Reconstruction and Calibration with the ATLAS Detector Using Proton-Proton Collisions at $\sqrt{s} = 900$ GeV. Technical Report ATLAS-CONF-2010-016, CERN, Geneva, Jul 2010.

[86] Properties of Jets and Inputs to Jet Reconstruction and Calibration with the ATLAS Detector Using Proton-Proton Collisions at $\sqrt{s} = 7$ TeV. Technical Report ATLAS-CONF-2010-053, CERN, Geneva, Jul 2010.

[87] Optimisation and performance studies of the ATLAS b-tagging algorithms for the 2017-18 LHC run. Technical Report ATL-PHYS-PUB-2017-013, CERN, Geneva, Jul 2017.

[88] Rudolph Emil Kalman. A new approach to linear filtering and prediction problems. *Journal of Fluids Engineering*, 82(1):35–45, 1960.

[89] Measurements of the Higgs boson production and decay rates and constraints on its couplings from a combined ATLAS and CMS analysis of the LHC pp collision data at $\sqrt{s} = 7$ and 8 TeV. Technical Report ATLAS-CONF-2015-044, CERN, Geneva, Sep 2015.

[90] Elzbieta Richter-Was, Daniel Froidevaux, and Luc Poggioli. Atlfast 2.0 a fast simulation package for atlas. Technical report, 1998.

[91] Stefano Frixione, Giovanni Ridolfi, and Paolo Nason. A positive-weight next-to-leading-order monte carlo for heavy flavour hadroproduction. *Journal of High Energy Physics*, 2007(09):126, 2007.

[92] Stefano Frixione, Paolo Nason, and Giovanni Ridolfi. The powheg-hvq manual version 1.0. *arXiv preprint arXiv:0707.3081*, 2007.

[93] Torbjörn Sjöstrand, Stephen Mrenna, and Peter Skands. A brief introduction to pythia 8.1. *Computer Physics Communications*, 178(11):852–867, 2008.

[94] MadGraph Manual. Madevent: a multipurpose event generator powered by madgraph, 2007.

[95] Sea Agostinelli, John Allison, K al Amako, J Apostolakis, H Araujo, P Arce, M Asai, D Axen, S Banerjee, G Barrand, et al. Geant4—a simulation toolkit. *Nuclear instruments and methods in physics research section A: Accelerators, Spectrometers, Detectors and Associated Equipment*, 506(3):250–303, 2003.

[96] Rene Brun and Fons Rademakers. Root—an object oriented data analysis framework. *Nuclear Instruments and Methods in Physics Research Section A: Accelerators, Spectrometers, Detectors and Associated Equipment*, 389(1):81–86, 1997.

[97] Jan Therhaag and TMVA Core Developer Team. Tmva-toolkit for multivariate data analysis. In *INTERNATIONAL CONFERENCE OF COMPUTATIONAL METHODS IN SCIENCES AND ENGINEERING 2009:(ICCMSE 2009)*, volume 1504, pages 1013–1016. AIP Publishing, 2012.

[98] Georges Aad, Tatevik Abajyan, Brad Abbott, J Abdallah, S Abdel Khalek, O Abdinov, R Aben, B Abi, M Abolins, OS AbouZeid, et al. Jet energy measurement and its systematic uncertainty in proton–proton collisions at $sqrts = 7$ tev with the atlas detector. *The European Physical Journal C*, 75(1):17, 2015.

[99] ATLAS collaboration et al. Calibration of b-tagging using dileptonic top pair events in a combinatorial likelihood approach with the atlas experiment. ATLAS-CONF-2014-004, 2014.

[100] Morad Aaboud, G Aad, B Abbott, J Abdallah, O Abdinov, B Abeloos, R Aben, OS AbouZeid, NL Abraham, H Abramowicz, et al. Luminosity determination in pp collisions at $sqrts = 8$ tev using the atlas detector at the lhc. *The European Physical Journal C*, 76(12):653, 2016.

[101] Georges Aad, T Abajyan, B Abbott, J Abdallah, S Abdel Khalek, O Abdinov, R Aben, B Abi, M Abolins, OS AbouZeid, et al. Measurement of the electroweak production of dijets in association with a z-boson and distributions sensitive to vector boson fusion in proton-proton collisions at sqrt {s}= 8 tev using the atlas detector. *Journal of High Energy Physics*, 2014(4):1–56, 2014.

[102] S Dittmaier, C Mariotti, G Passarino, R Tanaka, S Alekhin, J Alwall, EA Bagnaschi, A Banfi, J Blumlein, S Bolognesi, et al. Handbook of lhc higgs cross sections: 2. differential distributions. *arXiv preprint arXiv:1201.3084*, 2012.

[103] Gennaro Corcella, Ian G Knowles, Giuseppe Marchesini, Stefano Moretti, Kosuke Odagiri, Peter Richardson, Michael H Seymour, and Bryan R Webber. Herwig 6: an event generator for hadron emission reactions with interfering gluons (including supersymmetric processes). *Journal of High Energy Physics*, 2001(01):010, 2001.

[104] A Sherstnev and Robert S Thorne. Parton distributions for lo generators. *The European Physical Journal C*, 55(4):553–575, 2008.

[105] Richard D Ball, Valerio Bertone, Stefano Carrazza, Christopher S Deans, Luigi Del Debbio, Stefano Forte, Alberto Guffanti, Nathan P Hartland, José I Latorre, Juan Rojo, et al. Parton distributions with lhc data. *Nuclear Physics B*, 867(2):244–289, 2013.

[106] Lorenzo Moneta, Kevin Belasco, Kyle Cranmer, Sven Kreiss, Alfio Lazzaro, Danilo Piparo, Gregory Schott, Wouter Verkerke, and Matthias Wolf. The roostats project. *arXiv preprint arXiv:1009.1003*, 2010.

[107] Wouter Verkerke and David Kirkby. The roofit toolkit for data modeling. In *Statistical Problems in Particle Physics, Astrophysics and Cosmology*, pages 186–189. World Scientific, 2006.

[108] Alexander L Read. Presentation of search results: the cls technique. *Journal of Physics G: Nuclear and Particle Physics*, 28(10):2693, 2002.

[109] Glen Cowan, Kyle Cranmer, Eilam Gross, and Ofer Vitells. Asymptotic formulae for likelihood-based tests of new physics. *The European Physical Journal C-Particles and Fields*, 71(2):1–19, 2011.

[110] Zhijun Liang, Bo Liu, Javier Llorente Merino, Jason Nielsen, Peyton Rose, Liaoshan Shi, Song-Ming Wang, and Jacob Martin Pasner. Search for Higgs Boson Production via Weak Boson Fusion in Association with a High-Energy Photon. Technical Report ATL-COM-PHYS-2016-1693, CERN, Geneva, Nov 2016.

[111] ATLAS Collaboration et al. Search for higgs bosons produced via vector-boson fusion and decaying into bottom quark pairs in $sqrts = 13$ tev pp collisions with the atlas detector. *arXiv preprint arXiv:1807.08639*, 2018.

[112] Emidio Gabrielli, Fabio Maltoni, Barbara Mele, Mauro Moretti, Fulvio Piccinini, and Roberto Pittau. Higgs boson production in association with a photon in vector boson fusion at the lhc. *Nuclear Physics B*, 781(1-3):64–84, 2007.

[113] Emidio Gabrielli, Barbara Mele, Fulvio Piccinini, and Roberto Pittau. Asking for an extra photon in higgs production at the lhc and beyond. *Journal of High Energy Physics*, 2016(7):3, 2016.

[114] Fabian Pedregosa, Gaël Varoquaux, Alexandre Gramfort, Vincent Michel, Bertrand Thirion, Olivier Grisel, Mathieu Blondel, Peter Prettenhofer, Ron Weiss, Vincent Dubourg, et al. Scikit-learn: Machine learning in python. *Journal of machine learning research*, 12(Oct):2825–2830, 2011.

[115] Morad Aaboud, G Aad, B Abbott, J Abdallah, O Abdinov, B Abeloos, SH Abidi, OS AbouZeid, NL Abraham, H Abramowicz, et al. Jet energy scale measurements and their systematic uncertainties in proton-proton collisions at s= 13 tev with the atlas detector. *Physical Review D*, 96(7):072002, 2017.

[116] Atlas Collaboration et al. Performance of b-jet identification in the atlas experiment. *Journal of instrumentation*, 11(04):P04008, 2016.

[117] ATLAS collaboration et al. Optimisation of the atlas b-tagging performance for the 2016 lhc run. Technical report, ATL-PHYS-PUB-2016-012, 2016.

[118] ATLAS Collaboration et al. Performance of the atlas track reconstruction algorithms in dense environments in lhc run 2,(2017). *arXiv preprint arXiv:1704.07983*.

[119] Georges Aad, B Abbott, J Abdallah, O Abdinov, B Abeloos, R Aben, M Abolins, OS AbouZeid, NL Abraham, H Abramowicz, et al. Measurement of the charged-particle multiplicity inside jets from $sqrts = 8$ tev pp collisions with the atlas detector. *The European Physical Journal C*, 76(6):322, 2016.

[120] ATLAS collaboration et al. Electron and photon energy calibration with the atlas detector using data collected in 2015 at $\sqrt{s} = 13$ tev. *CERN, Geneva, Tech. Rep. ATL-PHYS-PUB-2016-015*, 2016.

[121] ATLAS collaboration et al. Photon identification in 2015 atlas data. Technical report, ATL-PHYS-PUB-2016-014, 2016.

[122] R Aggleton, M Ahmad, B Allanach, Charalampos Anastasiou, Elisabetta Furlan, Agnieszka Ilnicka, Achilleas Lazopoulos, Pasquale Musella, Luca Perrozzi, et al. Handbook of lhc higgs cross sections: 4. deciphering the nature of the higgs sector. *CERN Yellow Reports: Monographs*, 2(2017), 2017.

[123] Abdel Djouadi, Jan Kalinowski, and Michael Spira. Hdecay: A program for higgs boson decays in the standard model and its supersymmetric extension. *Computer Physics Communications*, 108(1):56–74, 1998.

[124] ATLAS collaboration et al. Optimisation and performance studies of the atlas b-tagging algorithms for the 2017-18 lhc run. Technical report, ATL-PHYS-PUB-2017-013, 2017.

[125] ATLAS collaboration et al. Fast tracker (ftk) technical design report. *CERN, Geneva, Tech. Rep. CERN-LHCC-2013-007. ATLAS-TDR-021*, 2013.

[126] Brian Batell, Stefania Gori, and Lian-Tao Wang. Higgs couplings and precision electroweak data. *Journal of High Energy Physics*, 2013(1):139, 2013.

[127] Charles Leggett, John Baines, Tomasz Bold, Paolo Calafiura, Steven Farrell, Peter van Gemmeren, David Malon, Elmar Ritsch, Graeme Stewart, Scott Snyder, et al. Athenamt: upgrading the atlas software framework for the many-core world with multi-threading. In *Journal of Physics: Conference Series*, volume 898, page 042009. IOP Publishing, 2017.

[128] GA Stewart, J Baines, T Bold, P Calafiura, A Dotti, SA Farrell, C Leggett, D Malon, E Ritsch, S Snyder, et al. Multi-threaded software framework development for the atlas experiment. In *Journal of Physics: Conference Series*, volume 762, page 012024. IOP Publishing, 2016.

[129] Performance of mass-decorrelated jet substructure observables for hadronic two-body decay tagging in ATLAS. Technical Report ATL-PHYS-PUB-2018-014, CERN, Geneva, Jul 2018.

[130] Gilles Louppe, Michael Kagan, and Kyle Cranmer. Learning to pivot with adversarial networks. In *Advances in Neural Information Processing Systems*, pages 981–990, 2017.

[131] Chase Shimmin, Peter Sadowski, Pierre Baldi, Edison Weik, Daniel Whiteson, Edward Goul, and Andreas Søgaard. Decorrelated jet substructure tagging using adversarial neural networks. *Physical Review D*, 96(7):074034, 2017.